Western Australian School of Mines

Department of Exploration Geophysics

Elastic Properties of Carbonates: Measurements and Modelling

Osni Bastos de Paula

This thesis is presented for the Degree of

Doctor of Philosophy

of

Curtin University

August 2011

Declaration

To the best knowledge and belief this thesis contains no material previously published by any other person except where due acknowledgement has been made.

This thesis contains no material which has been accepted for the award of any other degree or diploma in any university.

Signature

Date: 03 August 2011

I dedicate this thesis

to

my family

ACKNOWLEDGEMENTS

During the past 3 years while undertaking my PhD, I have greatly enjoyed my journey through many scientific paths. I firstly acknowledge and thank my supervisor Professor Boris Gurevich. His brilliant ideas, endless enthusiasm, guidance and support were fundamental in producing this thesis. I also wish to thank my co-supervisor, Dr Marina Pervukhina for her thoughtful ideas, confidence and encouragement which made a huge contribution to this thesis.

I also greatly thank Mrs Dina Makarynska, for sharing her codes with me and our useful discussions. I am grateful to Dr Maxim Lebedev who helped me a lot with digital rocks and laboratory issues. I am also grateful to Dr Milovan Urosevic, Dr Roman Pevzner, Dr Anton Kepic, Mr Elmar Strobach and Mr Dominic Howman for their immense contribution in the planning, acquisition and processing of ground penetrating radar (GPR) and seismic data from Shark Bay. I would also like to thank Mr Ricardo Jahnert and Dr Lindsay Collins for the fruitful discussions we had about carbonate systems.

I would also like to thank all the staff and colleagues of the Department of Exploration Geophysics. My special thanks go to Ms Deirdre Hollingsworth and Ms Jennifer McPherson for their administrative help and to Mr Robert Verstandig for his IT support and reviewing expertise.

I also experienced very productive interactions with the CSRIO Earth Science and Resource Engineering staff. My thanks go to Dr Claudio Delle Piane, Dr Tobias Muller, Dr Ben Clennell, Dr Valeriya Shulakova and Dr Matthew Josh.

My thanks also to Dr Mark Knackstedt, from the Australia National University and Dr Andrew Squelch, from Curtin University, for their support in the digital rock experiments, and Dr Mariusz Martyniuk, from the University of Western Australia, who collaborated on the nanoindentation experiments.

I am very grateful for the financial assistance provided by Petrobras, Petroleo Brasileiro S.A. and the commitment of Mr Guilherme Vasquez, Dr Nilo Matsuda, Mr Anderson Chagas, Mr Eduardo Moreno, Dr Marcos Grochau, Mr Carlos Beneduzi, Mr Viviane Sampaio, Dr Lucia Dillon, Dr Carlos Lopo Varela, Dr Andre Romanelli, Mr Roberto Dávila, Dr Sylvia dos Anjos, Dr Mario Carminatti and Dr Guilherme Estrella.

I would like also to acknowledge the sponsors of the Curtin Reservoir Geophysics Consortium (CRGC), and CSIRO Earth Sciences and Resource Engineering.

And last but not least, I would like to give a special thank you to my wife Rossana, who has supported me in this journey with all of her kindness and serenity. I want also to extend this special thanks to my sons Fabio and Renato for their understanding and also to my parents, Odorico and Suely for their belief in me.

This is the last time I use the first person in singular (I) in this thesis. From now on the first person plural (we) are used because it absolutely reflects the close interaction between all fellows listed above. Our research dissertation follows.

ABSTRACT

This thesis is a multi-scale study of carbonate rocks, from the nanoscale and digital rock investigations to the imaging studies of carbonate reservoir analogues. The essential links between these extremes are the carbonate physical properties and rock-physics models, which are investigated here through the modelling of ultrasonic wave propagation in carbonate samples, focusing on elastic stress sensitivities, saturating fluids and porosity models. Validation of Gassmann fluid substitution in carbonates is also investigated using correlations between core and well log measurements.

On the nanoscale, we use the nanoindentation technique in an oolitic limestone to directly measure the calcite Young modulus and derive bulk and shear moduli. We have found a large variation in the calcite bulk modulus, from 56 to 144 GPa. The high values obtained in some oolite rings were interpreted as genetically associated with biologically generated calcite (biocalcite). There are many measurements that achieve these values in brachiopod shells, but none in oolitic limestone. We associate the smaller values with microporosity, which is undetectable by our microCT or even SEM images. On the microscale we use the X-ray microCT images. From these images we can compute oolite elastic parameters using finite difference methods (FDM). In this oolite sample, calcite was segmented in two distinct phases. Nanoindentation provides the elastic parameters for each phase. The results of the modelling are compared with ultrasonic measurements on dry samples.

To compute the properties of rocks on fluid-saturated samples, one needs to use fluid substitution methods, such as Gassmann's equations. However, the applicability of Gassmann's equations and the fluid substitution technique to carbonate rocks is still a subject of debate. Here we compare the results of fluid substitution applied to dry core measurements against sonic log data. The 36 meters of continuously sampled carbonates data, comes from a cretaceous reservoir buried at a depth of 5000 metres in the Santos Basin, offshore Brazil. Compressional and shear velocities, density and porosity were measured in 50 samples covering the entire interval. We obtain good agreement between the elastic properties obtained from core and log measurements. This shows that Gassmann's fluid substitution is applicable to these carbonates, at least at sonic log frequencies.

Carbonate microstructure is investigated using the stress dependency of shear and compressional wave velocities according to the dual porosity model of Shapiro (2003). The model assumes that the pore space contains two types of pores: stiff and compliant pores. Understanding the parameters of this model for different rocks is important for constraining stress effects in these rocks. The results for a carbonate dataset from the Santos Basin show a good correlation between compliant porosity and dry bulk modulus, total porosity and density for 29 samples of carbonates from the Santos Basin. The correlations seem to be different for different facies distribution, with different trends for mudstone facies and grainstone and rudstone facies. We also performed the same analysis using 66 samples of sandstones of diverse origins (Han et al., 1986): a good correlation appears between compliant porosity and the dry bulk modulus for all samples. If we correlate only the 7 samples from Fontainebleau sandstone, a good correlation also appears between total and compliant porosity. This analysis shows that the correlation is facies dependent also for sandstones.

While Gassmann's equations may be valid for low frequencies, they are not applicable at higher frequencies, where squirt dispersion is significant. We propose a workflow to model wave dispersion and attenuation due to the squirt flow using the geometrical parameters of the pore space derived from the stress dependency of elastic moduli on dry samples. Our analysis shows the dispersion is controlled by the squirt flow between equant pores and intermediate pores (with aspect ratios between 10^{-3} - $2 \cdot 10^{-1}$). Such intermediate porosity is expected to close at confining pressures of between 200-2000 MPa. We also infer the magnitude of the intermediate porosity and its characteristic aspect ratio. Substituting these parameters into the squirt model, we have computed elastic moduli and velocities of the water-saturated rock and compared these predictions against laboratory measurements of these velocities. The agreement is good for a number of clean sandstones, but much worse for a broad range of shaley sandstones. Our predictions show that dispersion and attenuation caused by the squirt flow between compliant and stiff pores may occur in the seismic frequency band. Confirmation of this prediction requires laboratory measurements of elastic properties at these frequencies.

The carbonate system of Telegraph Station, Shark Bay (WA), is a unique environment where coquinas, stromatolites and microbial mats are linked: an excellent analogue to carbonate pre-salt offshore Brazil. We acquired 7.5 km of GPR data and

high resolution seismic data in the coquina ridges. They are composed by calcite shells deposited by cyclones, which show excellent high resolution GPR images, being a low loss dielectric medium. Three classes of coquinas were mapped: tabular layers, convex-up crest and washover fan. From the correlation of ^{14}C dating of 50 samples and the mapped events we can estimate an average rate of one event every 13 years. From our interpretation the Holocene regression is continuous but not homogeneous. Carbonate dissolution features, faults, trends and discontinuities were mapped. Analysis of these features helps us understand reservoir porosity and permeability distribution in carbonate deposits, and can be used to constrain reservoir properties in pre-salt carbonates in Brazilian basins.

TABLE OF CONTENTS

LIST OF FIGURES

LIST OF TABLES

CHAPTER 1

INTRODUCTION

1.1. The challenging carbonates

Predictions of carbonate properties and fluid contents from seismic is still a challenge despite all the efforts and resources when dealing with new technologies, high resolution data and new geological models. The main problem is that carbonate systems are characterised by a great spatial variability of parameters such as porosity and permeability. Rock physical models that take into consideration these specific features of carbonate rocks can constrain seismic interpretation and give more confidence in results of quantitative geophysical approaches like AVO and time-lapse analysis. To achieve the desired confidence we must start understanding the carbonate microstructure analysis at nanoscale, including petrography analysis and porosity characterisation, followed by larger scale studies like the digital rock approach given by microCT scans (Arns et al., 2002) and computational rock physics (Dvorkin et al., 2011).

Laboratory measurements are of crucial importance for hydrocarbon exploration. Even sophisticated geological models, derived from well logs and seismic datasets that improve resolution every year, need to be tested and validated experimentally. The best way to achieve this goal is through laboratory experiments in controlled conditions. Advances in technology also make the laboratories better equipped and new, valuable information can be obtained to help to understand the ultimate datasets. The number of laboratory ultrasonic measurements in carbonates will increase, and to address this demand, new and more efficient theoretical models need to be employed to explain these data. Some of these promising approaches result from studies of stress dependency of velocities and also more complex fluid substitution techniques.

Finally, the understanding of the physical properties of carbonates, measured or estimated (but well calibrated), are fundamental for the quantitative seismic interpretation of the complex carbonate reservoirs. In the following paragraphs we review some of the consolidated concepts and classifications of carbonates, a starting point for understanding their complexity. As distinct from sandstones, the carbonates

remain in situ where they are deposited, in very restrictive conditions, but their evolution during geological time is often much more complex than the evolution of sandstones. Carbonate porosity and permeability can change dramatically during the geological time since diagenesis begins in the earliest stages of consolidation (Eberly, 1997). Dolomitisation, the process of calcium to magnesium substitution, is one of the most important processes of the reservoir properties degradation. Dolomitisation usually decreases porosity (Lucia, 2007) and increases bulk and shear moduli. Because of this complex behaviour, in terms of geological models, it is important to establish the main trends. Another important aspect is the interaction between the matrix and the fluid saturating the pores. At high pressures and temperatures the reactive solutions in the pore space can affect the matrix and thus drastically change elastic properties that affect seismic wave propagation. This effect is not taken into account in most of the poroelasticity models described in the literature.

A brief description of carbonates terminology is needed since we will refer to them later. The primary definition comes with the predominant mineral of the sample: the rock is defined as a limestone if more than 50% of the mineral content is calcite. In the case where more than 50% of the mineral content is dolomite then the rock is a dolostone. A genetic classification that takes in account the depositional texture was due to Dunhan (1962), dividing the carbonates into 7 classes (Figure 1.1). A few new terms were introduced later to complement Dunhan's classification, like Rudstone introduced by Hembry and Klovan (1971). In this case, Rudstone is a variation of the grain supported Grainstone, but with more than 10% of the components greater than 2mm.

Another important classification when dealing with carbonates is based on the porosity type. Choquete and Pray (1970) described 15 types of porosity, primarily grouping them as fabric selective, non-fabric selective and also four types of porosity that are independent of the original fabric. Figure 1.2 describes their classification.

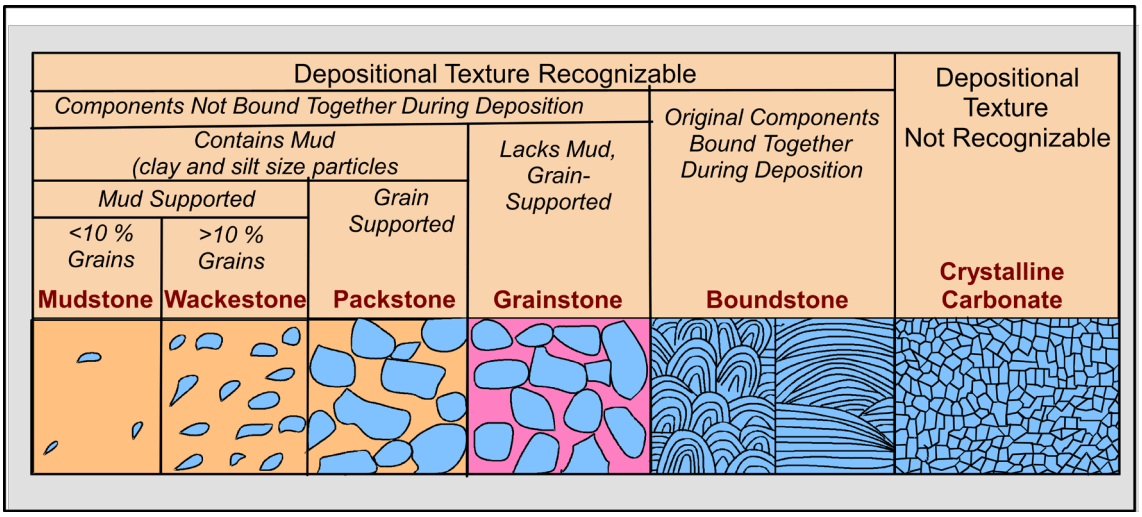

Figure 1.1. The Dunhan classification (1962) of carbonates defining 7 basic terms to describe depositional texture.

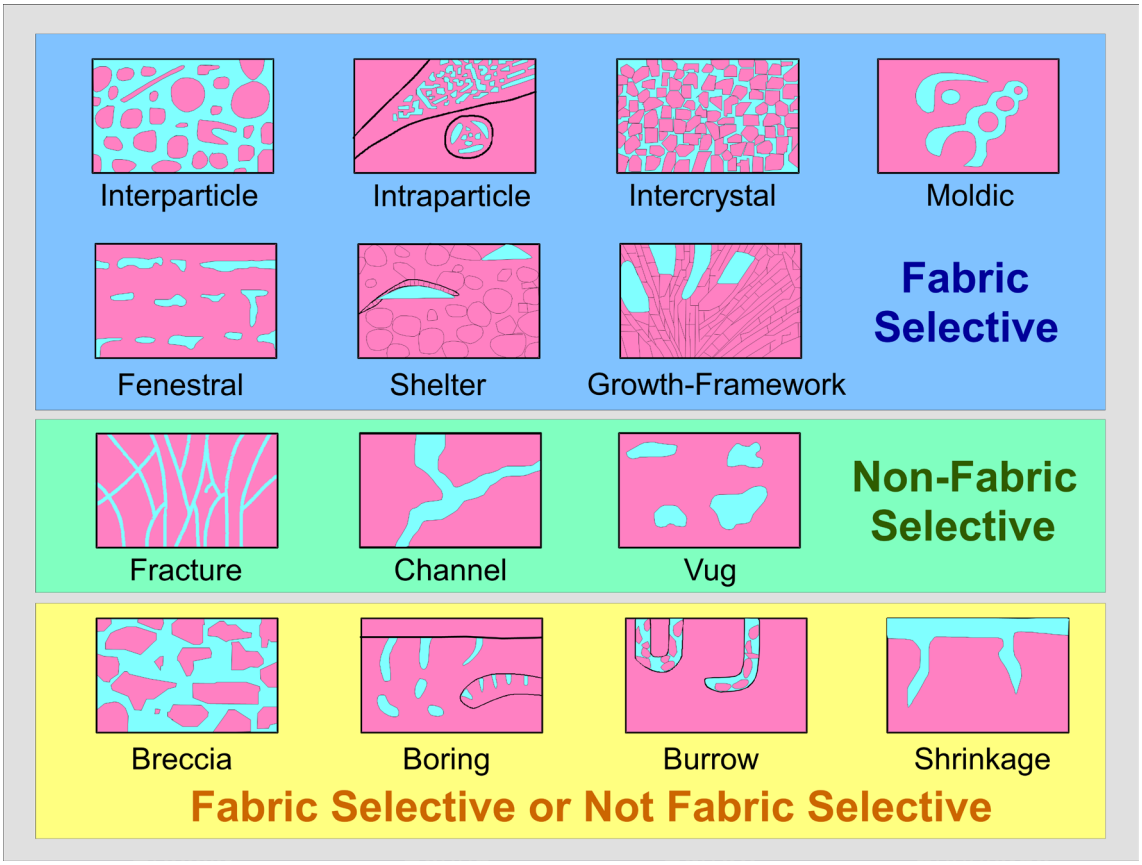

Figure 1.2. The Choquete and Pray (1970) classification of porosity. The porosity can be primary, created during the deposition or secondary, originating after deposition during the diagenesis process. Porosity can also be fabric selective or completely independent of original carbonate fabric.

1.2. Aim of the research

The proposed research seeks to obtain, analyse and upscale laboratory measurements of elastic properties on reservoir carbonate samples and develop theoretical models and workflows that can be used in log analyses and quantitative seismic interpretation. Better understanding of the dispersion and attenuation mechanisms taken from the proposed laboratory experiments lead to a better prediction of carbonate properties. The microstructure of carbonates is analysed using high quality X-Ray microCT to construct realistic dual-nature porosity models, quantify stiffness and compliance porosities and extract elastic parameters for seismic waves. With this approach we maximise the use of laboratory information, constrained by realistic geological information. The ultimate goal is the minimisation of hydrocarbon exploration risks.

The main focus of this project is the quantitative seismic interpretation. This area is becoming day by day one of the most important areas of the hydrocarbon exploration and production (E&P), due to increasing data resolution and availability of new technologies. These advances lead to a more deterministic approach in exploration, giving significance to interpretation and statistical quantification of the intrinsic error evaluation. The heterogeneity parameters that directly affect the poroelastic properties are basically extracted from the rock samples and well logs.

1.3. Thesis layout

This dissertation is composed of six chapters focusing on carbonates at different scales, from nano/micro scales discussed in the second chapter to meter/decimetre scales of GPR and seismic data in chapter six. The multi scale approach is sometimes clearly linked, like when we use microCT images to explain some GPR responses. The following briefly describes the chapters' content:

Chapter 2. A new possibility for better understanding of the carbonate microstructures comes from X-Ray CT images. With modern microCT scanners, the 3D structure of carbonate samples can be obtained at resolution of a few microns. In addition, the use of visualisation software packages and modern computers allows pore space mapping and simulation of rock elastic properties. Using a carbonate core plug, Arns (2005) showed the potential of mapping the microstructure and estimating

petrophysical properties, such as permeability, drainage capillarity pressure, formation factor and Nuclear Magnetic Resonance (NMR) response. This procedure is called computational rock physics and one of its limitations is the variability of elastic moduli at the microscale.

Chapter 2. We use electron microscopy (2D) and nanoindentation experiments to constrain the elastic properties of carbonate grains. The procedure described here is particularly useful in carbonates due to their dynamic framework, with their unstable macro and micro porosity and the elastic parameters of their individual grains.

Chapter 3. Many theoretical models and different approaches are described in the literature that try to predict elastic properties of rock trough fitting laboratory measurements. One of the best known and useful models are Gassmann's equations (1951) that relate the bulk and shear moduli of a saturated porous medium to the bulk and shear moduli of the same medium in the dry case. According to Wang (2001), the velocities obtained from laboratory measurements at the high frequencies or derived from well logging data are often higher than those estimated by Gassmann's equations. Gassmann's equations give good results for sandstones at seismic frequencies, but sometimes fail for carbonates because they do not predict chemical interaction between the fluid and matrix. Most of these conclusions come only from laboratory measurements, with little or no constraints from field environments. In Chapter 3 we show a case where Gassmann's fluid substitution gives good results in carbonates, using ultrasonic core measurements and sonic log data. The high quality carbonates data comes from a Cretaceous reservoir buried at 5000 meters depth in the Santos Basin, offshore Brazil.

Chapter 4. A study of complex dual-nature porosity of reservoir rocks is necessary for quantitative understanding of seismic wave propagation in reservoirs. The compliant porosity can be estimated from stress dependency of dry rock compressibility using an isotropic theory from Shapiro (2003). In Chapter 4 we explore this theory using a carbonate dataset from the Santos Basin and samples from a variety of sandstones (Han et al., 1986). The estimated compliant porosity and aspect ratios show good correlations with the dry bulk modulus, total porosity and density for the samples of carbonates from the Santos Basin. The rules of correlation nevertheless seem to obey the facies distribution, with different trends for mudstone facies and grainstone and rudstone facies. A minor correlation is obtained between the aspect ratio of compliant

pores and dry bulk modulus, total porosity and density. We achieve similar results with the sandstones.

Chapter 5. When dealing with ultrasonic measurements in the complex carbonate porous-space, the high frequency effects must be considered. Some of the mechanisms of viscous and inertial interaction between the fluid and the mineral matrix of the rocks were taken into account in the theory developed by Biot (1956). He derived theoretical formulae for predicting the high frequency acoustic velocities of saturated rocks in terms of dry rock properties. This theory was later extended to anisotropic media (Biot, 1962). Another effect to be considered in the high frequency range is the squirt effect: a propagating wave induces pore pressure gradients in a saturated porous rock and squirt or local flow then tries to compensate these pressure gradients. Mavko and Jizba (1991) derived expressions at very high frequencies that describe the increase in bulk and shear modulus stiffness due to squirt flow. A new squirt model (Gurevich et al., 2010) gives the complex and frequency-dependent effective bulk and shear moduli of a rock. In Chapter 5 we describe an alternative approach to the new squirt model (Gurevich, 2010): first, we assume the aspect ratio of the pore space is derived from the Shapiro formulation (2003) and secondly, we assume that not all the compliant pores are closed at the level of stress obtained at laboratory measurements. With the first step we overcome the derivation of being dependent on wet measurements while with the latter assumption we are able to overcome the limitation of laboratories (maximum confining pressures). Using this approach we can explain the elastic behaviour of many fluid saturated sandstones (Han et al., 1986).

Chapter 6. One of the scientific goals of the study of modern carbonate systems is to apply new information to enhance the knowledge of the genesis and evolution of ancient analogues. Our carbonate reservoirs are in this context and the interpretation of modern data will improve our knowledge of their properties and spatial distribution. In Chapter 6 we describe the acquisition of 2D high resolution seismic and GPR data acquired at the coquina Ridges of Telegraph Station in eastern Hamelin Pool, Shark Bay (Western Australia). With GPR we recover shallow data, at least down to the water table (15 meters), while with the seismic data we can obtain deeper information (60 meters). Besides the spatial behaviour of the Holocene, Pleistocene and underneath sequences that help us understand the recent evolution and facies distribution, we also

compare laboratory data with the field derived data, showing a good consistency between these different scales.

1.4. Publications arising from this thesis

- De Paula, O. B., M. Pervukhina, and B. Gurevich, 2008, Role of compliant porosity in stress dependency of ultrasonic velocities in carbonates and sandstones: III Simposio Brasileiro de Geofisica, SBGf.
- De Paula, O. B., B. Gurevich, M. Pervukhina, and D. Makarynska, 2009, Application of a new model of squirt-flow attenuation and dispersion in carbonates: 7^{1th} EAGE Conference & Exhibition.
- De Paula, O. B., M. Pervukhina, and B. Gurevich, 2010, Testing Gassmann fluid substitution in carbonates: sonic log versus ultrasonic core measurements: 81th Annual Meeting, SEG.
- De Paula, O. B., M. Pervukhina, B. Gurevich, M. Lebedev, M. Martyniuk, and C. Delle Piane, 2010, Estimation of Carbonate Elastic Properties from Nanoindentation Experiments to Reduce Uncertainties in Reservoir Modelling: 21th International Geophysical Conference & Exhibition, ASEG.
- De Paula, O. B., B. Gurevich, M. Pervukhina, M. Lebedev, M. Martyniuk, and C. Delle Piane, 2010, Estimation of Carbonate Elastic Properties using Nanoindentation and Digital Images: 72th EAGE Conference & Exhibition.
- De Paula, O. B., M. Pervukhina, D. Makarynska, and B. Gurevich, 2012, Modeling squirt dispersion and attenuation in fluid saturated rocks using pressure dependency of dry ultrasonic velocities: Geophysics, **77**, 157-168
- Gurevich, B., D. Makarynska, O. B. De Paula, and M. Pervukhina, 2010, A simple model for squirt-flow dispersion and attenuation in fluid-saturated granular rocks: Geophysics, **75**, 109-120.
- Gurevich, B., M. Pervukhina, D. Makarynska, and O. B. De Paula, 2009, A new model for squirt-flow attenuation and dispersion in fluid-saturated rocks: 71th EAGE Conference & Exhibition.
- Gurevich, B., D. Makarynska, M. Pervukhina, and O. B. De Paula, 2009, A new squirt-flow model of elastic wave attenuation and dispersion in fluid-saturated rocks: Poromechanics IV, Proceedings of 4th Biot Conference on Poromechanics.

- Gurevich, B., D. Makarynska, O. B. De Paula, and M. Pervukhina, 2011, Squirt-flow attenuation and dispersion in fluid-saturated rocks: 1st International Workshop on Rock Physics.
- Gurevich, B., D. Makarynska, and O. B. De Paula, 2011, Bounds for seismic dispersion and attenuation in poroelastic rocks: SEG Annual Meeting, (submitted).
- Jahnert, R., O. B. De Paula, L. Collins, E. Strobach, and R. Pevzner, 2011, Evolution of a Carbonate Barrier in Shark Bay by GPR Imaging: Architecture of a Holocene Reservoir Analogue: Sedimentary Geology (submitted).
- Lebedev, M., M. Pervukhina, O. B. De Paula, B. Clennell, and B. Gurevich, 2009, Dynamic elastic properties from micro-CT images: modeling and experimental validation: EGU General Assembly.
- Shulakova,V., M. Pervukhina, T. M. Muller, M. Lebednev, S. Schmidt, P. Golodoniuc, O. B. De Paula, B. M. Clennel, and B. Gurevich, 2011, Computational elastic up-scaling of sandstones on the basis of X-ray microtomographic images: Geophysical Prospecting (submitted).

CHAPTER 2

CALCITE NANOINDENTATION AND DIGITAL ROCK SIMULATIONS OF ELASTIC PARAMETERS

2.1. Background

Carbonate rock physics properties are by far less predictable than those of siliciclastic reservoir rocks because of their chemical sensitivity to interstitial fluids and their variable and complex porosity. Carbonates can rapidly stiffen due the early diagenesis. Nevertheless, when they are exposed or in contact with fresh water, a dissolution process is triggered increasing the macro and micro porosity and changing the elastic parameters of the weathered rock.

With the aim of better constraining the elastic properties of porous carbonates and the variability of elastic moduli at the microscale, we undertake a multidisciplinary study where results from nanoindentation experiments and microstructure visualisation by the means of microCT (3D) and electron microscopy (2D) are used to feed finite element models.

Nanoindentation is a well-known technique recently used to study the mechanical properties of composite materials (Constantines et al., 2006) and the nanomechanics of biomaterials (Merkel et al., 2009 and Bruet et al., 2005). This technique measures material hardness by pressing a hard tip (like diamond) with known properties into a sample whose properties are unknown. A load is placed on the tip as it penetrates further into the specimen. The hardness is obtained by dividing the maximum load by the residual area produced by the indenter into the specimen.

Many recent nanoindentation studies focus on biogenetic calcite samples to study skeletal support and protection (Gunda and Volinski, 2008). They show that the elastic moduli, in particular the Young Modulus (E) of biocalcite crystals, depend on the particular functionality in the structural framework. The Young Modulus of biocalcite also differs from that of inorganic calcite: Merkel et al. (2009) showed that modern calcite in brachiopods dorsal and ventral valves always show a higher Young modulus

than inorganic calcite. The high modulus is interpreted as due to different amount of inter- and intra-crystalline organic matrices. Weiner et al. (2000) also shows that even a single crystal of biomineral can exhibit mechanical properties far higher than its inorganic counterparts, a feature that he attributed to occlusion of often very low levels of macro molecules within the crystals. Values in the order 100 GPa for a seashell nacre were obtained by Bruet et al. (2005). Gunda and Volinski (2008) obtained 75 +/- 4.9 GPa for a single crystal of calcite while investigating the construction of nano-sized surface patterns. Huerta et al. (2007) conclude that molluscs can produce a wide range of ultrastructures using calcium carbonate: they found a Young Modulus of 60-110/120 GPa in a calcite semi-nacre shell and 20-60/80 GPa in calcite fibres.

With the intention of investigating variability of elastic moduli to constrain carbonate reservoir modelling, we choose an oolitic limestone sample to be tested via nanoindentation experiments. This sample was primarily chosen due the high complexity of its pore space introduced by selective microporosity: it is more developed in the darker rings when compared with the lighter rings of the oolite. There is no publication of nanoindentation in this type of rock, except the ones that emerged from this thesis (De Paula et al., 2010a and De Paula et al., 2010b).

2.2. Methodology

A sample of heavily weathered oolitic carbonate from the Dampier Formation, southern Carnarvon Basin in Western Australia was chosen for this experiment. Heterogeneities and dissolution patterns of the analysed oolite are present from the outcrop (Figure 2.1) to the micro/nanoscale (Figures 2.2 to 2.4), a detailed knowledge of their influence on the bulk rock elastic and mechanical properties can help in constraining realistic models and reduce the uncertainties related to exploration in carbonate reservoirs. More details about the Pleistocene Dampier Formation and the oolite distribution can be found in Logan et al. (1970).

The sample is first analysed using the microCT technique to visualise the pore distribution and connectivity in 3D; next, scanning electron microscope (SEM) images are acquired from the same sample to image the microporosity and mineral phase distribution. Nanoindentation tests are then used to measure the elastic parameters of various regions of the samples more or less affected by dissolution. Finally, using these

results, a finite element model simulating the elastic behaviour of the carbonate is fine tuned.

2.3. Carbonate Sample

The sample of oolitic limestone has a complex structure that was formed during several stages of deposition and diagenesis. Concentric calcite rings, sometimes deposited around a quartz core, are a common oolite feature (Figures 2.2 and 2.3). The black round and irregular spots present secondary intragranular microporosity formed as a result of calcite dissolution in the concentric rings. Macropores between oolite particles were also developed in the micritic cement during diagenesis (Figures 2.3 and 2.4).

The mineral composition of the oolite was analysed using semi-quantitative X-ray diffraction (XRD). This technique is based in an X-ray tube that bombards the sample powder and produces diffractions in a range of angles. The peaks of energy as a function of the diffraction angles reflect specific wavelengths that are characteristic of the target materials. The interpretation of these data (Figure 2.5) shows that the oolitic sediment is composed of 79% of calcite, 11% of aragonite, 6% of quartz and 2% of ankerite (values given in weight %).

Figure 2.6 shows one of 14 point analyses acquired using Energy Dispersive X-Ray Spectroscopy in the SEM to identify the composition of the oolite rings. All the spectra show that the rings are composed of calcium carbonate.

Porosity and permeability obtained by helium injection as a function of pressure are shown in Figure 2.7. The porosity decreases considerably from 17% at a confining pressure of 7 MPa to 14.2% at 10 MPa and then decreases slightly to 13.8% at 22 MPa. Permeability also decreases from 0.037 mD at confining pressure of 7 MPa to 0.030 mD at 21 MPa. A higher porosity of 27% (Figure 2.8) was obtained using the mercury injection technique. This anomalous value is probably caused by sample damaging during transporting and testing. Nevertheless, the Figure 2.5 shows that two thirds of the total porosity is found in micropores with throat diameters from 10 to 30 nm. It is important to note that the diameters of these small pores are beyond the resolution of the microCT scan (1 micron).

Figure 2.1. Outcrop of heavily weathered oolitic carbonate from the Dampier Formation, southern Carnarvon Basin in Western Australia.

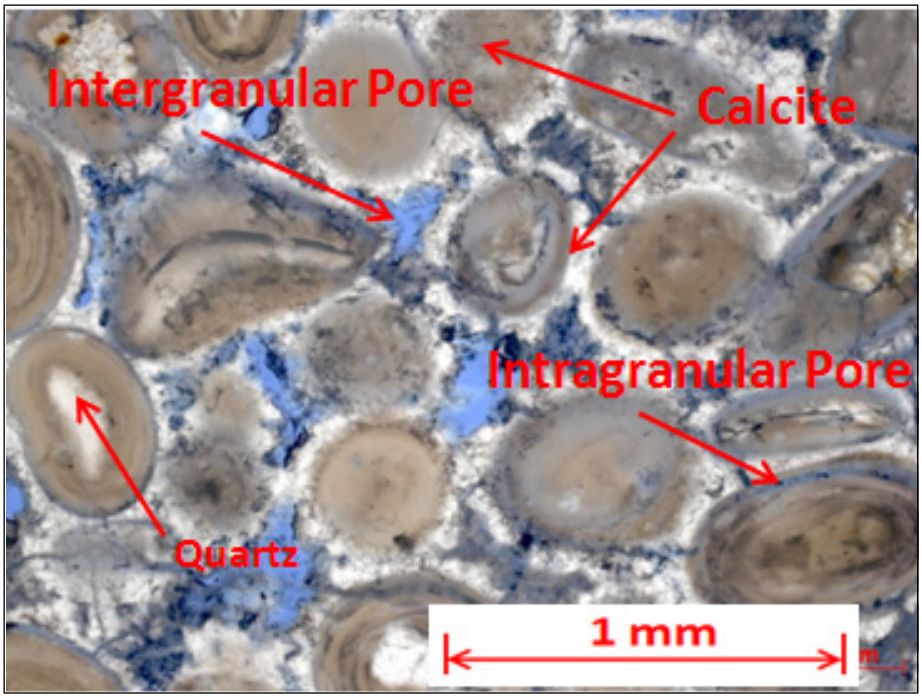

Figure 2.2. Oolite thin section showing details of the microstructure complexity. Intergranular porosity is visible in blue and micritic cement made of calcite in white showing a strong dissolution feature. Note a crystal of quartz inside the oolite.

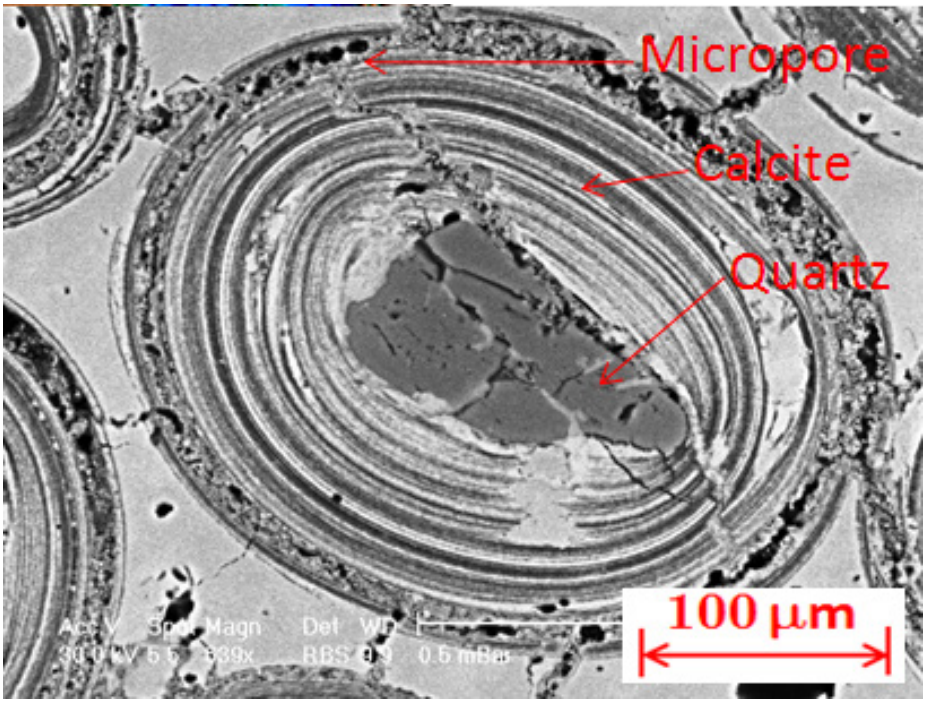

Figure 2.3. Oolite SEM image showing a fractured quartz seed, calcite rings and macro/microporosity. The pore space (black) is distributed along preferential rings and inside the micritic cement.

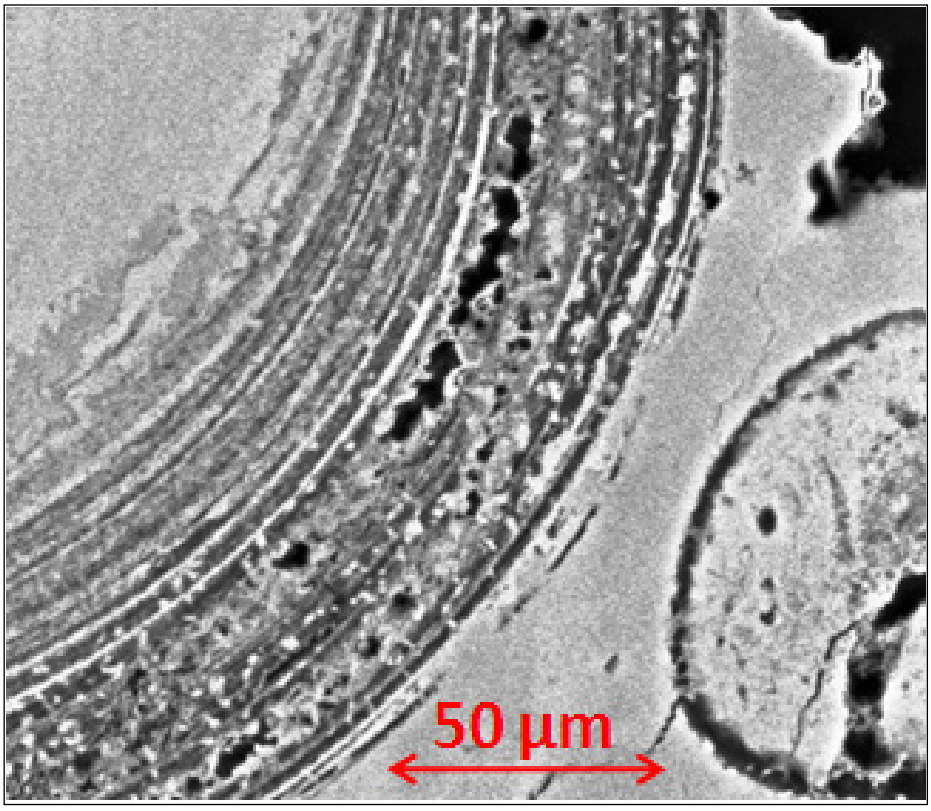

Figure 2.4. Oolite SEM image showing calcite rings, micritic cement and macro/microporosity. Note that microporosity is selective and grows preferentially along the dark rings of calcite.

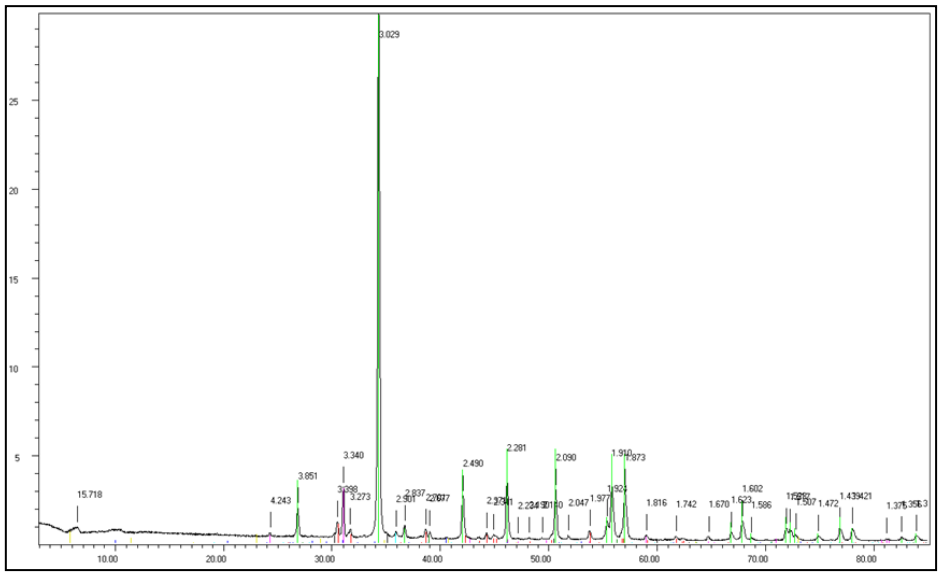

Figure 2.5. X-ray diffraction (XRD) pattern acquired to obtain the oolite sample composition. The identified mineral fractions are calcite (79%), aragonite (11%), quartz (6%) and ankerite (2%).

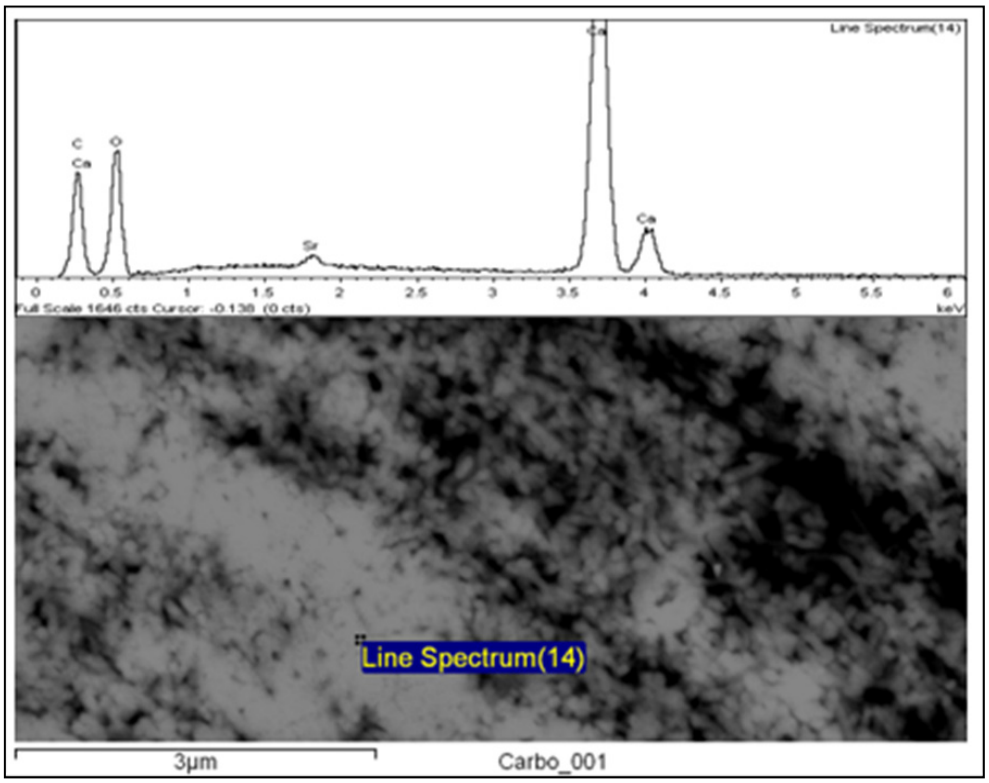

Figure 2.6. Energy Dispersive X-Ray Spectroscopy of the rings of oolite. The point analysis spectrum shows that the rings are made of pure calcium carbonate.

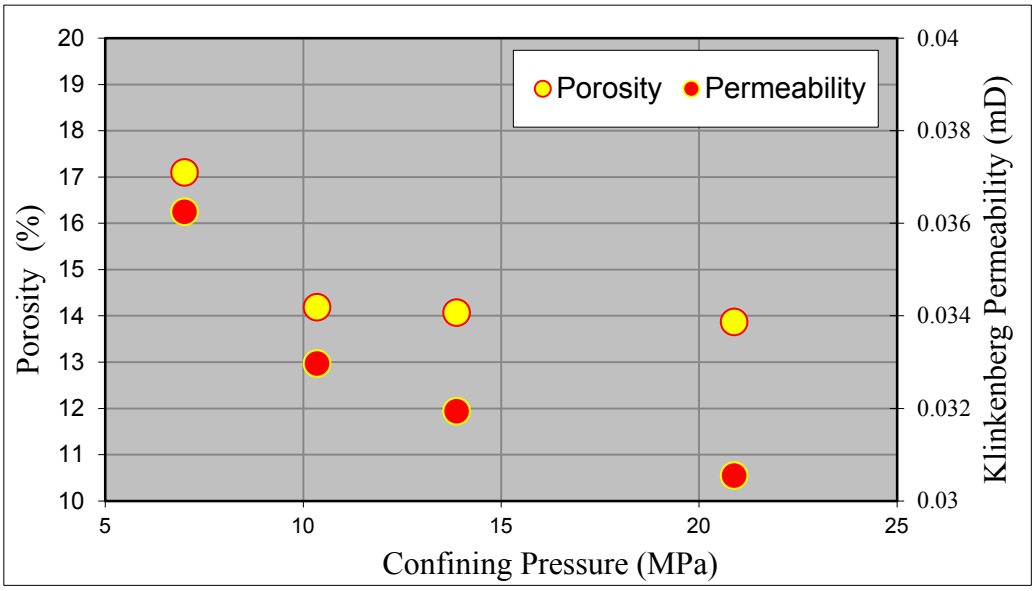

Figure 2.7. Oolite porosity and permeability as a function of increasing confining pressure obtained by helium injection. The helium porosity is on average 14% and the Klinkemberg permeability on average 0.03 mD.

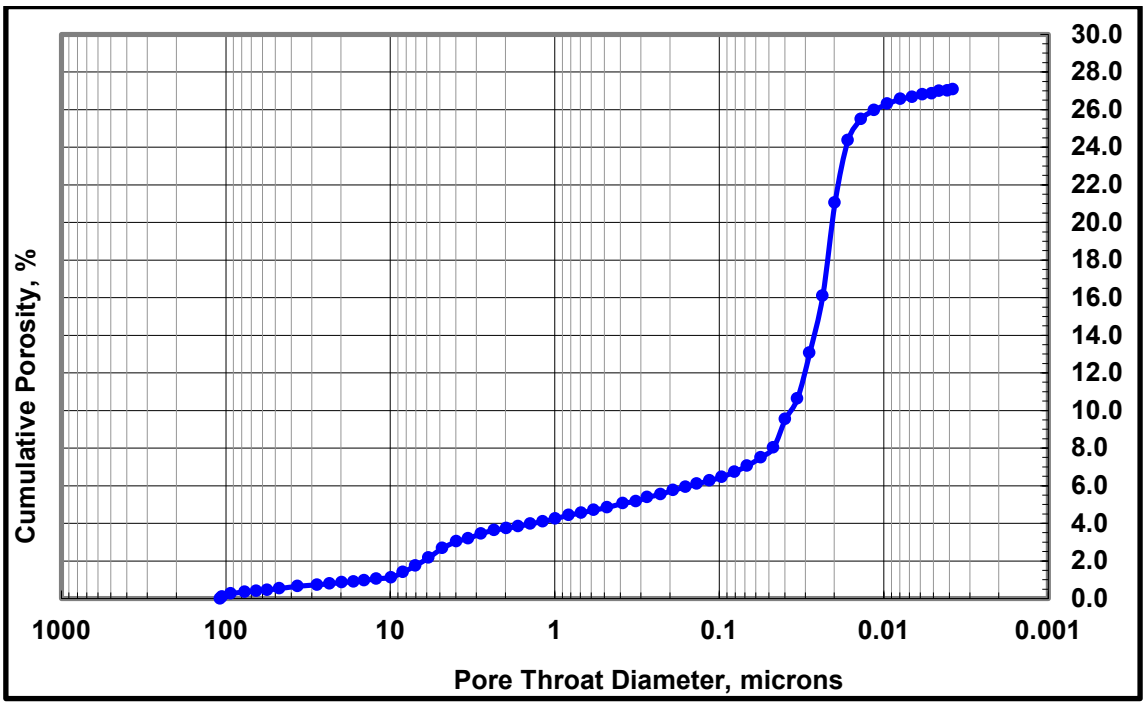

Figure 2.8. Oolite porosity as a function of pore throat diameters obtained from Mercury injection. Note that most of the pores are below 0.4 microns and cannot be resolved using microCT imaging (maximum resolution around 1 micro).

2.4. Nanoindentation experiment

Before indentation testing, the sample needs to be polished to a flat surface. The residual topography is shown in the atomic force microscope (AFM) image (Figure 2.9). The same image, with some enhancement processing, is shown in Figure 2.10. Residual roughness of about 80 nm is the result of different resistance to abrasion of the micritic cement, the stiff concentric rings (beige) and the softer rings (valleys in blue). The AFM image (Figure 2.9) maps concentric ring pattern similar to the microCT and SEM images implying that different parts of this carbonate sample, i.e., dense and dissolved concentric calcite rings and micritic cement, have different mechanical properties that can be measured by the nanoindentation technique.

We used the so-called grid-indentation technique as recently used by Ulm and co-workers for heterogeneous materials (Ortega et al., 2007). The technique is based on a number of nano-contact experiments and a statistical analysis of resulting measurements. A total of 49 nano-contact points marked by red crosses in Figure 2.10 are distributed over a wide area which embraces dense and dissolved carbonate concentric rings of an oolite particle and micritic cement. Force-driven indentation tests are operated for each of the nano-contact points using a Hysitron nanoindenter TS70.

Young's modulus (E) for each point is calculated from the measured load (P) and indentation depth (h) (see Figure 2.11 for more details) as follows

$$\boldsymbol{E = \frac{\sqrt{\pi}}{2}\frac{S}{\sqrt{A_c}}(1-\nu^2)} \tag{2.1}$$

Here v is Poisson's ratio, $S = (dP/dh)_{h=hmax}$ which is the unloading slope of the force-depth curve and A_c is the projected contact surface between the indenter and the deformed material surface, which is determined as a function of the measured maximum indentation depth h_{max}.

The only parameter here that is not measured is the Poisson ratio. Constantines et al. (2006) showed that a great precision is not necessary in the estimation of Poisson's ratio to obtain a reasonable estimation of Young's modulus (in the range of v: 0.1-0.4, the error on E is less than 10%). We extended this sensitivity study to the other elastic parameters and the main results are shown in Figure 2.12. It is shown that if we increase the Poisson ratio by 10% (from 0.30 to 0.33) we overestimate the bulk modulus (+15%), underestimate the shear modulus (-4%), overestimate the compressional

velocity (+4%) and underestimate the shear velocity (-2%). In our modelling we use ν=0.30 for calcite, with a degree of confidence following the described rules. The oolite itself has a Poisson ratio of ν=0.29 (Equation 2.2), bulk modulus K=16.7 GPa and shear modulus μ=8.2 GPa, obtained from the laboratory measurements of ultrasonic compressional wave velocity (V_P=4108 m/s), shear wave velocities (V_S=2241 m/s) and density (ρ=1640 kg/m^3). Most of the published Poisson ratios for calcite are in the range of between 0.30 and 0.32, giving us confidence in our estimations.

$$\nu = \frac{3K-2\mu}{2(3K+2\mu)} \tag{2.2}$$

The histogram of the Young's moduli obtained by the nanoindentation experiment is shown in Figure 2.13. The presence of two calcite components can be inferred on the basis of the histogram analysis,that is, the harder component with an average value of Young's modulus of about 144 GPa and the softer component with a Young's modulus of about 56 GPa. It is assumed that this difference in Young's modulus of the unaltered calcite grains and partially dissolved rims is caused by the presence of nano- and micro-pores which are below the resolution of microCT scanner.

2.5. Elastic modelling

The histogram of the grey-level distribution obtained from the microCT image of the oolite carbonate sample is shown in Figure 2.14. Four main phases, namely, soft and stiff calcite, quartz and pore space can be distinguished in the histogram. The pore space (or extremely dissolved calcite) distribution is shown as a blue curve, quartz as a black curve and soft and stiff calcite as red curves.

To obtain the effective elastic moduli from the microCT images we use a Finite Element Method (FEM). The FEM code (Arns, 2000) simulates an effective elastic moduli using as an input exact 3D geometry of each phase and its elastic moduli. We processed the microCT images using AVIZO (VSG, Inc.) software and generated a 400^3 pixels cube. Figure 2.15 shows the cube with intergranular porosity in yellow. In order to simplify the model and analyse the sensitivity to the different calcite phase ratios (soft and stiff) we have segmented the images into three phases: porous space, soft calcite and stiff calcite (Figure 2.16). We generated nine distinct segmented images, varying volumes of pore space (phase 1) from 21% to 31%, soft calcite (phase 2) from

29% to 58% and stiff calcite from 15% to 39%. The modelling parameters and results are listed on the table below:

Phase1(Pore)	Phase2(Soft)	Phase3(Hard)	K	μ
0,21	0,45	0,34	19,2	13,7
0,21	0,52	0,27	17,9	12,5
0,21	0,58	0,21	16,7	11,6
0,26	0,40	0,34	12,9	9,9
0,26	0,47	0,27	12,0	9,2
0,26	0,53	0,21	11,1	8,5
0,31	0,29	0,39	8,8	7,3
0,31	0,41	0,27	7,7	6,4
0,31	0,53	0,15	6,6	5,5

Table 2.1. Modelling parameters and the effective elastic moduli obtained from the Finite Element Method (FEM).

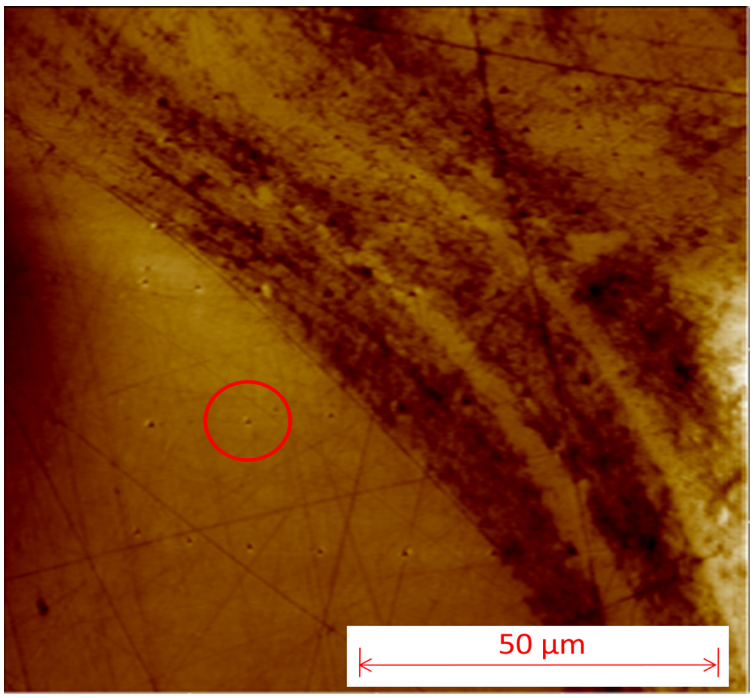

Figure 2.9. Oolite topographic map from 40 nm (white) to -40 nm (brown) after polishing. Note one of the indentation points in the centre of red circle (Image from the AFM).

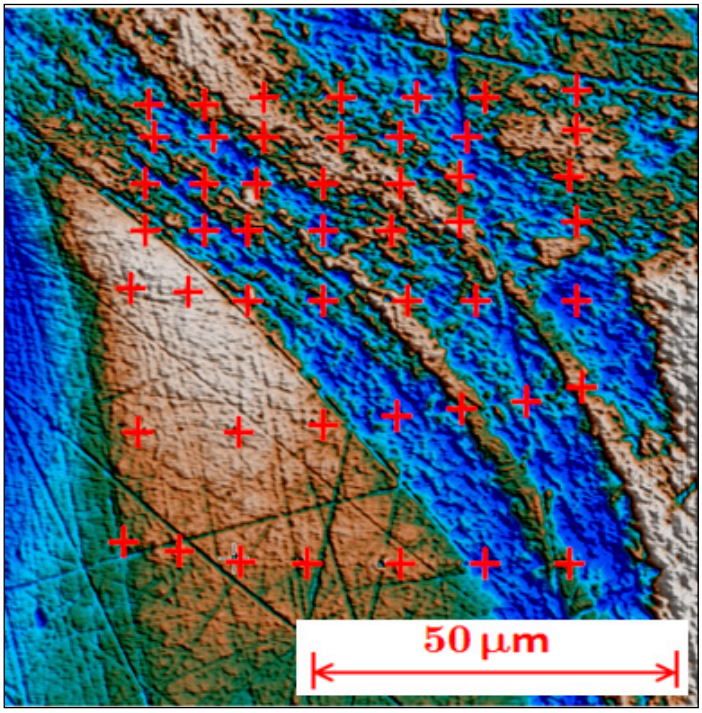

Figure 2.10. Oolite topographic map from -40 nm (blue) to 40 nm (white) after polishing and with the nanoindentation grid superimposed (crosses in red).

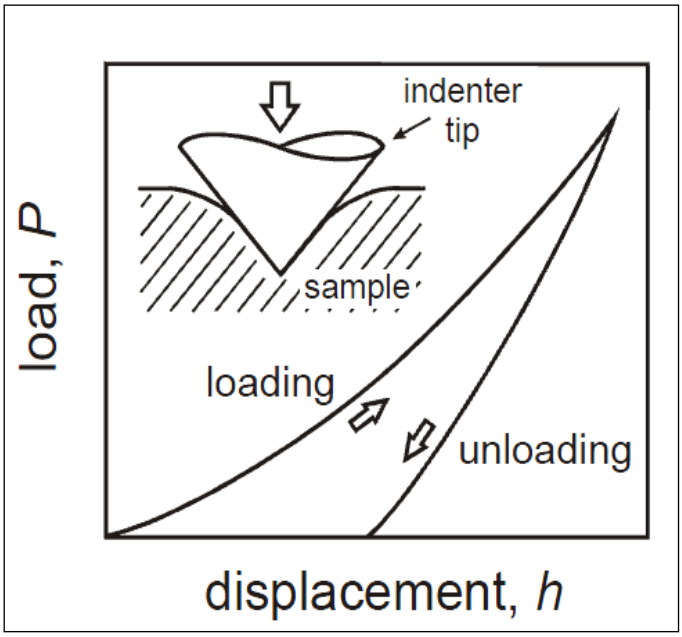

Figure 2.11. Indenter experiment with the penetration depth history into a test sample as a function of an applied load *P* (Martyniuk, 2006).

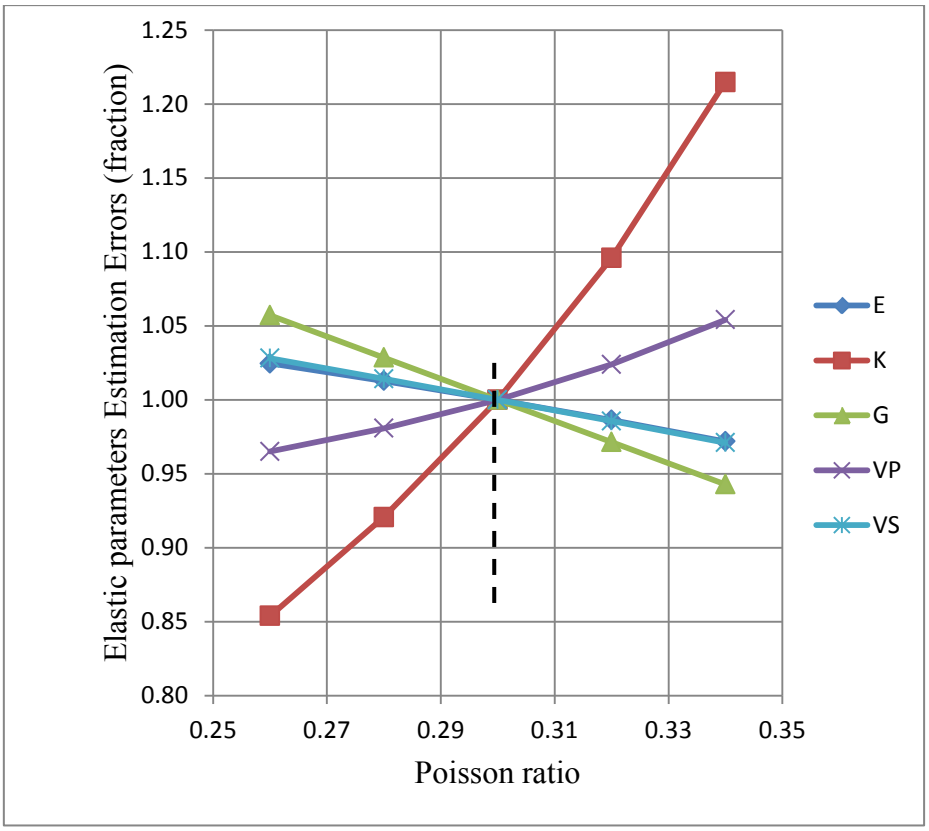

Figure 2.12. Propagation of errors to elastic parameters as a function of Poisson ratio v estimations. Note that increasing v from 0.30 to 0.33 we overestimate in 15% bulk modulus K (red), underestimate shear modulus G in 4% (green), overestimate compressional velocity V_P in 4% (magenta) and underestimate shear velocity V_S in 2% (blue).

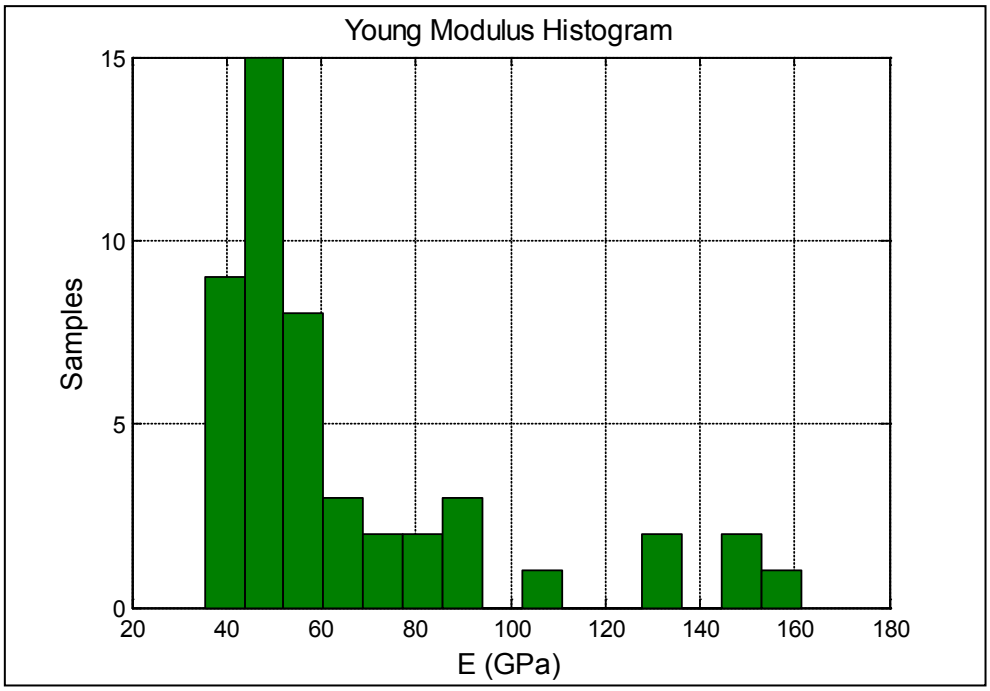

Figure 2.13. Distribution of calcite Young Modulus *E* obtained from the nanoindentation tests.

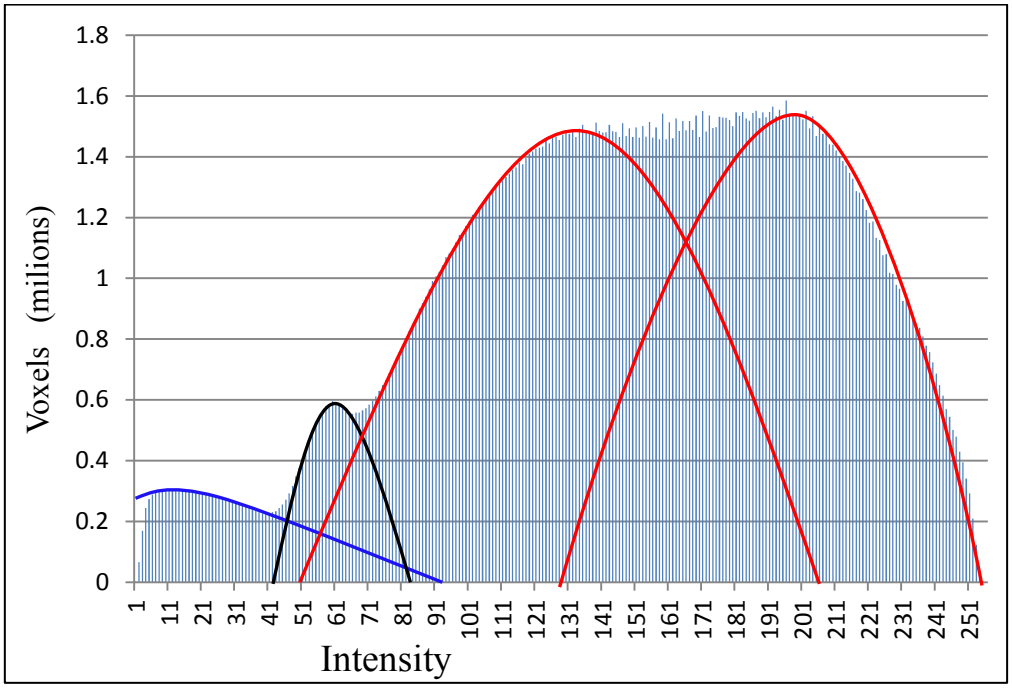

Figure 2.14. Histogram of the grey level from the CT image showing the low intensity values due the pore space (blue), an intermediate cluster due to quartz (black) and the higher intensities due to soft and stiff calcite (red).

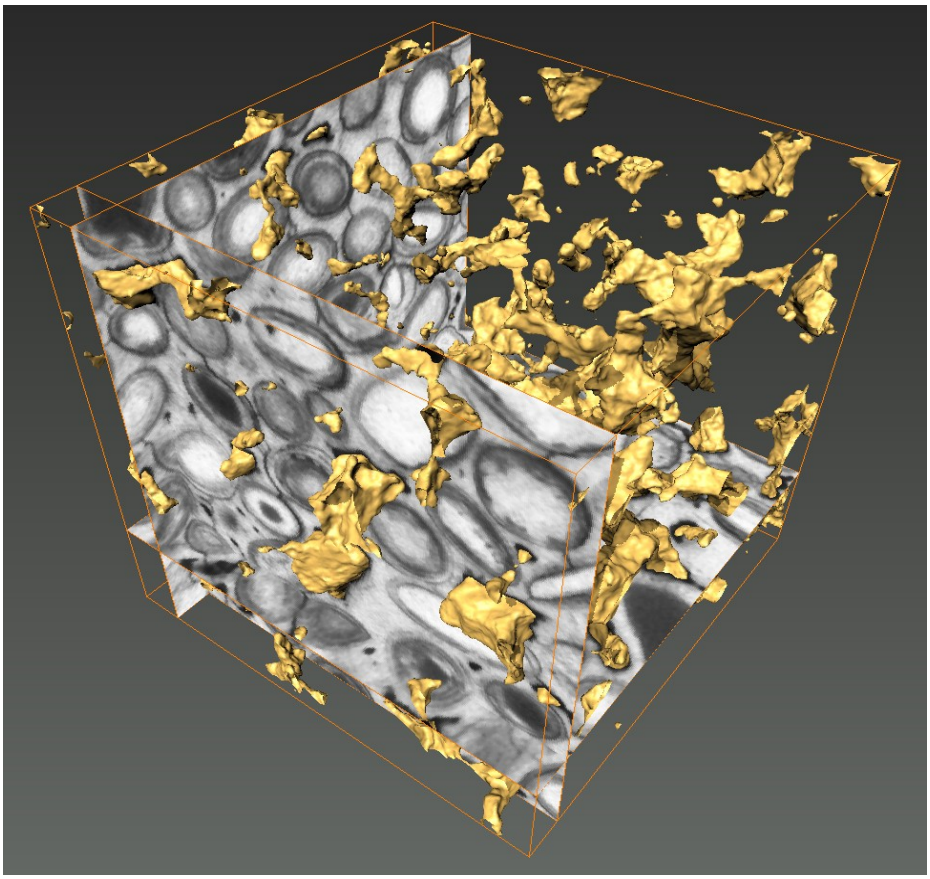

Figure 2.15. Oolite 400^3 pixels cube from microCT images with intergranular porosity in yellow.

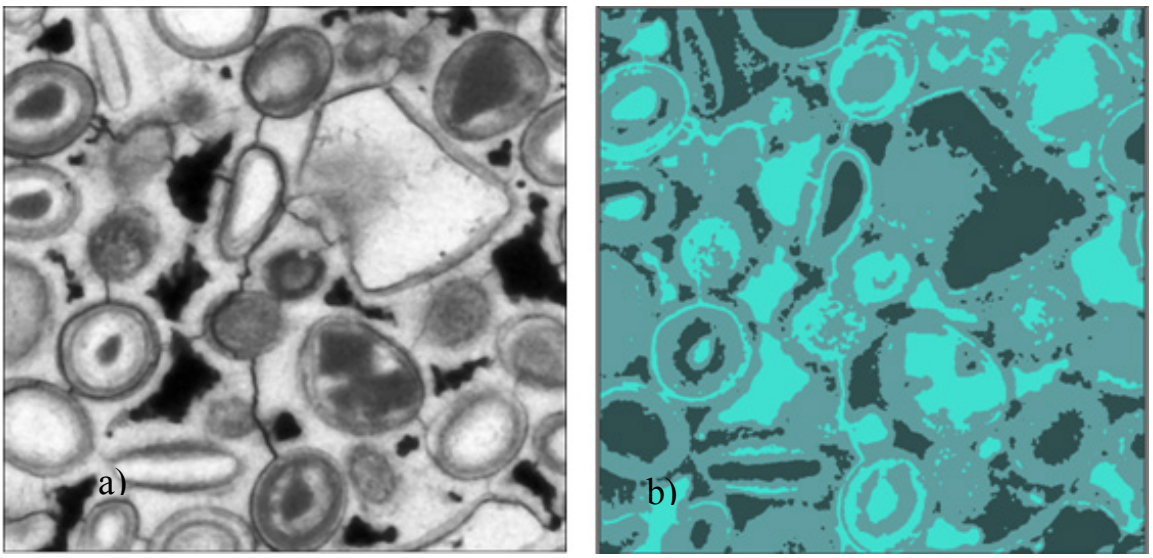

Figure 2.16: Oolite microCT image in grey scale (a) and segmented microCT image (b) showing 3 phases: pore space (blue), soft calcite (grey) and stiff calcite (dark grey)

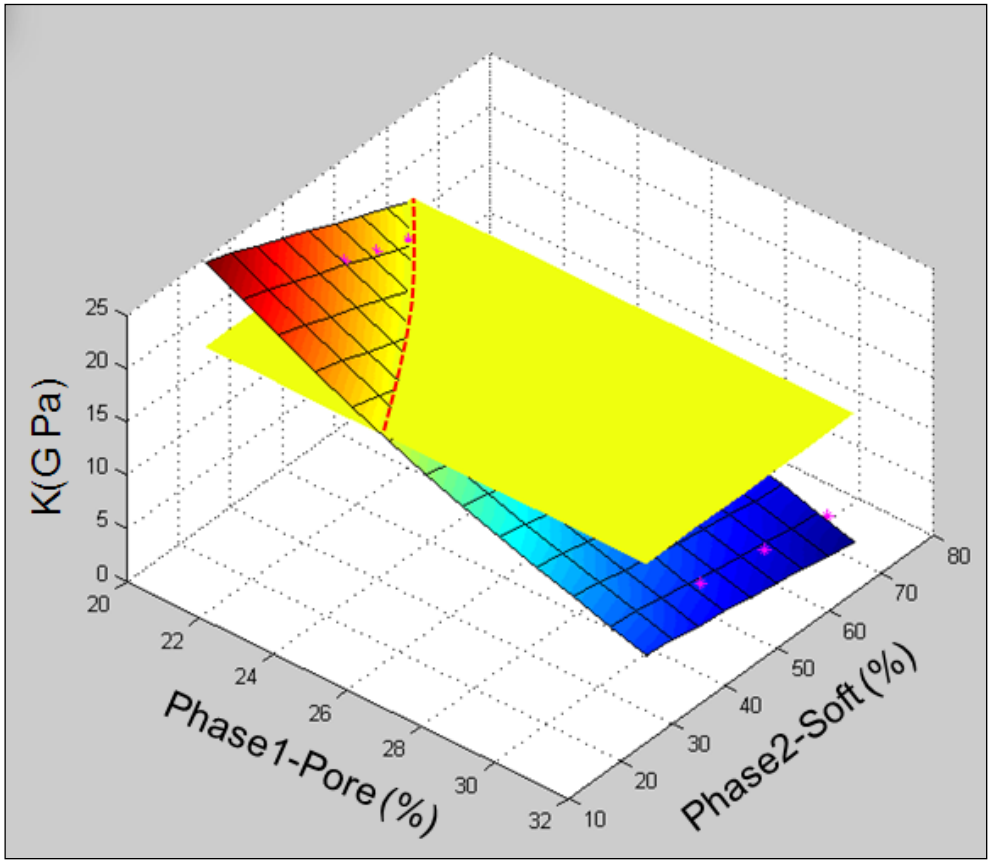

Figure 2.17. Bulk modulus from elastic modelling as a function of porosity and soft/stiff calcite ratios. The bulk modulus from ultrasonic measurements is in yellow.

Simulated elastic moduli are used to generate a surface of all possible solutions in a 3D domain (Figure 2.17). The interception of the surface with the plane K=16.7 GPa that represents the bulk modulus obtained by ultrasonic measurements (yellow surface in Figure 2.17) gives a line (red) of all possible solutions constrained by the experimental results. The surface of solutions given by the FEM modelling can be used to show the carbonate evolution with time if we assume that the soft calcite emerged as a result of partial dissolution of the stiffer calcite phase.

2.6. Conclusions

The nanoindentation technique has been shown to be practically useful for measuring the elastic parameters of the mineral constituents of a complex oolitic carbonate sample. The results obtained from the nanoindentation technique allow separation of two calcite phases with Young's moduli of 144 GPa and 56 GPa. These two phases can also be identified in microCT images due to different X-ray attenuation values.

Exact 3D distribution of the two calcite phases obtained from microCT images by segmentation has been used for the simulation of elastic moduli of the carbonate sample.

The bulk and shear moduli simulated from microtomographic images using mineral moduli based on nanoindentation are in a good agreement with the results of ultrasonic laboratory measurements.

The effect of nano- and some micro-porosity, undetectable by microCT images, is also taken into account in our workflow: we considered here that the smaller values of hardness obtained from nanoindentation are probably caused by calcite dissolution at nano- and micro-scales.

More indentation points can give a statistical representation of the Young modulus for the whole sample and can better discriminate the phases. The only estimated parameter in our workflow is the Poisson ratio, but it was shown from our simulations that it does not significantly affect elastic properties estimations. At the same time, the results are very sensitive to calcite segmentation and more research in this area is needed.

The technique shown here can be used to quantify calcite elastic parameters from any sample of carbonate reservoir. It can help to elucidate some anomalous trends in well logs and seismic data interpretation.

CHAPTER 3

GASSMANN FLUID SUBSTITUTION IN CARBONATES: SONIC LOG VERSUS ULTRASONIC CORE MEASUREMENTS

3.1. Background

The technique of Gassmann fluid substitution is widely used in the industry to understand how elastic properties change when samples are saturated with different fluids (Smith et al., 2003). However, the applicability of Gassmann's equations and the fluid substitution technique to carbonate rocks is still a subject of debate due to the fact that the derived saturated elastic properties do not always agree with the measured data (Wang, Z. 2000, Baechle et al., 2005, Adam, L. et al., 2006, Vanorio, T., et al., 2007 and Agersborg, 2008). Most of these analyses are based on laboratory measurements, with little or no constraints from field environments. Laboratory measurements are usually performed at ultrasonic frequencies, while Gassmann theory gives moduli in the low-frequency limit. Thus one possible reason for the discrepancy between the measurements of the saturated elastic properties from Gassmann predictions is variation of the saturated moduli with frequency (dispersion). If this is the case, then the discrepancy might not exist when the measurements are performed at lower frequencies, such as seismic (Hz) or sonic logging (KHz) frequencies. Since laboratory measurements of dynamic moduli at these frequencies are not feasible, it appears particularly useful to compare Gassmann predictions with field observations. Sonic logs appear to offer such an opportunity. Indeed, on one hand, the sonic frequency (about 10 KHz) is much lower than in ultrasonic measurements. On the other hand, the wavelength is not too large (about 50 cm), which allows us to consider the rock to be approximately homogeneous within one wavelength. The aim of this chapter is to compare velocities obtained with Gassmann's equations with those measured by the sonic log. To this end, we follow here the robust method proposed by Mavko et al. (1998): use the dry velocities from the laboratory measurements, perform fluid substitution using Gassmann's equations, and compare the result with the sonic log data. Grochau and Gurevich (2009) demonstrated the applicability of this approach to

data from a sandstone reservoir in the Campos Basin, offshore Brazil. We perform a similar analysis for carbonates data (core measurements and logs) from a cretaceous reservoir in the Santos Basin, offshore Brazil. Our samples are from an interval of 18 meters continuously sampled at a depth of more than 5000 meters. Compressional and shear velocities in a range of confining stress, density and porosity were measured in 50 samples covering the entire interval.

3.2. Methodology

To compare how Gassmann's fluid substitution technique is effective we have to compare the modelling results against the elastic properties derived from the sonic logs. A rigorous quality control of all parameters is fundamental to this procedure.

First of all, the 50 carbonate samples are dried under dry room conditions to perform the ultrasonic measurements. Two pairs of piezoelectric transducers are positioned at the sample's corners (top and base) to acquire shear and compressional velocities. A sinusoidal pulse of 500 KHz is propagated through the sample and the time of flight is registered. To determine the stress dependency of elastic properties, the sample is immersed in a pressure chamber with hydraulic oil. In this case the confining pressure varies from 1000 to 6000 psi. The porosity of the samples is measured in the laboratory using a porosimeter with nitrogen injection.

Secondly, a good estimation of the reservoir effective pressure is necessary to compare with laboratory data. The reservoir effective pressure P_{Effec} is obtained from the relation

$$P_{Effec} = Ah_w + B(h_r - h_w) - \eta P_{por} \tag{3.1}$$

where A and B are ocean water and lithostatic pressure gradients, h_r and h_w are reservoir and water depths (measured from sea surface), η is the effective stress coefficient and P_{por} is the pore pressure obtained from the Repeated Formation Test (RFT) of the well. This method is very basic and may not be very accurate. In particular, it ignores the effect of tectonic stresses. However it has been calibrated by Petrobras and provides a good estimate of effective pressure, especially if the depth interval of interest is not too large.

The next step is to use the dry laboratory measurements at the effective stress (P_{Effec}) determined using equation 3.1 and estimate the saturated bulk modulus $K_{sat,}$ using Gassmann's relation

$$\frac{1}{K_{sat}} = \frac{1}{K_g} + \frac{\phi\left(\frac{1}{K_f}-\frac{1}{K_g}\right)}{1+\phi\left(\frac{1}{K_f}-\frac{1}{K_g}\right)/\left(\frac{1}{K_{dry}}-\frac{1}{K_g}\right)}, \tag{3.2}$$

where K_{dry} and K_g are respectively dry and grain bulk moduli, and ϕ is total porosity. The porosity is measured in the lab and also estimated from well logs. The dry modulus K_{dry} is known from laboratory ultrasonic measurements. By using this modulus in Gassmann equation, we assume that the dispersion of the dry moduli is negligible. The grain bulk modulus can be taken as that of calcite (i.e., 70 GPa). This commonly used value would be sufficient for high-porosity rocks. However for very small porosities the saturated modulus computed with Gassmann equation 3.2 becomes very sensitive to the grain modulus, and independent estimation of the modulus of the mineral may be in order. To get an effective bulk modulus, a range of K_g can be used to find the best fit between modelled and measured elastic moduli. Finally, equation 3.2 requires an estimate of the fluid bulk modulus. The entire interval of interest is saturated with brine. The brine density ρ_w was estimated from the salinity and confining pressure at the reservoir level using the Geolog crossplot displayed in Figure 3.1. Brine velocity was computed as a function of salinity, temperature and depth from equation (Mackenzie, 1981)

$$\boldsymbol{c(D,S,T) = 1448.96 + 4.591\,T - 5.304\,10^{-2}\,T^2 + 2.374\,10^{-4}\,T^3 + 1.340\,(S-35)}$$

$$\boldsymbol{+1.630\,10^{-2}\,D + 1.675\,10^{-7}D^2 - 1.025\,10^{-2}\,T(S-35) - 7.139\,10^{-13}\,T\,D^3,} \tag{3.3}$$

where c is the brine velocity, D is depth in meters, S is salinity in parts per thousand and T is temperature in degrees Celsius. Brine bulk modulus can then be computed as $K_w = \rho_w c^2$ (in our case we obtain K_w = 4 GPA for the water salinity of 250.000 ppm).

Using equations 3.2 and 3.3, we can calculate the saturated bulk modulus K_{sat} from the laboratory measurements of the dry modulus K_{dry}. This can be compared with the saturated bulk modulus derived from P- and S-wave velocities obtained from the well log. However, since in our case the shear log is not available, the comparison between measured and modelled can be made for the P-wave modulus: $\boldsymbol{M = \rho V_p^2}$ and $\boldsymbol{V_p^2 = K + 4\mu/3}$.

3.3. Results

The porosities measured on samples are in good agreement with porosities derived from the density log (Figure 3.2). The porosity varies from almost zero to a maximum of 25%, with a deviation of 0.016 (RMS) calculated between these two porosity datasets. The porosity distribution along the interval (Figure 3.3) shows a very low porosity at the bottom increasing towards the top, indicating some increase in energy in the depositional system. The facies distribution can be seen from the thin sections in Figure 3.3, starting from mudstone at the bottom, changing to grainstone and reaching the rudstone stage at the top of the interval.

The results of Gassmann fluid substitution can be seen in Figure 3.3: the compressional-wave elastic modulus of the dry sample M_{dry} is plotted in red, derived from the well log M_{log} in black and saturated sample M_{sat} in blue. The blue bars represent the results for the grain bulk modulus range between 55 GPa and 65 GPa. We use 60 GPa as an effective bulk modulus for the calcite in this interval due the fact that when porosity tends to vanish, the saturated bulk modulus obtained from Gassmann's equations became close to the grain bulk modulus. This is the case for the deeper low porosity samples where M_{dry} is also closer to M_{log}. For lower porosities we see that the moduli computed with Gassmann equation are much closer to the well log values than the dry moduli. However there is still some discrepancy, particularly in the interval 5127-5129.5 m.

From the cross-plot of M_{log}, M_{dry} and M_{sat} (Figure 3.4) it is clear that the M_{sat} (black stars) are much closer to the black straight line (100% fit) than the M_{dry} (red stars). The RMS deviation of the differences changes from 12 GPa to 4 GPa.

Figure 3.3 we see that the effect of fluid on the elastic modulus also depends on the porosity of the rock. To explore this in more detail, Figure 3.5 shows this

dependency, where the dry P-wave elastic modulus (red) decreases from 80 GPa to less than 30 GPa as the porosity increases from almost zero to 25%. Almost parallel trends are observed with the saturated P-wave elastic modulus (blue) and the P-wave elastic modulus derived from the logs (black). Note that again there is a discrepancy between dry and log-derived P-wave moduli of about 15 GPa for the samples with a porosity of higher than 1%. This discrepancy is greatly reduced after Gassmann substitution. Figure 3.6 shows the histogram of the differences between dry and log derived P-wave elastic moduli (red) and the differences between saturated and log derived P-wave elastic moduli (blue). We restricted the histogram to samples with porosities higher than 1% for two reasons: it is where the fluid substitution is more robust and to avoid evaluation uncertainties for the low porosity rocks (some of the porosities derived from the density log were even negative, which was clearly due to log errors or uncertainty in mineral density). Again, one can see that the histogram for the differences between saturated and log derived P-wave elastic moduli is centred approximately around zero, indicating good consistency between lab and log-derived saturated moduli.

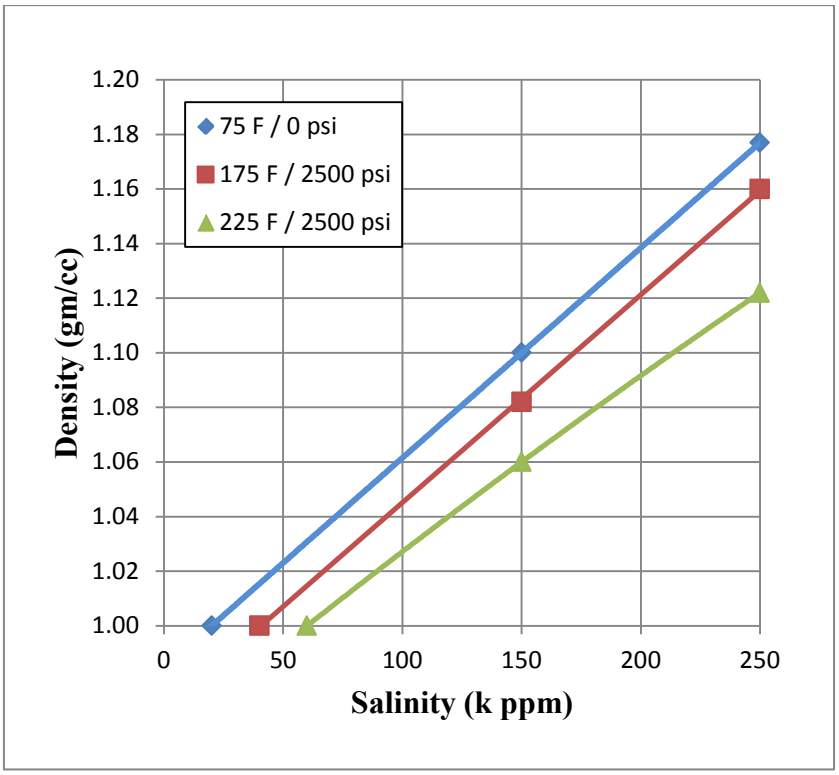

Figure 3.1. Water density as a function of salinity at different temperatures and confining pressures (Geolog).

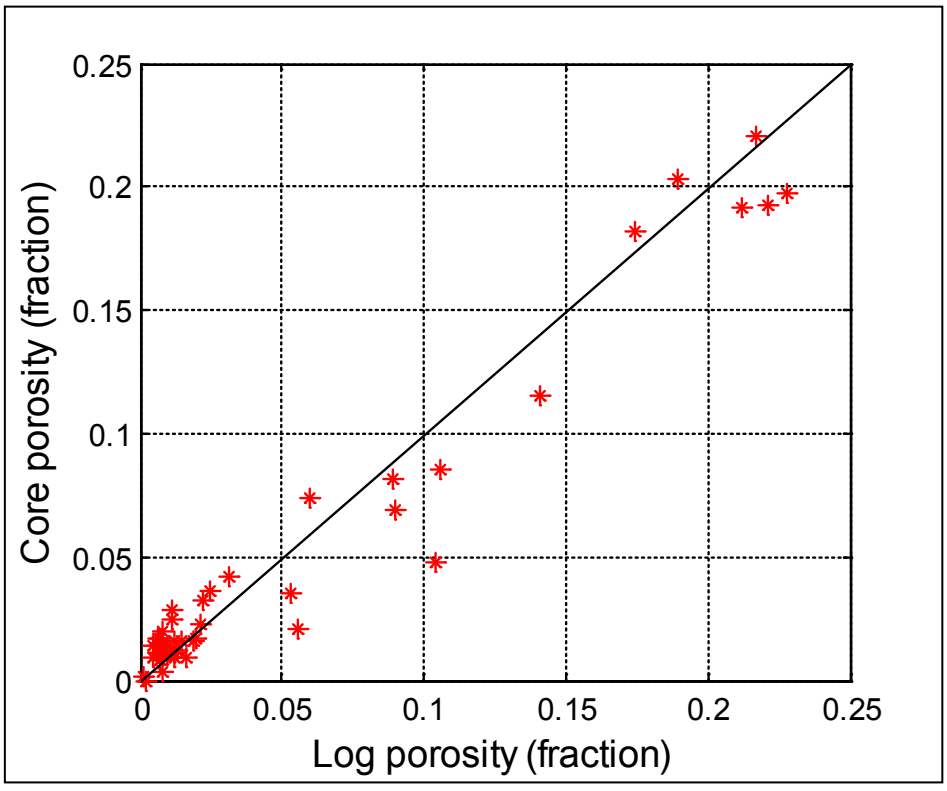

Figure 3.2. Correlation between porosity derived from the density well log and the porosity measured on the samples. These two porosity datasets show RMS deviation of 0.016.

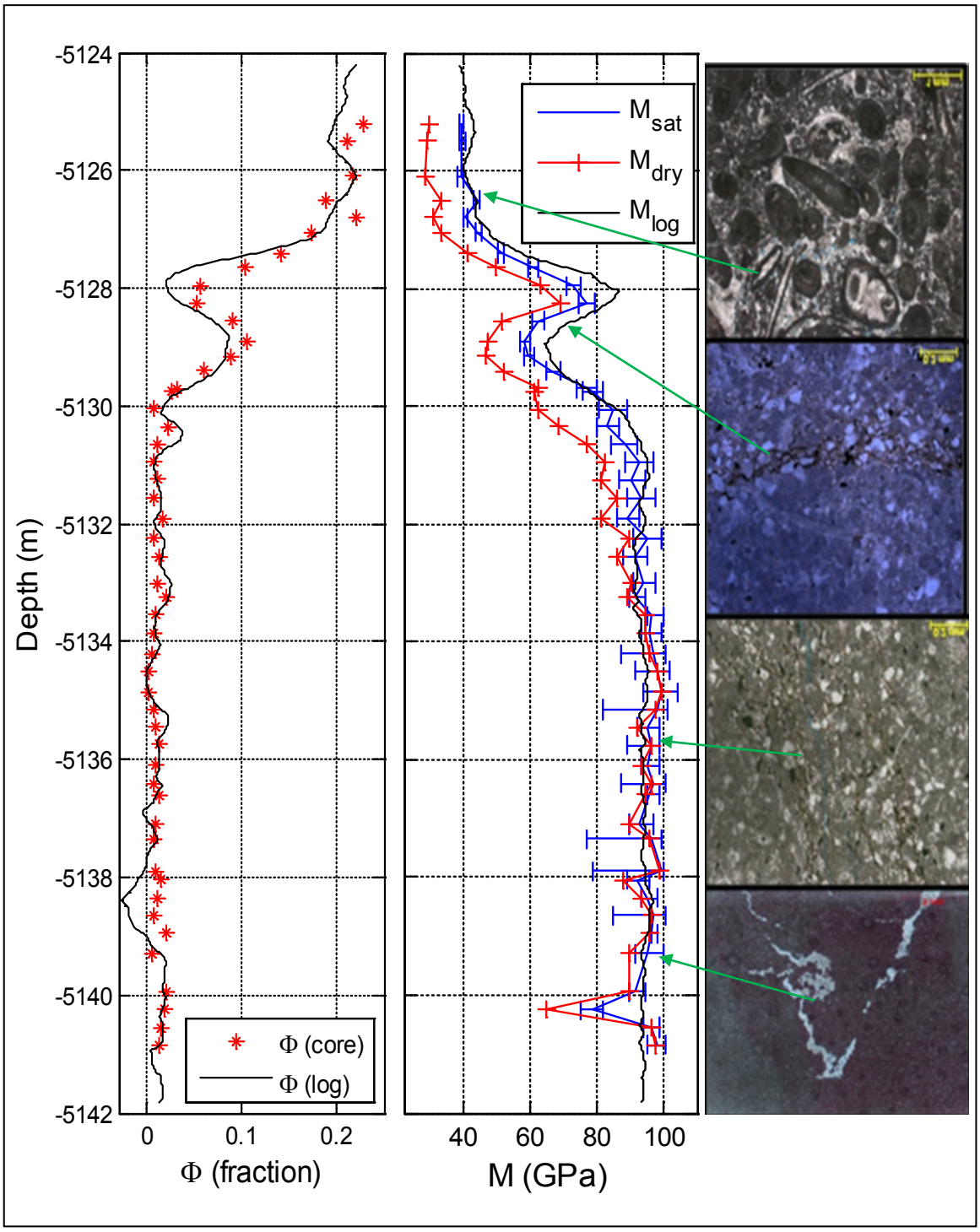

Figure 3.3. Porosity ϕ measured in 50 carbonate samples (stars in red) showing good agreement with porosity derived from the density log (black). In the middle, P-wave elastic modulus M_{dry} from lab dry measurements (red) and M_{log} from the well log (black) and the resulting M_{sat} of fluid substitution using Gassmann (blue). The blue bars represent the possible range of the grain bulk modulus bounds. On the right, thin sections show the facies distribution, from mudstone at the base, grainstone in the middle to rudstone in the top interval.

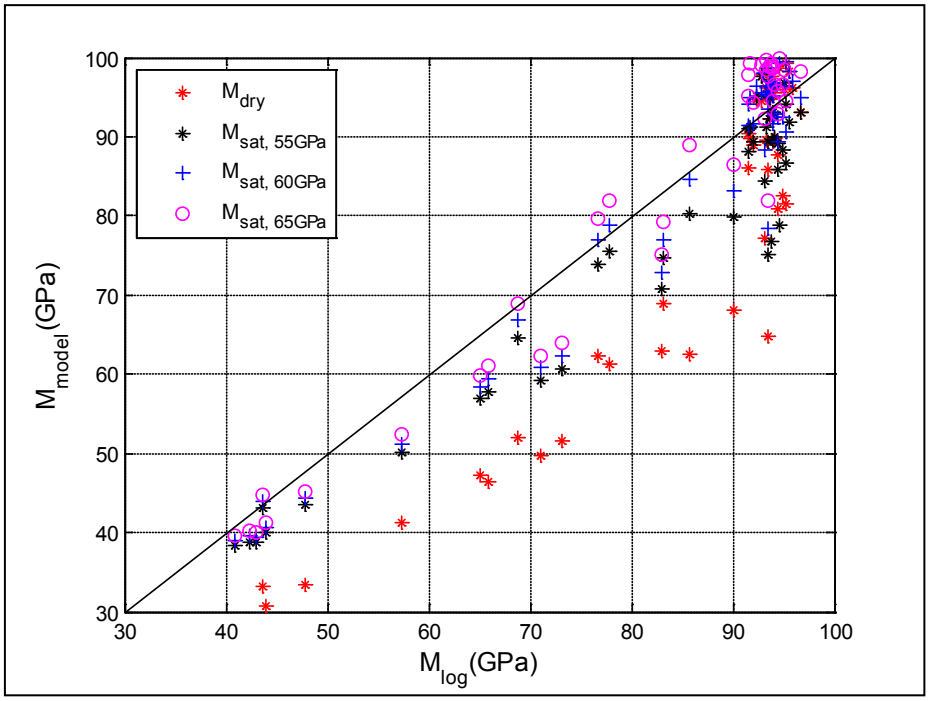

Figure 3.4. Correlation between P-wave elastic modulus derived from the sonic well log and the dry (red) and saturated moduli obtained using using Gassmann equation with K_{grain} of 55 GPa (blue), 60 GPa (black) and 65 GPa (purple).

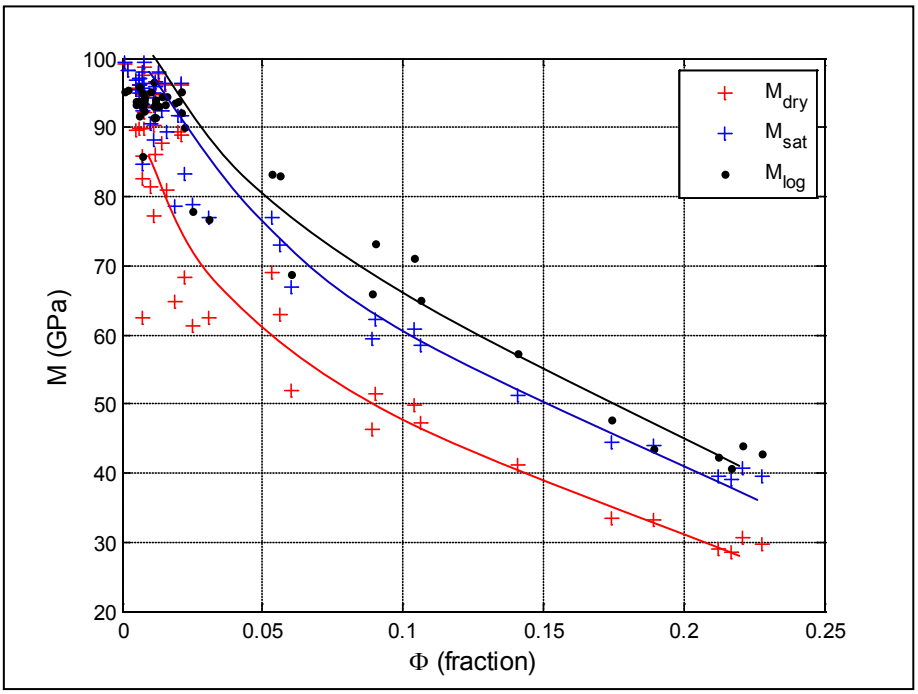

Figure 3.5. P-wave elastic moduli of dry rock (red) saturated using Gassmann (blue) and derived from well logs (black). The dashed lines are the main trends showing the moduli dependency on the porosity. Notice the agreement of the elastic moduli saturated by Gassmann and the elastic moduli derived from well log.

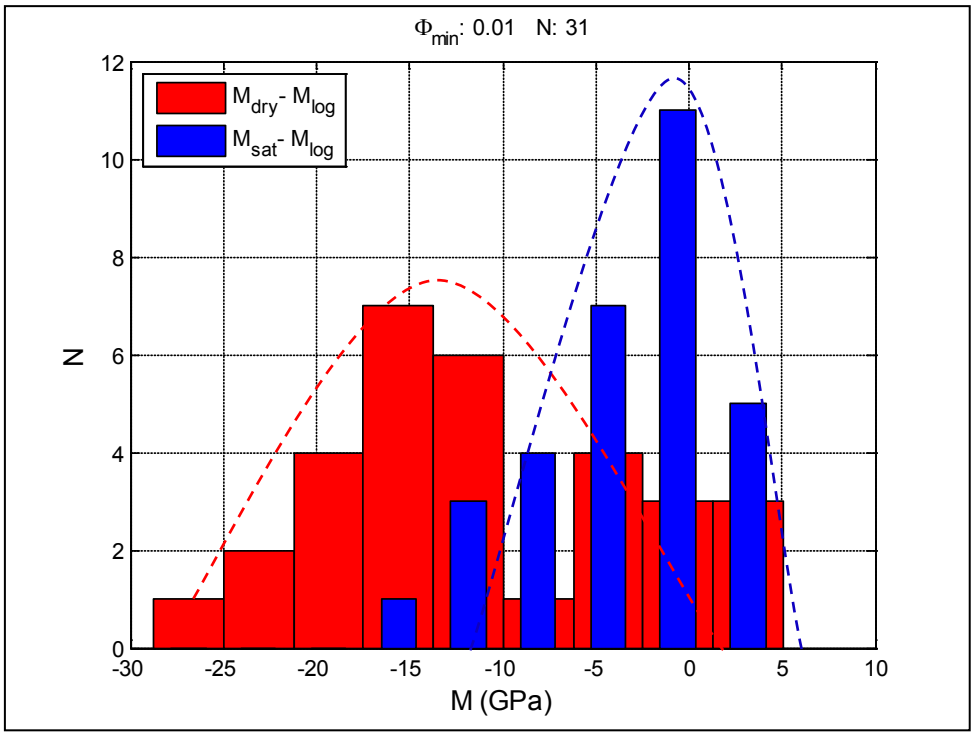

Figure 3.6. Histogram showing that the differences between dry M_{dry} and log derived P-wave elastic moduli M_{log} are much higher (15 GPa) than the differences after Gassmann substitution M_{sat} and log derived P-wave elastic moduli M_{log} (4 GPa). This histogram is restricted to samples with a porosity of higher than 1% and they are fully saturated with brine.

3.4. Conclusions

We showed that the P-wave elastic modulus obtained from Gassmann fluid substitution in carbonates using ultrasonic measurements of dry samples are in a better agreement with the P-wave elastic modulus derived from well sonic and density logs than the dry moduli. However the P-wave moduli obtained from Gassmann equations underestimate those obtained from logs by up to 6-8%, which corresponds to an error in Vp of up to 3-4%. The samples, in this case fully saturated with brine, are from depths greater than 5000 meters from a reservoir in the Santos Basin, offshore Brazil. This is only one example and similar studies for different carbonate reservoirs are required to assess applicability of Gassmann fluid substitution on other basins. The work flow tested here can be used in quantitative seismic interpretation and time lapses studies. The main condition for such a workflow is the availability of ultrasonic measurements on samples from a relatively small depth interval. This is essential because the fluid substitution effect on elastic moduli is comparable to statistical variation of the moduli for a given porosity (due to the rock heterogeneity and measurements errors).

CHAPTER 4

ROLE OF COMPLIANT POROSITY IN STRESS DEPENDENCY OF ULTRASONIC VELOCITIES

4.1. Introduction

Understanding the stress dependency of elastic properties of rocks is important for a variety of applications such as reservoir characterisation, overpressure prediction and quantitative interpretation of time-lapse seismic data. Most commonly, the dependency of elastic wave velocity, *V,* on stress is described by a combination of linear and exponential terms (Eberhart-Phillips et al., 1989; Zimmerman et al., 1991)

$$V(P) = A + KP - Be^{-PD}\ , \tag{4.1}$$

where P is confining pressure and A, K, B, and D are fitting parameters that provide the best agreement with the measured data. A number of authors explained the exponential term in equation 4.1 by the presence and closure of pores with a wide spectrum of aspect ratios (Zimmerman, 1991; Tod, 2002). However, Shapiro (2003) showed that the experimentally observed stress dependency (equation 4.1) can be explained by the presence (and closure) of only two types of pores, namely, stiff porosity ϕ_s, which decreases linearly with the increasing confining stress, and soft or compliant porosity ϕ_c, which is defined as the difference between the total porosity ϕ minus stiff porosity ($\phi_c=\phi-\phi_s$) (Walsh, 1965; Mavko and Jizba, 1991). Stiff porosity ϕ_s, is composed of equant pores, with an aspect ratio (ratio of the minimum to the maximum dimensions of the pore) normally larger than 0.1 (Zimmermann et al., 1986). The remaining porosity is the soft or compliant porosity ϕ_c, with an aspect ratio of less than 0.01.

The existence of compliant porosity in rock was reported by many authors (e.g., Wang and Simmons, 1978; Mavko and Jizba, 1991; Schmitt and Li, 1995; Morrow and Lockner, 1997). Shapiro (2003) provided a simple theoretical model of the stress dependency of rocks based on the concept of dual (stiff plus compliant) porosity. According to this dual porosity concept, the pore space of the rock can be divided into two classes of pores: stiff pores, that are largely unaffected by stress (up to typical stress

levels encountered at reservoir conditions) and compliant pores, whose closure controls the stress dependency of rock properties. Independently, Liu et al. (2008) derived analogous equations based on similar assumptions. Later the stress sensitivity theory of Shapiro (2003) was extended to anisotropic rocks (Shapiro and Kaselow, 2005).

A row of studies use the theory to describe behaviour of various isotropic and anisotropic rocks, for instance, Becker et al. (2007), Pervukhina et al. (2008a, b) and De Paula et al. (2008). Another useful application of the dual porosity approach was discovered by Pervukhina et al. (2010) who suggested a method which allowed estimation of bulk compliant porosity in sandstones using stress dependencies of their elastic compressibilities. To extend the method for the case of anisotropic rock, Pervukhina et al. (2011) employed a generic approach to media with discontinuities developed by Sayers and Kachanov (1995) as results of Shapiro and Kaselov (2005) were demonstrated to be applicable to a specific case of discontinuities with equal normal and shear compliances. Theoretical equations were obtained for a specific case of a medium with TI symmetry and applied to derive bulk compliant porosity in shales from stress dependencies of their five elastic constants. The acquired compliant porosity and its properties were shown to be depth-dependent and can be used for developing depositional trends of shales.

The stress sensitivity approach of Shapiro (2003) provides an appealingly simple interpretation of equation (4.1) and can be applied to estimate bulk compliant porosity (Pervukhina et al., 2010), which can be further used for a variety of important practical geophysical applications. However, this approach is not widely used yet because of the limited number of studies that provide experimental verification of this approach for different types of rocks.

In this chapter we examine the applicability of the dual porosity concept to carbonate rocks and explore the behaviour of parameters that control the stress dependency of carbonates in comparison with other rocks. Specifically, we study the behaviour of compliant porosity and aspect ratio as functions of total porosity, density and dry bulk modulus of a variety of samples. The data that are studied here are obtained from ultrasonic measurements on 29 carbonate samples from the Santos Basin, 6 carbonate samples from Agersborg et al. (2008) and 70 sandstones from Han et al. (1986). In particular, the carbonate samples from the Santos Basin are the same used in

the previous section, representing the sampling of 30 meters of continuous core from a depth of more than 5000 meters.

4.2. Compressibility of a dual porosity matrix

If we follow Mavko and Jizba (1991) and assume that compliant porosity is the porosity that can be closed at confining stress of about 100 MPa and the stiff porosity reduces linearly when the stress increases, the total porosity and zero pressure P=0 can be written as follows

$$\phi(0) = \phi_c + \phi_{s0} \tag{4.2}$$

and at confining pressure P_h of about 100 MPa is equal to

$$\phi(P_h) = \phi_{s0} - \Delta\phi_s \,. \tag{4.3}$$

Here, ϕ_c, ϕ_{s0} and $\Delta\phi_s$ are equal to compliant, stiff porosity at zero confining pressure and variation in stiff porosity due to the pressure increase. If we further assume (following Shapiro, 2003) that the closure of compliant porosity does not affect the decrease of stiff porosity, we can assume that in linear approximation perturbation of dry compressibility C_d (the reciprocal of the bulk modulus) with variation in stresses is equal to

$$C_d(\phi_{s0} - \Delta\phi_s, \phi_c) = C_{ds}\left[1 - \theta_s\phi_s + \theta_c\phi_c\right] \tag{4.4}$$

where $C_{ds0}=1/K_h$ is the drained compressibility of a hypothetical rock with the compliant porosity closed and stiff porosity is equal to $\phi_{s0}=\phi_s(0)$. θ_s and θ_c are the pressure sensitivity coefficients for stiff and compliant porosity, respectively, can be further written as

$$\theta_s = \frac{1}{C_{ds0}}\frac{\partial C_d}{\partial \phi_s} \text{ and } \theta_c = \frac{1}{C_{ds0}}\frac{\partial C_d}{\partial \phi_c} \,. \tag{4.5}$$

We can neglect the second term in the square brackets in 4.4, as variations in compliant porosity is of the same order of magnitude as compliant porosity and θ_s is much smaller than θ_c (Shpiro, 2003; Takei, 1998) and rewrite 4.4 as follows

$$C_d\left(\phi_{s0} - \Delta\phi_s, \phi_c\right) = C_{ds}\left[1 + \theta_c\phi_c\right]. \tag{4.6}$$

Substituting 4.6 into the Betti reciprocal theorem (Zimmerman et al.,1986)

$$\frac{d\phi}{dP} = \frac{1}{K_g} - (1-\phi)C_d \tag{4.7}$$

and neglecting ϕ in comparison with unity, we obtain an equation of pressure dependency of stiff and compliant porosity

$$\frac{d\phi_s}{P} + \frac{d\phi_c}{P} = C_{gr} - C_{ds} - \theta_c\phi_c C_{ds}\ , \tag{4.8}$$

where C_g=1/K_g is the grain compressibility.
If compliant porosity is closed equation 4.8 can be written as

$$\frac{d\phi_s}{P} = C_{gr} - C_{ds}\,. \tag{4.9}$$

Thus, for arbitrary compliant porosity

$$\frac{d\phi_c}{P} = -\theta_c\phi_c C_{ds}\,. \tag{4.10}$$

Equations 4.9 and 4.10 can be rewritten as integral pressure dependencies of the stiff and compliant porosities

$$\phi_s = \phi_{s0} - P\left(C_{ds0} - C_g\right) \tag{4.11}$$

and

$$\phi_c = \phi_{c0}e^{-\theta_c C_{ds0}P}, \tag{4.12}$$

where $\phi_{s0}=\phi_s(0)$ and $\phi_{c0}=\phi_c(0)$ are values of the stiff and compliant porosity in the unstressed rock. If we substitute equations 4.11-4.12 into equation 4.7, stress dependencies of elastic compressibility on stress can be obtained as explicitly

$$C_d(P) = C_{ds0}[1 - \theta_s(C_{ds0} - C_g)P + \theta_c\phi_{c0}e^{-\theta_c C_{ds0}P}]. \quad (4.13)$$

The stress sensitivity coefficient θ_c for compliant porosity can be related to the characteristic aspect ratio α_c of the compliant pores by the equation for bulk modulus of an elastic medium with a dilute concentration of ellipsoidal cavities (Christensen, 2005; Mavko et al., 1998; Kuster and Toksöz, 1974)

$$\theta_c = \frac{K_h(3K_h+4\mu_h)}{\pi\alpha_c\mu_h(3K_h+\mu_h)}. \quad (4.14)$$

Here K_h and μ_h denote elastic moduli of the rock without compliant pores, and stiff porosity equal to ϕ_{s0}. Thus equations 4.13-4.14 imply that the exponential decrease of the elastic moduli with the increase of confining pressure is achieved by the progressive closure of compliant pores of a (approximately) constant aspect ratio, rather than by the change of the aspect ratio. However, the overall pore shape distribution does change because the compliant porosity changes much more rapidly than the stiff porosity. The values of the coefficient θ_c obtained by fitting equations 4.13 to experimental pressure dependencies of the elastic moduli yield aspect ratios in the range $0.3\cdot10^{-4}$ - $0.03\cdot10^{-4}$. Note also that roughly speaking, the coefficient θ_c is on the order of α_c^{-1}; in other words, the characteristic crack closing pressure is

$$P_c = K_h / \theta_c = \alpha_c K_h . \quad (4.15)$$

In next sections we estimate compliant porosity from stress dependencies of elastic compressibilities of the rock (Pervukhina et al., 2010). Then we investigate correlations of the compliant porosity with other parameters and its effects on the elastic properties of carbonates and other rocks.

4.3. Workflow

Pervukhina et al. (2010) suggested that it is possible to estimate compliant porosity using the equation 4.13 from compressibility calculated from experimentally measured ultrasonic velocities. Soft porosities estimated with this method then can be compared with the ones estimated from strain measurements. First compressibilities and soft porosities are obtained as follows.

1. For each pressure, the dry bulk modulus K_{dr} is obtained using the standard equation $K_{dr} = \left[V_P^2 - (4/3)V_S^2\right]\rho_0$ and compressibility as $C_{dr} = K_{dr}^{-1}$.
2. We will obtain soft and stiff porosity from a non-linear fitting of experimentally measured $\Delta C_{dr}(P)$ as a ratio of the coefficient before the exponential to the exponent as predicted by equation (4.13). We use non-linear Levenberg-Marquardt algorithm (Levenberg, 1944; Marquardt, 1963) for approximation of all exponential dependencies. We fitted experimentally measured compressibilities with equation 4.13 to get the best fit values of the stiff limit C_{drs} and then calculated $\Delta C_{dr}(P) = C_{dr}(P) - C_{drs}$. Hereafter, we refer to this soft porosity as predicted. Softand stiff porosities calculated with this method for one of carbonate samples are shown in Figure 4.1.

   We will also compute the variation of total porosity with pressure for the samples for which strain measurements with pressure are available and estimate soft and stiff porosity as follows.
3. Since experiments are performed with isotropic pressure, we assume that ε_{ax} represents the strain in all three directions. Then, the volumetric strain (relative variation of the sample volume *v* with pressure) is $\varepsilon = (v - v_0)/v_0 = 3\varepsilon_{ax}$, where v_0 is sample volume at zero pressure. At the same time, the relative change of total volume v_{gr} of solid grains with pressure is $\varepsilon_{gr} = (v_{gr} - v_{gr0})/v_{gr0} = -C_{gr}P/(1-\phi)$, where v_{gr0} is total volume of solid grains at zero pressure and C_{gr} is the compressibility of the solid grain material, which is assumed known from mineralogical analysis. Since pore volume at any pressure is the total volume minus grain volume, $v_\phi = v - v_{gr}$, using Zimmerman *et al.* (1986), we get:

$$\phi = \frac{v_\phi}{v} = 1 - \frac{v_{gr}}{v} = 1 - \frac{\left[1 - C_{gr}P/(1-\phi)\right]v_{gr0}}{(1+\varepsilon)v_0}. \quad (4.16)$$

For small deformations, this gives

$$\phi = 1 - (1-\varepsilon)(1-\phi_0) - C_{gr}P = \phi_0 + (1-\phi_0)\varepsilon + C_{gr}P. \quad (4.17)$$

Note that for $P > 0$, total volumetric strain ε is negative, and is larger by absolute value than the grain deformation $C_{gr}P$; therefore, according to equation (4.17), porosity will decrease with increasing pressure, as it should.

4. We will estimate stiff porosity by fitting a linear trend to the porosity-pressure dependency in the uppermost part of the measurement pressure range (Walsh, 1965; Mavko and Jizba, 1991).
5. Once stiff porosity is defined, the compliant (soft) porosity is defined at each pressure as the difference between total and stiff porosity. Hereafter, we call this porosity measured.

4.4. Validation of the dual porosity model for sandstones

Pervukhina et al. (2010) verified the model of Shapiro (2003) using ultrasonic measurements taken from six samples of sandstones. The sandstone core samples from the Northwest Shelf of Australia were recovered from depths of 1700-2000 metres. The stress dependent velocity measurements were partially published in Siggins and Dewhurst (2003). Cores for testing were cut with diameters of 38 mm and length of 76 mm. Lithologies were homogeneous over the length of the cores. The porosity ranged from 7–24% with an average clay content of 4%. The sandstones were tested dry under ambient conditions in a triaxial cell to a maximum effective confining pressure of 60 MPa. Full waveforms were recorded for P- and S-waves at nominal centre frequencies of f_P = 800kHz and f_S = 400 kHz, respectively. The strain measurements were taken during the loading and unloading pressures. More details of the sandstones and

experimental method can be found in Siggins et al., (2001) and Siggins and Dewhurst (2003).

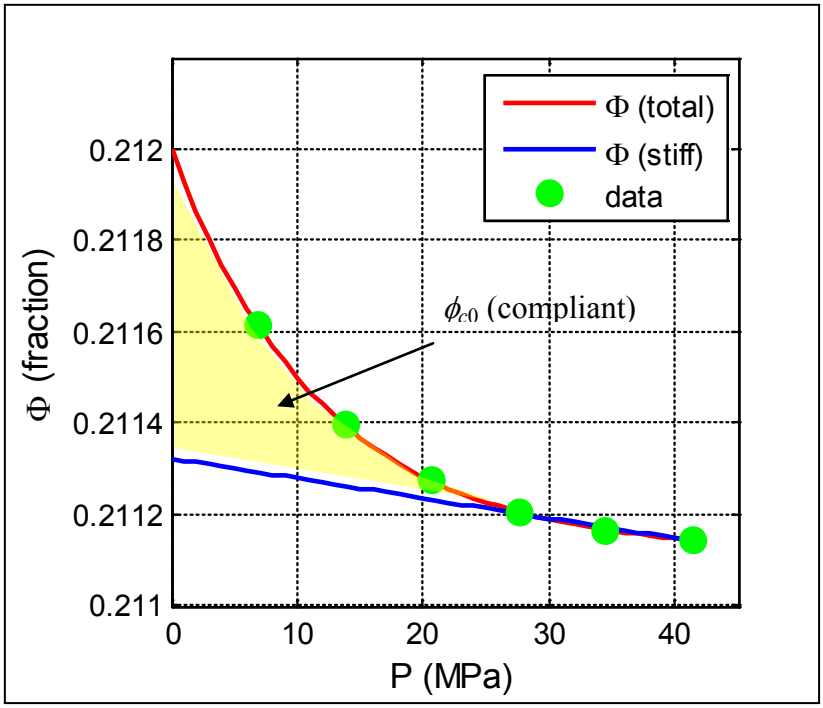

Figure 4.1. Pressure dependency of total (circles and red line), stiff (blue line) and compliant (yellow) porosity in a grainstone carbonate from the Santos Basin, Brazil.

Using the workflow described above, we re-analyse here the data for the six sandstones to compare compliant porosities obtained from porosity measurements and from the analysis of stress sensitivity of compressibility for all the confining stresses. Figure 4.2 shows the compliant porosities estimated from the fitting of the elastic compressibility plotted against the compliant porosities obtained from the measurements of the axial lengths of the samples. Colours represent confining pressures from 0 (blue) to 60 MPa (red). We can see that these compliant porosities are in a good agreement.

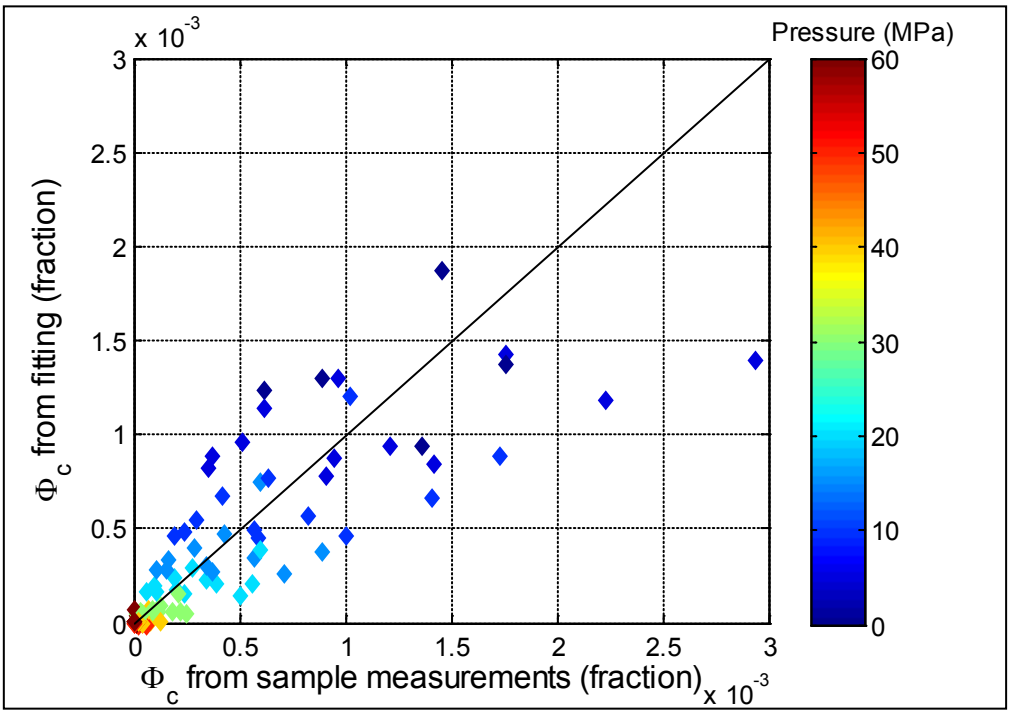

Figure 4.2. Cross plot of the compliant porosities ϕ_c estimated from sample axial length measurements against the values estimated from fitting compressibilities according to Shapiro (2003) theory. The colours represent the confining pressure from 0 to 60 MPa.

4.5. Compliant porosity in carbonates

We expect that the dual porosity model could be a good model for carbonates, because cracks and oblate pores are very common to these rocks (De Paula et al., 2008, De Paula et al., 2009). As strain measurements are unavailable for our carbonate samples we use an altered workflow that will be described in detail in Chapter 5 to calculate compliant and stiff porosity of the carbonates. Variations of total, soft and stiff porosities with pressure are shown in Figure 4.1 for one of the reservoir carbonate samples from the Santos Basis, offshore Brazil. Here we employ the method suggested by Mavko and Jizba (1991) to subdivide total porosity into stiff and compliant part. The red line tangent to the blue curve at higher pressures is the stiff porosity. The difference between the total porosity (red) and stiff porosity (blue) is defined as compliant or soft porosity. Figure 4.1 shows that total measured porosity of 21.16% at 5 MPa decreases to less to 21.12% at the confining pressure of 40 MPa (red).

The elastic bulk moduli verses porosity relationship for the 29 carbonate samples from the Santos Basin, offshore Brazil at reservoir confining stress has already been investigated in the previous chapter. We now analyse the stress dependency of elastic moduli of these samples using the concept of dual porosity. The ultrasonic shear and compressional velocities were measured on these dry samples at the confining pressures from 5 GPa to 40 GPa. In Figure 4.3 the experimentally measured dry bulk moduli are plotted vs. the total porosity. Note that the dry bulk moduli decrease from 60 GPa to less than 20 GPa when porosity increases from ~0% to 23%. For the porosities less than 2% there is almost no correlation between the dry bulk moduli and the porosities. This corresponds to the domain of mudstone facies (see Figure 3.5 in Chapter 3). When the confining stress increases from 5 to 40 MPa (shown by colour change from blue to red), the bulk moduli increase dramatically while the decrease in total porosity is almost imperceptible.

The compliant porosity for each of the 29 samples of the Santos carbonates is estimated using the methodology described in Section 4.2. Then the compliant porosity at zero pressure ϕ_{c0} that is estimated from the fitting coefficients of equation 4.9 is used for the further analysis. In Figure 4.4 the dry bulk moduli are plotted against compliant porosities for all 29 samples of Santos carbonates. Note the sharp decrease in the bulk moduli from 60 GPa to less than 10 GPa while the compliant porosity increases from ~0 to 0.1%.

Figure 4.5 shows the cross-plot of dry compressibility $C_{dry} = 1/K_{dry}$ against the compliant porosity. In this case a positive linear trend is observed with the increase of C_{dry} from 0.02 to 0.1 GPa while the compliant porosity increases from ~0 to 0.1%.

In Figure 4.6 we cross-plot compliant porosity at zero confining stress ϕ_{c0} versus total porosity ϕ for the same carbonate samples. Note that the relationship between compliant and total porosity is broadly linear, in particular, for the total porosities above 5%. The compliant porosity increases from 2.0×10^{-4} to 1.0×10^{-3} while total porosity increases from 5.0×10^{-2} to 2.2×10^{-1}.

In Figure 4.7, the compliant porosity at zero stress ϕ_{c0} is plotted against the dry rock density. We observe that the compliant porosity broadly decreases from 1.0×10^{-3} to almost zero while dry rock density increases from 2100 kg/m^3 to 2700 kg/m^3. The dashed blue line shows the trend. This negative linear trend can be explained by the fact

that the compliant porosity shows positive linear correlation with the total porosity as was shown in Figure 4.6.

In Figure 4.8 we plot the characteristic aspect ratio (obtained with equation 4.14) of the compliant pores as a function of total porosity for Santos carbonates. The aspect ratio of compliant pores increases from less than 1.0×10^{-4} to almost 0.8×10^{-3} while the total porosity increases from 0.05 to 0.23. Note that for the total porosity less than 0.3 all ranges of the alpha are possible: the carbonate facies classified as mudstone are in this domain.

To compare the results obtained for the Santos carbonates with parameters for other reservoir rocks, in Figure 4.9 we plot the compliant porosity at zero confining stress ϕ_{c0} as a function of total porosity ϕ for distinct datasets. The dataset includes the 29 carbonate samples from 30 meters continuous interval from the Santos Basin discussed previously (blue), 6 carbonate samples from Agersborg et al. (2008) (black) and 70 samples of sandstones from Han et al. (1986) (green and red). A good correlation between compliant and total porosity are found for both Santos carbonates (dashed blue line) and for Fontainebleau sandstones (dashed red line). The remaining Han's sandstones and Agersborg carbonates show a very broad positive linear trend, probably because they came from different locations, have different mineralogy or belong to distinct facies. The trends between the total and compliant porosities are different for each type of sedimentary rock and even for sandstones with different mineralogy as can be seen from the comparison of the trends of the Fontainebleau sandstones and the Santos carbonates with other samples.

In Figure 4.10 we cross-plot the aspect ratio of compliant porosity at zero confining stress as a function of total porosity for the same dataset. The correlation between aspect ratio and total porosity is clear for the Santos carbonates with porosities above 0.05 and for the Fontainebleau sandstone (5 of 7 points are aligned). For the remaining samples, the aspect ratio of compliant porosity exhibits no correlation with total porosity.

Dry bulk moduli K_{dry} against total porosity ϕ and compliant porosity at zero pressure ϕ_{c0} for sandstone samples (Han et al., 1986) are shown in Figures 4.11 and 4.12, respectively. For this dataset, the bulk moduli broadly decrease while porosity increases. A much better correlation exists between the dry bulk moduli of the

sandstones and compliant porosity (Figure 4.12). Dry bulk moduli decrease from 30 GPa to 4 GPa while the compliant porosity increases from almost 0 to 2.7 x 10^{-3}.

A, B, K and *D*	fitting parameters
α_c	aspect ratio of a compliant pore
C_d	rock dry compressibility
C_{d0}	dry compressibility of a rock with compliant porosity closed
C_g	grain dry compressibility
ε	volumetric strain
ϕ	total porosity
ϕ_c	compliant porosity
ϕ_{c0}	compliant porosity at zero confining pressure
ϕ_s	stiff porosity
ϕ_{s0}	stiff porosity at zero confining pressure
ϕ_0	porosity at zero confining pressure
f_P	centre frequencies for P waves
f_S	centre frequencies for S waves
K_d	dry bulk modulus
K_g	grain Bulk modulus the
K_h	rock Bulk modulus at high pressures
μ_h	rock shear modulus at high pressures
θ_c	pressure sensitivity coefficient for compliant porosity
θ_s	pressure sensitivity coefficient for stiff porosity
v	volume of sample
v_ϕ	volume of pores
v_{gr}	volume of grains
v_0	volume of sample at zero pressure
P	confining pressure
P_c	characteristic crack closing pressure
V	elastic wave velocity
V_p	compressional elastic wave velocity
V_s	shear elastic wave velocity

Table 4.1. Notations

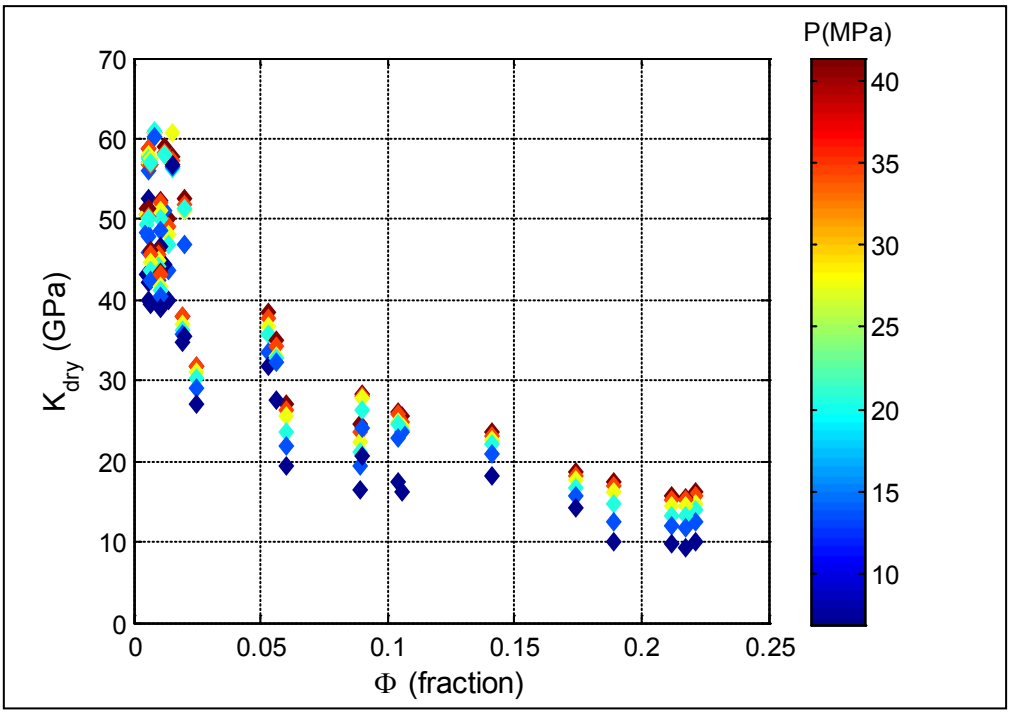

Figure 4.3. Dry bulk moduli K_{dry} against total of porosity ϕ for 29 carbonate samples from the Santos Basin, offshore Brazil. Note the increase in bulk modulus while total porosity decreases.

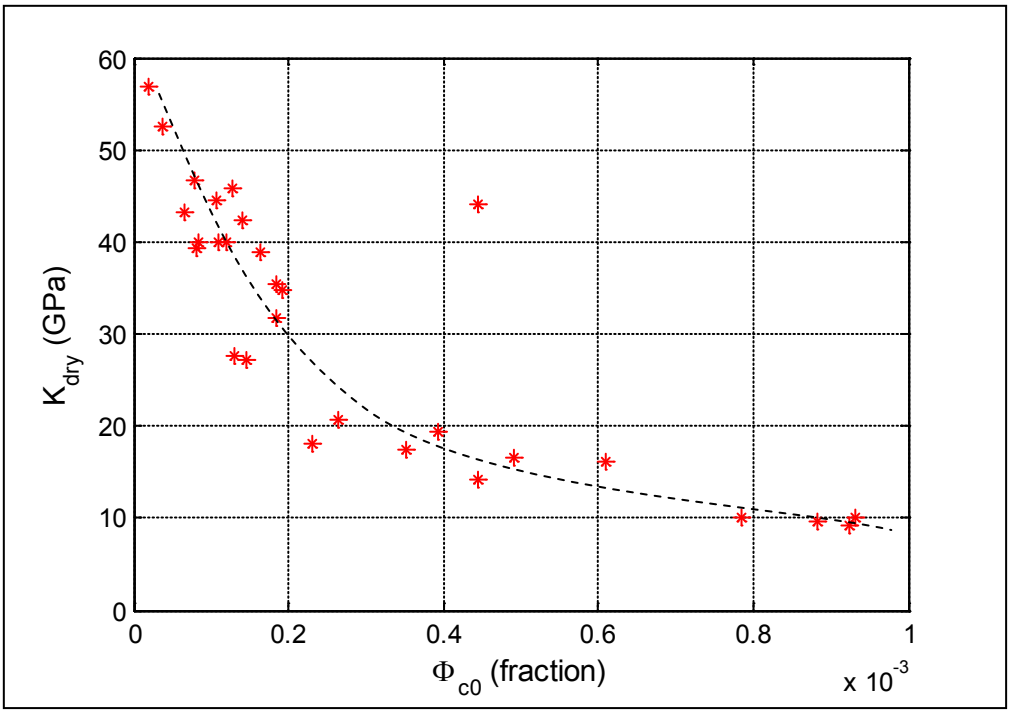

Figure 4.4. Dry bulk moduli against compliant porosity for Santos carbonates. Note the decrease in bulk moduli while compliant porosity increases. The compliant porosity here is estimated from fitting data using Shapiro (2003) theory.

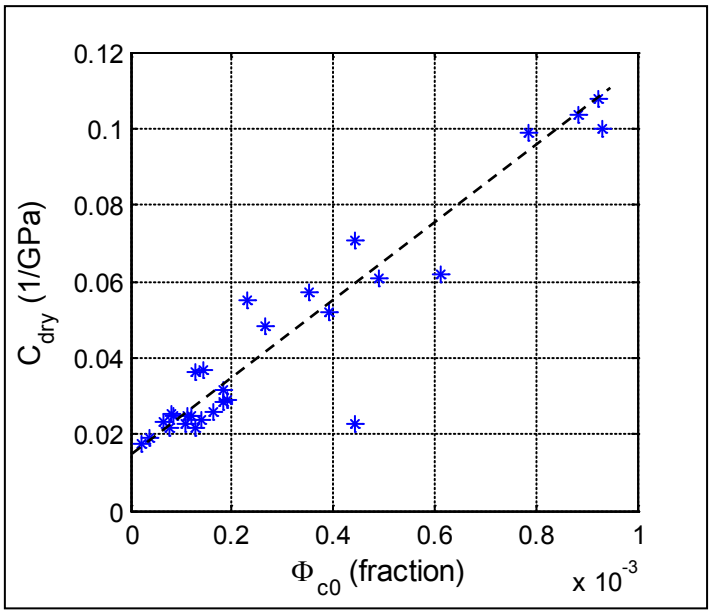

Figure 4.5. Dry compressibility against compliant porosity for Santos carbonates. Note the linear relationship between the compressibility and the compliant porosity.

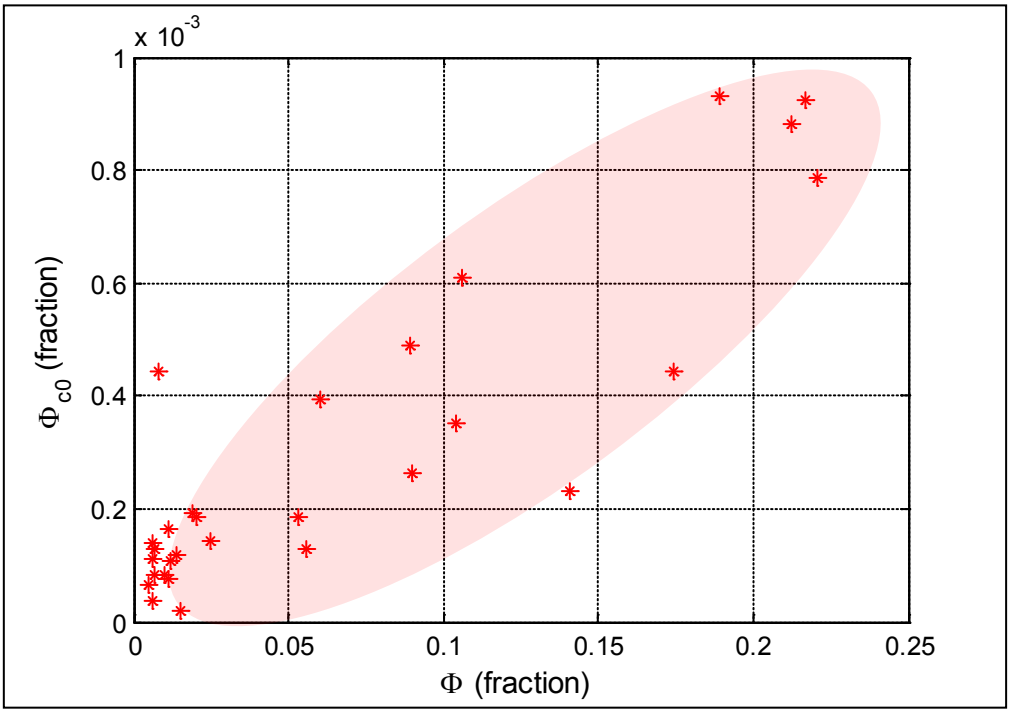

Figure 4.6. Compliant porosity at zero confining stress ϕ_{c0} as a function of total porosity ϕ for Santos carbonates. Note the positive broadly linear relationship between compliant and total porosity, in particular, for porosities above 5%.

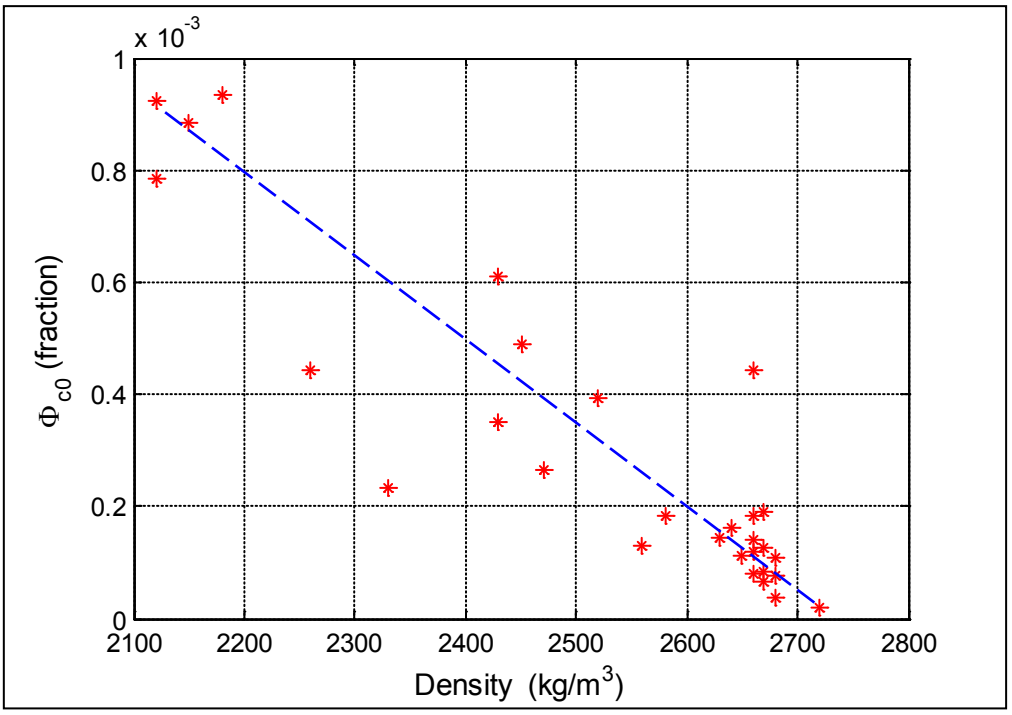

Figure 4.7. Compliant porosity at zero confining stress as a function of dry bulk density for Santos carbonates. The compliant porosity exhibits a linear decrease when the rock density increases.

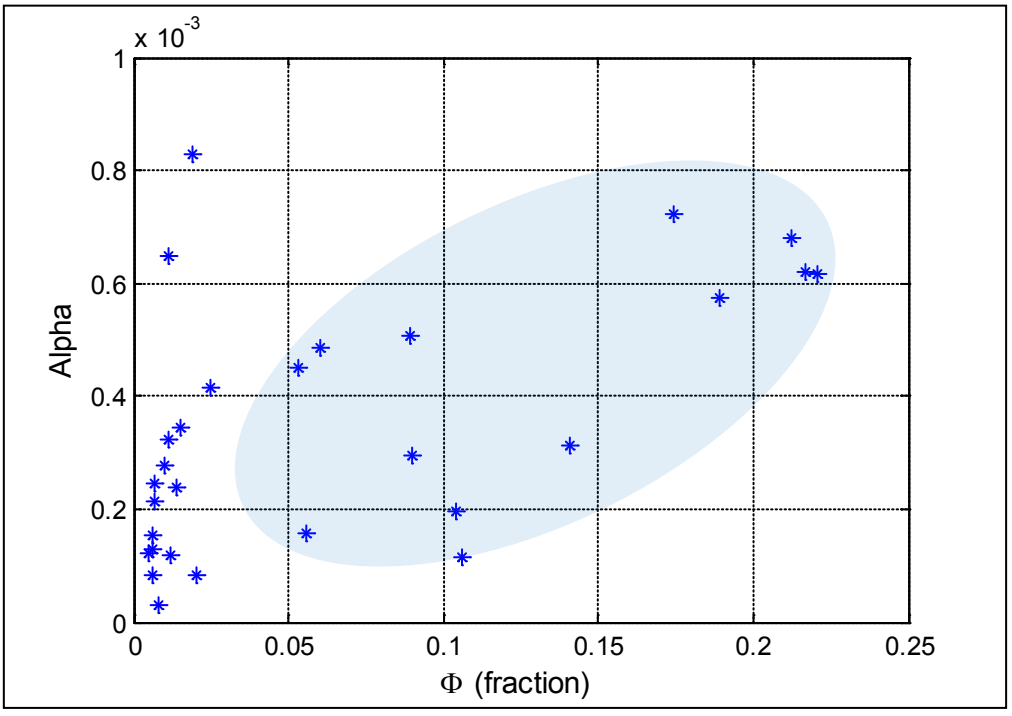

Figure 4.8. Aspect ratio of compliant pores as a function of total porosity for Santos carbonates. Note the increase of the aspect ratio of compliant pores with the increase of total porosity.

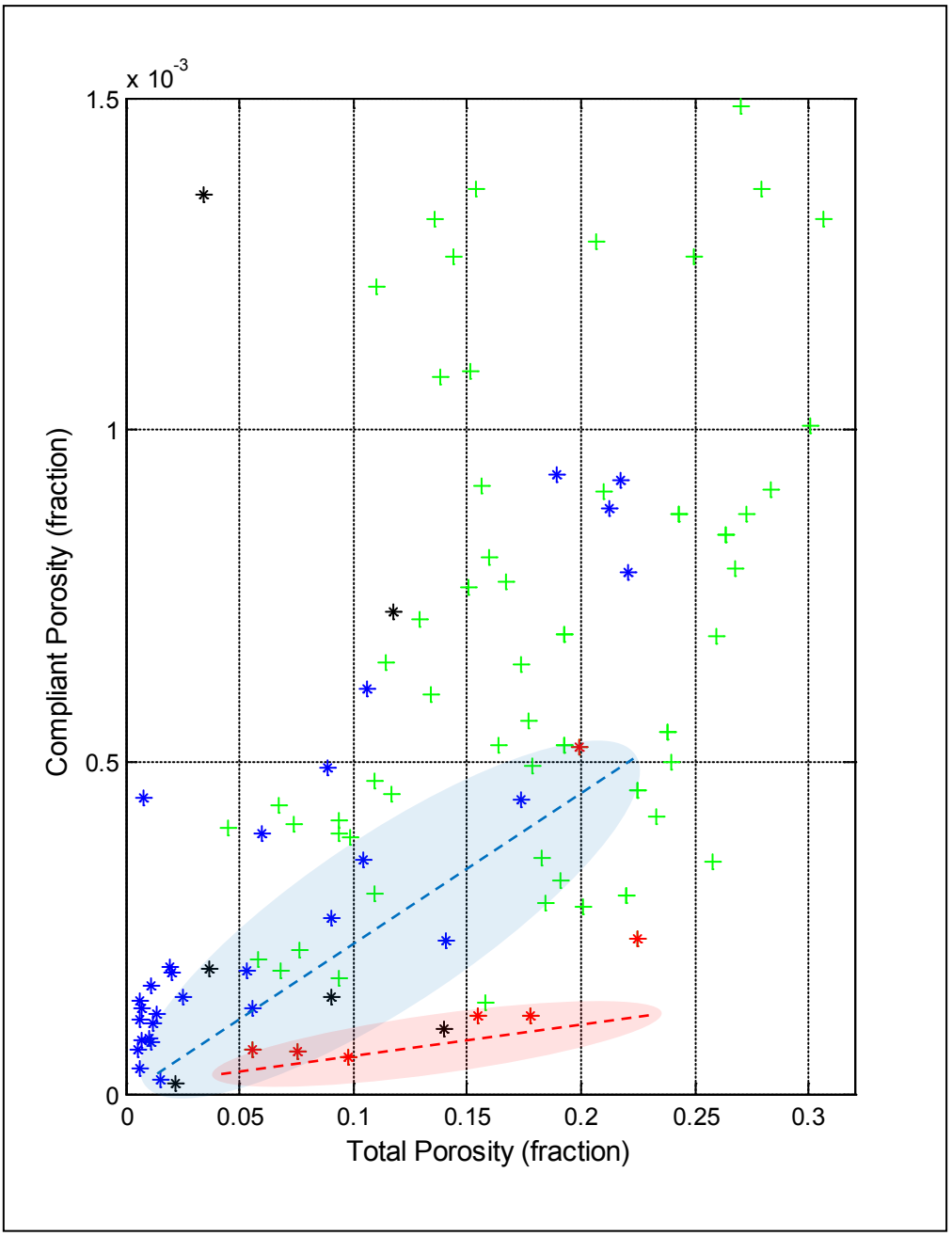

Figure 4.9. Compliant porosity at zero confining stress ϕ_{c0} vs. total porosity ϕ for carbonates and sandstones. Note the good correlation of compliant and total porosity for Santos carbonates (blue stars) and Fontainebleau sandstones (red stars). The other sandstones (green crosses) and carbonates (black crosses) that came from different locations show no correlation between compliant and total porosity.

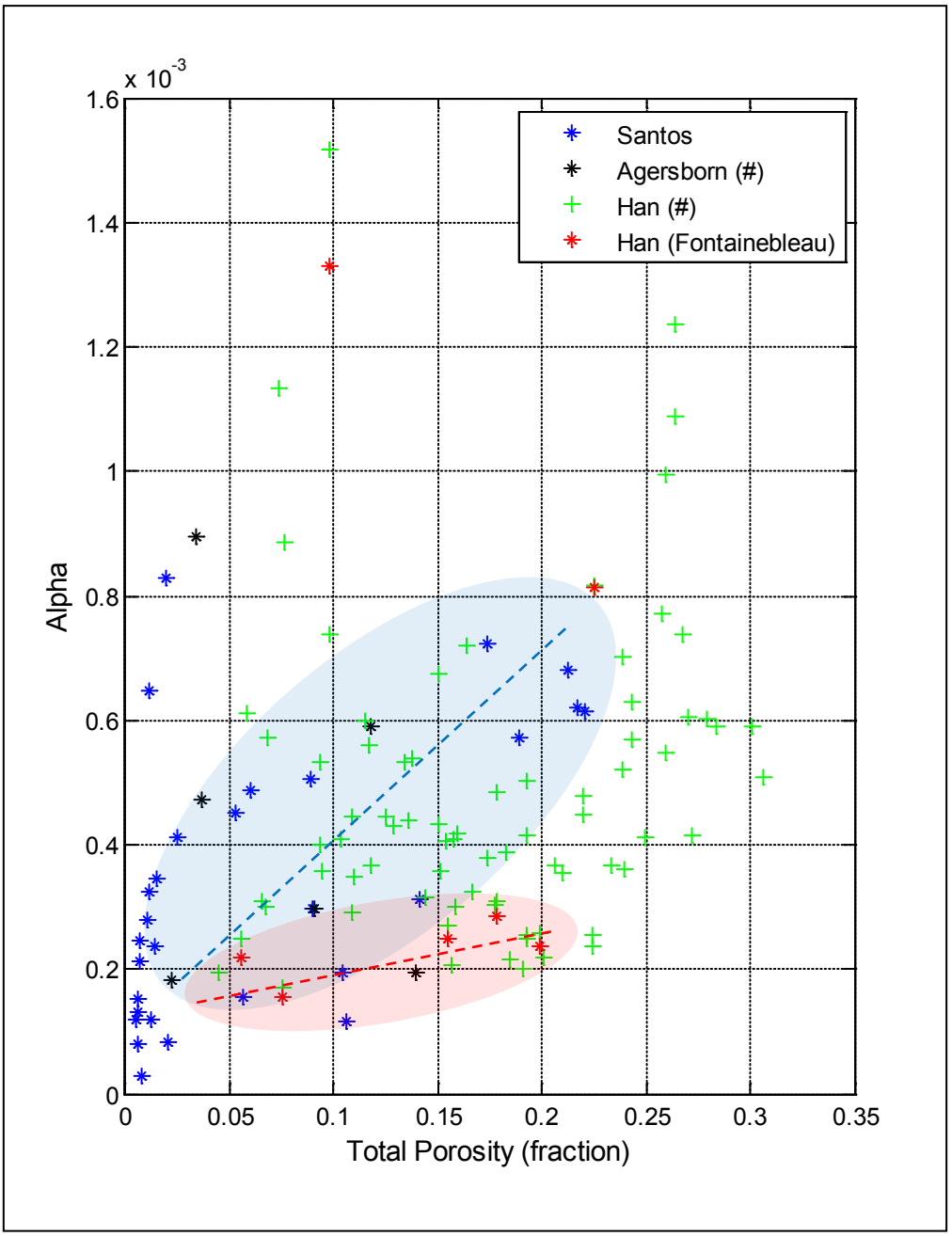

Figure 4.10. Aspect ratio of compliant porosity at zero confining stress as a function of total porosity for carbonates and sandstones. Note the reasonable correlation of the aspect ratio and total porosity for Santos carbonates (blue stars) and Fontainebleau (red stars). The other sandstones (green crosses) and carbonates (black crosses) show no correlation between the aspect ratio and the total porosity.

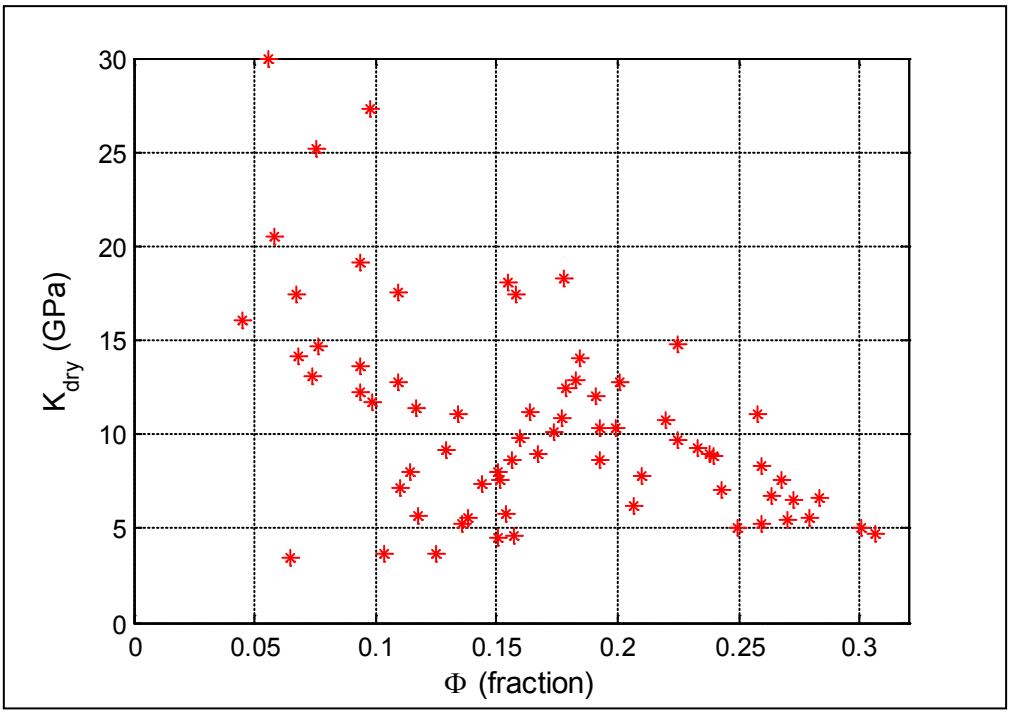

Figure 4.11. Dry bulk moduli K_{dry} against total porosity for sandstones (Han's dataset). Note that the dry bulk moduli broadly decrease with porosity increases.

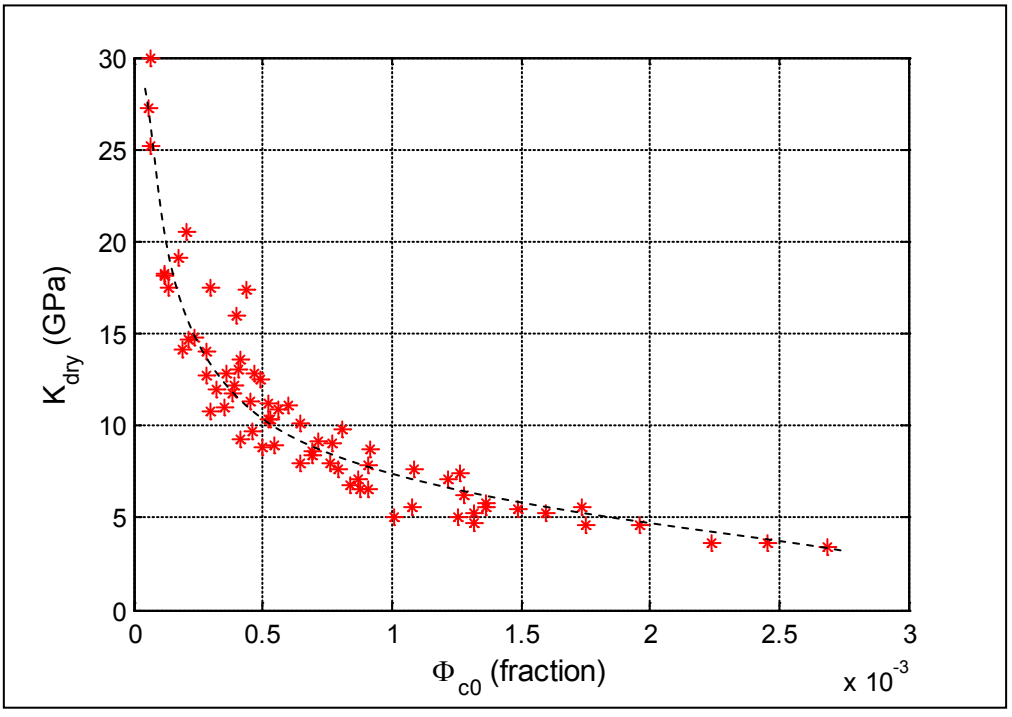

Figure 4.12. Dry bulk modulus K_{dry} against compliant porosity ϕ_{c0} for sandstones (Han´s dataset). The bulk moduli show an inverse relation with the compliant porosity. Note that these samples came from different locations and have different clay content.

4.6. Conclusions

For a suite of sandstones, the compliant porosities estimated by the fitting of stress dependencies of the compressibility are shown to be in a good agreement with the compliant porosities obtained from the variation of axial lengths of the samples for the whole range of confining stresses. This further justifies the stress sensitivity model suggested by Shapiro (2003) and confirms that the workflow suggested by Pervukhina et al. (2010) can be used to obtain the soft porosity for the cases when the porosity measurements with stress are not available.

For the 29 samples of carbonates from the Santos Basin, the compliant porosities obtained by the described method show a positive linear trend with the compressibility of the samples. The compliant porosity is proportional to the total porosity for the Santos carbonates. Density exhibits a negative trend with the compliant and total porosity. The aspect ratio of compliant pores shows a general increase with an increase of the total porosity.

A general increase of the compliant porosity with total porosity is observed for the set of 70 sandstone samples measured by Han et al. (1968). The number and diversity of the samples suggests that this general positive trend between these two types of the porosities may be universal for sedimentary rocks. This trend, however, is different for each type of sedimentary rock and even for sandstones with different mineralogy and generally cannot be used for the prediction of compliant porosity from the total one.

These results show that the approach described above can be used for enhanced characterisation of the pore space of reservoir rocks, no matter whether they are sandstones or carbonates. The relationships of compliant porosity and aspect ratio with total porosity, bulk modulus and density are shown to be robust if we constrain the analysis to the samples of the same facies or the same field. These relationships can then be used to obtain unique signatures for reservoirs and can be useful for reservoir modelling and 4D monitoring.

CHAPTER 5

MODELLING SQUIRT DISPERSION AND ATTENUATION WITHOUT ADJUSTABLE PARAMETERS

5.1. Introduction

Understanding dispersion and attenuation of elastic waves in rocks is important for consistent analysis of seismic, borehole acoustic and ultrasonic data. A major cause of elastic wave dispersion and attenuation in fluid-saturated rocks is the so-called squirt flow, that is, local (pore-scale) wave-induced flow of the pore fluid between pores of different shapes and orientations (Mavko and Nur, 1975; Mavko and Nur, 1979; Jones, 1986). When an elastic wave propagates through a fluid-saturated medium, relatively compliant pores are deformed to a greater degree than the relatively stiff ones. This difference creates local pressure gradients within the fluid phase, resulting in fluid flow and corresponding energy dissipation that continues until the pore pressure is equilibrated.

Over the last 40 years a number of theoretical models of squirt dispersion and attenuation have been proposed with different assumptions concerning the distribution of pore shapes and orientations. Most theoretical models of squirt-flow attenuation are based on the analysis of aspect ratio distributions (Mavko and Nur, 1979; O'Connell and Budiansky, 1977; Palmer and Traviolia, 1980); a comprehensive review of these earlier studies is given by Jones (1986). An alternative approach is based on the recognition that the pore space of many rocks has a binary structure (Walsh, 1965; Mavko and Jizba, 1991; Shapiro, 2003): relatively stiff pores, which form the majority of the pore space, and relatively compliant (or soft) pores, which mostly contribute for the pressure dependency of the elastic moduli (Murphy et al., 1986; Dvorkin et al., 1995; Chapman et al., 2002; Gurevich et al., 2010). In these models, the magnitude of dispersion is related to the amount of soft porosity, while the characteristic frequency of the squirt dispersion is related to the degree of compliance of the soft pores (often expressed as the characteristic aspect ratio or other characteristic geometrical parameter of these soft pores). This characteristic compliance or aspect ratio cannot be measured

directly and is often taken to be an adjustable parameter that can be obtained by fitting the model to experimental data (such as the dispersion curve measured in the laboratory). The existence of an adjustable parameter that cannot be independently measured is a weakness of all squirt models, as it impedes independent verification of these models.

Mavko and Jizba (1991) showed that the magnitude of the squirt dispersion can be related directly to the pressure dependency of the elastic dry moduli of the dry rock. At the same time, this pressure dependency also defines the characteristic compliance (or aspect ratio) of the soft pores (Walsh, 1965; Shapiro, 2003). By estimating the characteristic pore compliance from the rock's pressure dependency, we can eliminate the adjustable parameter in the squirt model. The purpose of this chapter is to establish such a workflow, and to test it against laboratory measurements.

The chapter is organized as follows. First, we briefly recall a simple theoretical model of squirt flow dispersion (as proposed by Gurevich et al., 2010) as well as a model of stress dependency of elastic moduli of dry rocks (Shapiro, 2003). We then propose the new concept of intermediate porosity to describe the pressure dependency of elastic moduli for pressures above 50 MPa. The next section outlines the workflow employed to obtain the geometrical pore space parameters from pressure dependency of the elastic moduli, and to predict the dispersion and attenuation in fluid-saturated rocks using the squirt model. This is followed by laboratory data examples where the predictions for water-saturated rocks are compared with the ultrasonic measurements.

5.2. Theoretical models

5.2.1. A squirt model

Squirt is a phenomenon of wave-induced pressure relaxation and fluid flow between pores of different shapes and/or orientations, and, more specifically, between relatively compliant and relatively stiff pores. Mavko and Jizba (1991) showed that at high frequencies (such that the fluid pressure has no time to equilibrate between pores of different stiffnesses/orientations), the effect of the squirt phenomenon on elastic properties is relatively independent of the assumptions about pore geometries. For such high frequencies, the squirt effect can be modelled via a so-called *modified frame* concept. Modified frame refers to the state of the rock in which the stiff pores are dry

while the compliant pores are saturated with a fluid. Mavko and Jizba (1991) showed that in the high-frequency limit, pressure dependency of the bulk and shear moduli $K_{\mathrm{mf}}(P)$ and $\mu_{\mathrm{mf}}(P)$ of the modified frame can be expressed as

$$\frac{1}{K_{\mathrm{mf}}(P)} = \frac{1}{K_{\mathrm{h}}} + \left(\frac{1}{K_{\mathrm{f}}} - \frac{1}{K_{\mathrm{g}}}\right)\phi_{\mathrm{c}}(P) \tag{5.1}$$

$$\frac{1}{\mu_{uf}(P)} = \frac{1}{\mu_d(P)} + \frac{4}{15}\left(\frac{1}{K_{mf}(P)} - \frac{1}{K_d(P)}\right) \tag{5.2}$$

where $\phi_{\mathrm{c}}(P)$ is the compliant porosity as a function of effective pressure P, $K_{\mathrm{d}}(P)$ and $\mu_{\mathrm{d}}(P)$ are bulk and shear moduli of the dry frame, K_{h} is the dry bulk modulus in the high pressure-limit (when all the compliant porosity is closed) and K_{g} is the bulk modulus of the solid grain material. Conversely, in the low frequency limit, the pore pressure has ample time to equilibrate between stiff and compliant pores, and thus the bulk and shear moduli of the modified frame are equal to those of the completely dry frame.

At intermediate frequencies, the fluid pressure would equilibrate partially and elastic properties would become dependent not only on pressure but also on frequency and geometry of the pore space. Murphy et al. (1986) proposed to represent the geometry of the compliant pores as flat slabs connecting stiffer pores (Figure 5.1). For granular rocks such as sandstones, stiff pores represent intergranular pores defined by the grain packing, while the flat slabs represent gaps at contacts between adjacent grains. Using the geometrical configuration proposed by Murphy et al. (1986), Gurevich et al. (2010) showed that the frequency dependent bulk and shear moduli of the modified frame are given by the following analytical expressions

$$\frac{1}{K_{\mathrm{mf}}(P,\omega)} = \frac{1}{K_{\mathrm{h}}} + \frac{1}{\frac{1}{\frac{1}{K_{\mathrm{d}}(P)} - \frac{1}{K_{\mathrm{h}}}} + \frac{3i\omega\eta}{8\,\phi_{\mathrm{c}}(P)\alpha_{\mathrm{c}}^2}} \tag{5.3}$$

and

$$\frac{1}{\mu_{\mathrm{mf}}(P,\omega)} = \frac{1}{\mu_{\mathrm{d}}(P)} - \frac{4}{15}\left(\frac{1}{K_{\mathrm{d}}(P)} - \frac{1}{K_{\mathrm{mf}}(P,\omega)}\right). \tag{5.4}$$

In equations 5.3 and 5.4, ω is the angular frequency of the wave, η is the dynamic viscosity of the pore fluid and α_{c} is the aspect ratio of the inter-granular gap (thickness over diameter). Equation 5.3 has a restriction that the fluid modulus must satisfy the condition

$$K_f \gg 8\,\phi_c \left(\frac{1}{K_d} - \frac{1}{K_h}\right)^{-1}. \quad (5.5)$$

This means that the fluid modulus should not be too small,that is, the fluid inside the crack must be a liquid. The frequency dependent bulk modulus of the rock fully saturated with the fluid K_s can be obtained from the frequency dependent modulus K_{mf} of the modified frame using Gassmann's (1951) equation

$$\frac{1}{K_s(P,\omega)} = \frac{1}{K_g} + \frac{\phi\left(\frac{1}{K_f} - \frac{1}{K_g}\right)}{1+\phi\left(\frac{1}{K_f} - \frac{1}{K_g}\right)\Big/\left(\frac{1}{K_{mf}(P,\omega)} - \frac{1}{K_g}\right)}, \quad (5.6)$$

where ϕ is the total porosity. The saturated shear modulus μ_s is equal to the shear modulus of the modified frame μ_{mf}

$$\mu_s = \mu_{mf.} \quad (5.7)$$

The saturated moduli K_s and μ_s computed with equations 5.3, 5.4, 5.6 and 5.7 are consistent with Gassmann's equation in the low-frequency limit and with Mavko-Jizba (1991) equations 5.1 and 5.2 in the high-frequency limit. Between these limits, the moduli are complex and frequency dependent, and thus the corresponding elastic waves exhibit attenuation and dispersion. Furthermore, at frequencies where visco-inertial relaxation becomes important, these equations can be combined with Biot's (1962) equations of poroelasticity to account for both squirt and local and Biot's global flow dissipation mechanisms (Gurevich and Carcione, 2011).

5.2.2. Stress dependency of the elastic parameters of a dry rock

The squirt equations 5.3 and 5.4 require knowledge of the pressure dependence of the dry bulk and shear moduli and of what fraction of the total porosity is compliant porosity. Commonly, the dependence the dry rock velocity on stress is described by a combination of linear and exponential terms (Eberhart-Phillips et al., 1989; Zimmerman, 1991)

$$V(P) = A + KP - Be^{-DP}, \quad (5.8)$$

where V is velocity (of P or S waves) in km/s, P is confining pressure in kbars, A, K, B, and D are fitting parameters that provide the best agreement with the measured

data. A number of authors explained the exponential term in equation 5.8 by the presence and closure of pores with a wide spectrum of aspect ratios (e.g., Zimmerman, 1991; Tod, 2002). However, Shapiro (2003) showed that the experimentally observed stress dependency (equation 5.8) can also be explained by the presence (and closure) of only two types of pores, namely, stiff porosity ϕ_s which decreases linearly with the increasing confining stress, and soft or compliant porosity ϕ_c which is defined as the difference between the total porosity ϕ minus stiff porosity ($\phi_c=\phi - \phi_s$) (see Walsh, 1965; Mavko and Jizba, 1991). Shapiro (2003) showed that if the pore space consists of stiff and compliant porosities so defined, then the stress dependency of its dry compressibility $C_d=1/K_d$ can be written as

$$C_d(P) = C_{ds0}[1 - \theta_s \Delta\phi_s(P) + \theta_c \phi_c(P)], \tag{5.9}$$

where $C_{ds0}=1/K_h$ is the drained compressibility of a hypothetical rock with the compliant porosity closed and stiff porosity equal to $\phi_{s0}=\phi_s(0)$, θ_s and θ_c are the pressure sensitivity coefficients for stiff and compliant porosity, respectively, and $\Delta\phi_s(P)=\phi_s(P) - \phi_{s0}$. Shapiro (2003) further showed that the pressure dependencies of the stiff and compliant porosities can be expressed by

$$\phi_s = \phi_{s0} - P(C_{ds0} - C_g) \tag{5.10}$$

and

$$\phi_c = \phi_{c0} e^{-\theta_c C_{ds0} P}. \tag{5.11}$$

where $\phi_{s0}=\phi_s(0)$ and $\phi_{c0}=\phi_c(0)$ are values of the stiff and compliant porosity in the unstressed rock, and $C_g=1/K_g$ is the grain compressibility. The linear relationship 9 between the rock compressibility obtained from ultrasonic velocities, and compliant porosity obtained from strain measurements was demonstrated for a number of sandstones by Pervukhina et al. (2010). The theoretically predicted relation that explicitly expresses the stress dependency of the dry elastic compressibility can then be obtained by combining equations 5.9 – 5.11 as follows

$$C_d(P) = C_{ds0}[1 - \theta_s(C_{ds0} - C_g)P + \theta_c \phi_{c0} e^{-\theta_c C_{ds0} P}]. \tag{5.12}$$

The relationship 5.9 between the drained compressibility and compliant porosity can be used in combination with the squirt equations 5.3 and 5.4 to obtain an explicit dependency of the elastic moduli of the saturated rock on pressure and frequency. Furthermore, the stress sensitivity coefficient θ_c for compliant porosity can be related to the characteristic aspect ratio α_c of the compliant pores by the equation for bulk modulus of an elastic medium with a dilute concentration of ellipsoidal cavities (Christensen, 2005; Mavko et al., 1988; Kuster and Toksöz, 1974)

$$\theta_c = \frac{K_h(3K_h+4\mu_h)}{\pi\alpha_c\mu_h(3K_h+\mu_h)}. \quad (5.13)$$

The use of the dilute concentration model is justified by the linear relationship 9 between the sandstone compressibility and compliant porosity (Pervukhina et al., 2010). In equation 5.13, K_h and μ_h denote elastic moduli of the rock without open compliant pores, and with the stiff porosity equal to ϕ_{s0}. Thus, equations 5.9 and 5.11 imply that the exponential decrease of the elastic moduli with the increase of confining pressure can be achieved by the progressive closure of compliant pores of a (approximately) constant aspect ratio, rather than by the change of the aspect ratio. However, the overall pore shape distribution does change because the compliant porosity changes with pressure much more rapidly than the stiff porosity. The values of the coefficient θ_c obtained by fitting equations 5.9 - 5.11 to experimental pressure dependencies of the elastic moduli yield aspect ratios in the range $0.03\cdot10^{-4}$ - $0.\ 3\cdot10^{-4}$. Note also that roughly speaking, coefficient θ_c is on the order of α_c^{-1}; in other words, the characteristic crack closing pressure is

$$P_c = K_h/\theta_c = \alpha_c K_h \quad (5.14)$$

5.3. Moderately stiff (intermediate) porosity

5.3.1. The concept of intermediate porosity

In his analysis of the contribution of the stiff porosity term in equation 5.9, Shapiro (2003) assumed that the stiff pores have aspect ratios of order 1 (so-called equant pores, Thomsen, 1995), and concluded that the contribution of the deformation of the stiff porosity is small compared to that of the compliant porosity, and thus can be

neglected. However, experimental studies (Eberhart-Phillips et al., 1989; Vernik and Hammam, 2009; Gurevich et al., 2009) show that in many cases the contribution of the stiff porosity term (that is, the term that varies linearly with pressure in the pressure range between 0 and 50 MPa) is significant. This implies that the stress sensitivity coefficient θ_s for stiff porosity is significantly larger than that for spherical or equant pores. In other words, experimental data suggest that in addition to equant pores, the stiff porosity contains pores with aspect ratios greater than $0.3 \cdot 10^{-1}$ but much less than 1. In analogy with equations 5.12 and 5.13, such porosity would decrease exponentially with the increasing pressure and close approximately at $P_s = \alpha_s K_e$, where K_e is the bulk modulus of a rock with only equant pores present (so-called Swiss-cheese rock). The modulus K_e is usually on the order of (but somewhat smaller than) the grain bulk modulus K_g. Thus, for a rock such as sandstone, P_s would be on the order of 200-2000 MPa. This is much larger than the maximum pressure typically applied in ultrasonic pressure cell experiments, and the exponential decrease of such porosity with confining pressure would look like a linear decrease in the pressure range, say, from 0 to 40 MPa.

The above analysis suggests that it is reasonable to divide the stiff porosity ϕ_s into two parts: the equant porosity ϕ_e with characteristic aspect ratio close to 1, and moderately stiff or intermediate porosity ϕ_m with a characteristic aspect ratio in the range 10^{-3} - $2 \cdot 10^{-1}$

$$\phi_s = \phi_e + \phi_m, \tag{5.15}$$

or, for the total porosity ϕ

$$\phi = \phi_e + \phi_m + \phi_c. \tag{5.16}$$

5.3.2. Stress dependency of dry moduli in the presence of intermediate porosity

By definition, the compressibility of the intermediate porosity is much higher than the compressibility of the equant porosity. Thus, the intermediate porosity will exhibit an exponential decay with increasing pressure, similar to the compliant porosity but at much higher confining pressures

$$\phi_m = \phi_{m0} e^{-\theta_m C_e P}, \tag{5.17}$$

where ϕ_m is porosity of the intermediate pores, ϕ_{m0} is the intermediate porosity at zero confining stress, θ_m is stress sensitivity of these pores and $C_e=1/K_e$ is the compressibility of the dry rock with equant pores only.

Closure of the intermediate porosity at such stresses will affect the compressibility of the rock in a similar way as closing of compliant pores affects compressibility at 0-50 MPa and its effect can be described by a similar equation

$$C_{ds}(P) = C_e[1 + \theta_m \phi_m(P)] \tag{5.18}$$

or

$$C_{ds}(P) = C_e\left[1 + \theta_m \phi_{m0} e^{-\theta_m C_e P}\right]. \tag{5.19}$$

In equations 5.18 and 5.19, C_{ds} is the compressibility of a hypothetic rock without the compliant porosity (that is, only with stiff porosity $\phi_s=\phi_e+\phi_m$ open). Furthermore, the effect of the deformation of equant porosity is neglected. For large pressures where the compliant porosity is closed (above 50-100 MPa), $C_{ds}(P)=C_d(P)$. The variation of the dry compressibility due to the combined effect of compliant and intermediate porosity can be written as

$$C_d(P) = C_e[1 + \theta_m \phi_{m0} e^{-\theta_m C_e P} + (1 + \phi_{m0})\theta_c \phi_{c0} e^{-\theta_c C_{dso} P}] \tag{5.20}$$

The stress dependency of the bulk modulus of typical reservoir sandstone is shown in Figure 5.2(a). Open circles at stresses of 5-50 MPa are the bulk moduli calculated from the experimentally measured ultrasonic velocities of St. Peter sandstone (Han et al., 1986) and the solid line shows the approximation of the moduli with equations 5.9 - 5.11. The dashed-dotted horizontal line shows the bulk modulus of the rock in the high-pressure limit, where all intermediate porosity is closed ('Swiss-cheese' limit). We calculate this limit using the coherent potential approximation (CPA) effective medium model for spherical pores (Berryman, 1980). Instead of CPA, differential effective medium (DEM) approximation (Cleary et al., 1980; Norris, 1985, Zimmerman, 1991) could be used. For porosities below, say, 0.25 and aspect ratios of

order 1, these models give similar results, but for sandstones with higher porosities CPA is more adequate (Berge et al., 1995; 1993). The dashed line is the fit of C_{ds} using equation 5.19, which shows the effect of the closure of the intermediate porosity. Figure 5.2(b) shows the effect of the compliant and intermediate porosity on the bulk modulus in the wider range of confining stresses of 5-500 MPa for the same sample. One can see that at low stresses, the effect of the closure of the intermediate porosity is almost linear.

The importance of the intermediate porosity can be demonstrated by comparing the bulk moduli measured at the highest confining stress in pressure cell experiments against estimates of the bulk moduli in the 'Swiss-cheese' limit, in which all porosity consists of equant pores. Indeed, typical values of the constant D in equation 5.8 are above 0.03 MPa^{-1} (Eberhart-Phillips et al., 1989; Shapiro, 2003), which means that at pressures above about 50 MPa we can assume the compliant porosity to be closed. Thus if all the stiff porosity consisted of equant pores (no intermediate porosity), the bulk modulus measured at the pressure of 50 MPa would be equal to that computed for spherical pores. However, the analysis of the St. Peter sandstone (Figure 5.2) shows an obvious difference of about 7 GPa between the measured bulk modulus at 50 MPa, and the predicted bulk modulus of the rock at the 'Swiss-cheese' limit, K_e computed using CPA.

Figure 5.3(a) is a plot of dry bulk modulus K_{50} at P=50 MPa against the 'Swiss-cheese' limit K_e for 66 dry sandstones with different mineralogy and clay content from different depths and locations as obtained from ultrasonic measurements of Han et al. (1986). The 'Swiss-cheese' limit K_e is computed for each sandstone by using CPA for spherical pores. The grain bulk and shear moduli K_g and μ_g used in CPA are obtained using the linear empirical fits for compressional and shear velocities (in km/s) of shaley sandstones (Han et al., 1986)

$$V_{Pg} = 5.59 - 2.18\, F_c \tag{5.21}$$

and

$$V_{Sg} = 3.52 - 1.89\, F_c\,, \tag{5.22}$$

where F_c is the clay content. Figure 5.3(a) shows that for all 66 sandstones, the modulus K_{50} is much lower than the K_e with the difference ranging 5 to 15 GPa. We explain this

difference by the presence of the intermediate porosity that is still open at the stress of 50 MPa.

The mismatch between the experimentally measured elastic moduli at 50 MPa and estimated effective elastic moduli of Swiss cheese rock with stiff porosity only cannot be explained with presence of stiff pores with aspect ratios smaller than unity. Figure 5.3(b) shows variations of the normalised bulk elastic moduli with porosity for all the sandstones. CPA predicted variations of the effective bulk moduli for the inclusions with aspect ratios of 0.01-1.0 are shown by lines. The difference between elastic moduli of rocks with the same porosity and aspect ratios of 1.0 and 0.5 is very small. The measured elastic moduli exhibit the same trend with the porosity increase as CPA predictions for aspect ratios of 0.2 and smaller. We consider pores with such aspect ratio as intermediate porosity. The normalised elastic moduli verses porosity trends, which correspond to CPA predictions for the pores with aspect ratios smaller than 0.2, can be considered as an independent verification of the existence of the intermediate porosity.

Once existence of intermediate pores is established, we need to check whether all the stiff porosity can be considered as intermediate with a single effective aspect ratio less than 0.2 (without any equant porosity). If there is no equant porosity, then in equation 5.19 C_{e}=1/K_{g} and $\phi_{m0} = \phi_{s0} \simeq \phi$. Then linearisation of equation 5.19 for small pressures gives

$$C_{\mathrm{ds}} = C_{\mathrm{g}}\left[1+\phi_{\mathrm{s0}}\theta_{\mathrm{m}} - \phi_{\mathrm{s0}}\theta_{\mathrm{m}}^{2}C_{\mathrm{g}}P\right]. \tag{5.23}$$

Thus the stress dependency of bulk modulus can be written as

$$K_{\mathrm{ds}} = K_{\mathrm{g}}\left[1-\phi_{\mathrm{s0}}\theta_{\mathrm{m}} + \phi_{\mathrm{s0}}\theta_{\mathrm{m}}^{2}C_{\mathrm{g}}P\right]. \tag{5.24}$$

Analysis of ultrasonic data for different classes of rocks shows that the stress sensitivity coefficients are similar for the bulk and shear moduli (Eberhart-Phillips et al., 1989; Takei, 2002; Shapiro, 2003). Thus, the linearised velocity-pressure dependency can be approximately written as

$$V_{\mathrm{P}} = V_{\mathrm{g}}\left[1-\phi_{\mathrm{s0}}\theta_{\mathrm{m}}/2 + \phi_{\mathrm{s0}}\theta_{\mathrm{m}}^{2}C_{\mathrm{g}}P/2\right] = V_{\mathrm{g}}\left[1-\phi_{\mathrm{s0}}\theta_{\mathrm{m}}/2\right] + V_{\mathrm{g}}\phi_{\mathrm{s0}}\theta_{\mathrm{m}}^{2}C_{\mathrm{g}}P/2. \tag{5.25}$$

Comparison of equation 5.25 with equation 5.8 without the exponential term gives the following approximate expression for coefficient *K* in equation 5.8

$$K = \frac{1}{2}\phi_{s0}\theta_m^2 V_g / K_g . \tag{5.26}$$

For a typical sandstone, taking ϕ=0.2, V_g = 5 km/s, $\theta_m = 3$ (assuming an aspect ratio of 0.2, Takei, 2002) and K_g =40 GPa = 400 kbar gives K of about 0.01. This value is about 20-40 times smaller than observed in ultrasonic experiments (e.g., Eberhardt-Phillips et al., 1989). The only way to explain this strong pressure dependency of velocities is to assume that some portion of the overall porosity has aspect ratios much smaller than 0.2.

5.3.3. Squirt flow in the presence of intermediate porosity

If the rock contains compliant, equant and intermediate porosity, two types of the squirt flow will occur: (I) between compliant and stiff pores (equant plus intermediate) and (II) between intermediate and equant pores. The frequency dependence of the modified frame bulk modulus due to the flow between compliant

and stiff pores is governed by equation 5.3 but with K_h replaced by the pressure dependent modulus $K_{ds}(P)$=1/$C_{ds}(P)$

$$\frac{1}{K_{mf}(P,\omega)} = \frac{1}{K_{ds}(P)} + \frac{1}{\frac{1}{\frac{1}{K_d(P)} - \frac{1}{K_{ds}(P)}} + \frac{3i\omega\eta}{8\,\phi_c(P)\alpha_c^2}}. \tag{5.27}$$

The corresponding equation for the flow between intermediate and equant pores is

$$\frac{1}{K_{mf}(P,\omega)} = \frac{1}{K_e} + \frac{1}{\frac{1}{\frac{1}{K_{ds}(P)} - \frac{1}{K_e}} + \frac{3i\omega\eta}{8\,\phi_m(P)\alpha_m^2}}, \tag{5.28}$$

Equations 5.27 and 5.28 can be combined to give a unified equation for the bulk modulus of the modified frame

$$\frac{1}{K_{mf}(P,\omega)} = \frac{1}{K_e} + \frac{1}{\frac{1}{\frac{1}{K_{ds}(P)} - \frac{1}{K_e}} + \frac{3i\omega\eta}{8\,\phi_m(P)\alpha_m^2}} + \frac{1}{\frac{1}{\frac{1}{K_d(P)} - \frac{1}{K_{ds}}} + \frac{3i\omega\eta}{8\,\phi_c(P)\alpha_c^2}}, \tag{5.29}$$

Modulus K_{mf} can be used to obtain the bulk modulus of the fully saturated rock using Gassmann's or Biot's equations. The shear modulus is given by equation 5.4.

5.4. Workflow

In this section, we outline the workflow that we apply to the ultrasonic velocities experimentally measured on dry sandstones to derive parameters of the pore microstructure and then to predict frequency dependent elastic properties of the saturated rock using these parameters. The workflow assumes that dry elastic properties (moduli and velocities) are independent of frequency (non-dispersive).

1) Dry bulk and shear moduli K_d and μ_d at each confining pressure P_i are obtained from the ultrasonic measurements of the compressional and shear velocities V_P and V_S.

2) Parameters C_{ds0}, ϕ_{c0}, θ_c, and θ_s are obtained by the least-squares fitting of the dry compressibility $C_d(P_i)=1/K_d(P_i)$ with equation 5.12.

3) Characteristic aspect ratio α_c of compliant pores is obtained using equation 5.13.

4) C_e is computed with CPA for spherical pores using K_g and μ_g, which can be obtained from the mineralogical composition of the rock, for instance, by Voigt-Reuss-Hill average (if elastic properties of composite materials are known) or by extrapolating of velocity-porosity regression to a zero-porosity limit. In this study we did not know exact mineral composition of the rock and thus use the latter approach.

5) Values of $C_{ds}(P_i)$ for each pressure P_i are obtained by subtracting the exponential term $\theta_c C_{ds0}\phi_{c0}\exp(-\theta_c C_{ds0}P_i)$ from the dry compressibilities $C_d(P_i)$.

6) Constants ϕ_{m0} and θ_m are obtained by least-squares fitting of the values of $C_{ds}(P_i)$ with equation 5.19. Note that since the data only exist for pressures P_i much smaller than $(\theta_m C_e)^{-1}$, this fit is essentially linear.

7) The characteristic aspect ratio α_m of the intermediate pores is obtained using the expression for a dilute concentration of ellipsoidal cavities (cf. equation 5.13)

$$\theta_m = \frac{K_e(3K_e+4\mu_e)}{\pi\alpha_m\mu_e(3K_e+\mu_e)} \tag{5.30}$$

8) The compliant porosity $\phi_c(P)$ as given by equation 5.11 and the corresponding aspect ratio, α_c, are substituted into equations 5.27 and 5.4 to calculate the bulk and shear modified frame moduli $K_{mf}(P,\omega)$ and $\mu_{mf}(P,\omega)$ to account for the

dynamic stiffness caused by the presence of the fluid in the grain contact area and pressure relaxation between compliant and stiff pores.

9) Likewise, intermediate porosity $\phi_m(P)$ given by equation 5.17 and the corresponding aspect ratio, α_m can be substituted into equations 5.28 and 5.4 to account for pressure relaxation between intermediate and equant pores.

10) The two models for the bulk modulus are combined using equation 5.25.

11) The frequency- and pressure-dependent bulk modulus $K_s(P,\omega)$ of the fully saturated rock is computed with the Gassmann equation 5.5, and together with the shear modulus $\mu_s(P,\omega)=\mu_{mf}(P,\omega)$ is used to compute complex and frequency- and pressure-dependent compressional and shear velocities $V_P(P,\omega)=\left\{\left[K_s+(4/3)\mu_s\right]/\rho\right\}^{1/2}$ and $V_S(P,\omega)=\left\{\mu_s/\rho\right\}^{1/2}$, where ρ is density of the saturated rock. The real part of these complex velocities defines the phase velocity of the corresponding waves, while the imaginary part defines attenuation.

5.5. Data examples

5.5.1. Pressure dependency of the ultrasonic velocities

The compressional and shear velocities predicted with the above workflow (from dry measurements) can be compared to laboratory measurements on wet samples. Most common and robust are time-of-flight measurements using a narrow-band ultrasonic pulse with a central frequency between 0.25 and 1 MHz. Such measurements effectively yield ultrasonic velocities in a narrow frequency band in a range of pressures between 0-50 MPa.

We illustrate the above workflow with ultrasonic measurements on dry and wet sandstones reported by Han et al. (1986). As the first example, we consider ultrasonic measurement data for a St. Peter sandstone sample, a typical reservoir rock with a porosity of about 20%. Figure 5.4 shows the decrease of the dry compressibility (calculated from compressional and shear ultrasonic velocities and density) with increasing pressure in the range 5-50 MPa (open circles). This decrease is well described by a combination of exponential and linear terms, equation 5.12, with the

exponential term vanishing at about 20–25 MPa. The fitting using equation 5.12 gives $\theta_c = 4.2 \cdot 10^3$ which corresponds to the aspect ratio $\alpha_c = 0.15 \cdot 10^{-3}$. The fitting curve is shown in Figure 5.4 by the solid line. Note that the characteristic frequency f_c of the squirt dispersion as described by equations 5.3 and 5.4 is approximately given by

$$f_c \sim \frac{4\mu_h(3K_h+\mu_h)}{3(3K_h+4\mu_h)\eta}\alpha_c^3 \tag{5.31}$$

(Gurevich et al., 2010, equations 5.41 -5.42). For the St. Peter sandstone sample, this gives $f_c \sim 50$ Hz. This frequency is in the seismic exploration range and well below the frequency of ultrasonic experiments. Thus, the dispersion at ultrasonic frequencies can only be explained by the squirt from the pores with a larger aspect ratio, that is, with intermediate porosity. Indeed, the aspect ratio of the intermediate porosity is $\alpha_m = 3.9 \cdot 10^{-3}$, which gives $f_c \sim 0.8 \cdot 10^6$ Hz, right within the typical range of ultrasonic measurements.

As can be seen in Figure 5.2, at the maximum stress of 50 MPa, the bulk modulus reaches 18 GPa, which is below the CPA estimate of K_e=23 GPa. We explain this difference by the presence of the intermediate porosity. The dashed line in Figure 5.4(b) shows the projected pressure dependency of the dry compressibility in a broader pressure range, as predicted by the model with the intermediate porosity, equation 5.19. The pressure dependency of the corresponding compliant porosity ϕ_c (solid line) and intermediate porosity ϕ_m (dashed line) are shown in Figure 5.5(a,b). Note the linear behaviour of ϕ_m at pressures below 50 MPa.

The stress dependencies of the bulk and shear moduli of both dry and wet St. Peter sandstone are shown in Figures 5.6a,b. In Figure 5.6a circles and squares show measured values of the bulk modulus of the dry and saturated rock, respectively. Dotted and solid lines show predictions of the Gassmann and Biot equations, respectively. The dash-dotted line shows the high frequency limit as predicted using Mavko-Jizba (1991) equations. The dashed line is the prediction of the model of squirt between intermediate and equant pores, equations 5.28 and 5.6. The prediction of the squirt flow dispersion model with the intermediate porosity is in an excellent agreement with the data. A similar observation can be made for the shear modulus (Figure 5.6b). It should be emphasized that the prediction is obtained from parameters extracted from dry measurements without any fitting to the measurements on saturated samples.

In Figures 5.7a,b the predicted saturated bulk modulus is plotted against the measurements for a number of sandstones. Crosses and open circles denote low frequency (Gassmann) and high-frequency (Mavko-Jizba) limits, respectively, and solid circles are predictions of the newly developed squirt model. Figure 5.7a compares the results for all 66 sandstone samples from Han et al. (1986) and for the whole range of pressures 5–50 GPa. In most cases, Gassmann saturation without squirt underestimates the experimental data, while the Mavko-Jizba prediction overestimates the measurements. The saturated bulk moduli obtained with our workflow shows a somewhat better agreement with the measured moduli than either of the limits, but with a rather large scatter. The corresponding plot from the same data set but for clean sandstones only (nine samples) is shown in Figure 5.7b. The squirt model shows a very good agreement with the experiment for most, though not all, of the samples.

5.5.2. Prediction of dispersion and attenuation

Once the model parameters are extracted from dry rock measurements, the squirt model can be used to compute the elastic moduli, wave velocities and attenuation in a range of frequencies. Figures 5.8(a,b,c,d) show predictions of the P- and S-wave velocities and attenuations, a reciprocal of a quality factor, Q, as functions of both frequency and effective pressure for the St Peter sandstone. At seismic frequencies the velocities slowly increase with an increase of frequency until about 1 MHz (the value slightly varies with effective pressure). At this frequency, the squirt characteristic frequency for this water saturated sample, a steep increase of the two velocities takes place. At frequencies higher than the characteristic frequency, velocities increase much more gradually.

At frequencies lower than the characteristic frequency, we expect a strong dependency of the velocity on pressure. At higher frequencies, the variation range of the velocities is much smaller. This observation can be easily understood if we recall that the effective pressure deforms the pore space and closes the thin cracks. At low stresses these thin cracks substantially decrease the bulk moduli of the sandstone at low frequencies, at which the pressure induced by the passing wave can equilibrate. However, at ultrasonic frequencies and at the same stresses, the pore pressure has no time to equilibrate, making it much stiffer, while at higher stresses where the thin pores are partially closed, the difference in rock stiffness between low and high frequencies is

smaller. In the ultimate case when all the thin pores are closed, the squirt flow would not cause any dispersion in the rock stiffness. The fact that generally measurements at ultrasonic frequencies in saturated sandstones deviate from the Gassmann predictions even at maximal effective stresses of 50–60 MPa indicates that thin pores still exist at those stresses.

Attenuation is also strongly frequency dependent. Figure 5.8(b,d) show the predicted compressional dimensionless P- and S-wave attenuation factors ($1/Q$) for a range of frequencies. We observe that the attenuation increases with frequency until it reaches the maximum value at the squirt characteristic frequency. After that, the attenuation starts to decrease until 10^7 Hz, after the rate of the decrease changes (as discussed in Gurevich et al., 2010). The attenuation is slightly dependent on pressure, showing an inverse relation: the minimum pressure (blue) corresponds to a maximum attenuation. This is true for all frequencies; however, the variation with pressure is stronger at frequencies lower than the characteristic frequency.

As discussed earlier, the velocity dispersion at an ultrasonic frequency is consistent with the model of squirt flow between intermediate and equant pores. The squirt flow between compliant and stiff pores has a much lower characteristic frequency (50 Hz for St. Peter's sandstone) and thus may be important in the seismic frequency band. Figure 5.9(a,b) show histograms of characteristic frequencies of the squirt between compliant and stiff pores (grey) and between intermediate and equant pores (black). Figure 5.9(a) is for all 66 samples and Figure 5.9(b) is for a subset consisting of clean sandstones only. We see that for most samples the characteristic frequency of the squirt between compliant and stiff pores is in the seismic frequency band.

5.6. Discussion

The model presented here is based on the concept that the pore space in the rock can be divided into three distinct portions: compliant pores that close at effective pressures of up to 50 MPa, intermediate pores that close at much higher pressures (say, 200–2000 MPa) and equant pores with the aspect ratio of the order 1, which do not deform noticeably for pressures up to 2000 MPa. We are not suggesting that the rock contains ellipsoidal pores with three distinct aspect ratios; rather, we suggest that this is the maximum information about the aspect ratio distribution that can be obtained from ultrasonic measurements on dry samples in the confining pressure range of up to 50

MPa. This is not the only model consistent with these measurements. Other models (such as those based on the power-law pressure dependency) are possible but are beyond the scope of our study.

It should also be noted that when we talk about a characteristic aspect ratio, we mean a relatively narrow, unimodal but continuous distribution. An exponential pressure dependency of elastic moduli is consistent with the existence of compliant pores of a single aspect ratio, and, within measurement errors, with a unimodal distribution of aspect ratios. Since the pressure range of up to 50 MPa is barely sufficient to obtain one exponent, it is not possible to determine the width of this distribution. Thus we use the model with one aspect ratio because it is the simplest model that fits the data and not because it gives a realistic description of the pore space. This applies even more obviously to the intermediate porosity, about which we have even less information. Again we may have a spectrum of aspect ratios between 10^{-3}–$2 \cdot 10^{-1}$ but we describe it by a single aspect ratio because we lack information to describe it in any more detail. Measurements over a much broader pressure range are necessary to characterise the pore space properties in more detail.

In discussing the deformation of the intermediate porosity, it is important to stress that our projected pressure dependencies in the range of up to 500 and even 2000 MPa are purely conceptual. One implicit assumption is that the solid grain material at all these pressures remains linearly elastic. This may not be the case, and indeed grains may even crush at these pressures (e.g., Zhang et al., 1990; Wong et al., 1997; Fortin et al., 2007). However this will not affect our predictions, because the real behaviour at these high pressures is not explicitly used. Instead we only use geometrical parameters of the pore space inferred from such hypothetical behaviour, which is, in turn, inferred from the pressure dependency at pressures below 50 MPa, where the grains are linearly elastic.

We have analysed the prediction of our squirt model for a large number of sandstones. To our knowledge, this has not been done before for any squirt model. Our results show that the model gives a reasonable agreement with the measurements for clean sandstones, but much less convincing agreement for shaley sandstones. This is understandable, since presence of clay may cause non-mechanical interactions between solid and fluid, which are not adequately described by any poroelasticity models. In addition, clays have a complex pore structure which may not be even roughly described

by our simple models. Further studies are necessary to analyse whether the model works at least at modest clay content, and for other rocks.

Our analysis is based solely on measurements of pressure dependency of ultrasonic velocities of dry and wet sandstones. It is highly desirable to compare our predictions with experiments in a much broader frequency range, such as forced-oscillation quasi-static measurements (e.g., Batzle et al., 2006; Adelinet et al., 2010; Mikhaltsevitch et al., 2011). These novel measurements have a potential to substantially improve our understanding of dispersion and attenuation. However, these measurements are still in their infancy and require further analysis and calibration. We plan to analyse these measurements and compare the results with our predictions in a future study.

Apart from stress dependency of elastic properties of rock, other sources of data can give information on the rock pore system. Thin section data in 2D give information about the pore aspect ratio distribution(s). 3D microtomographic images can be used to obtain comprehensive information about intermediate and stiff porosity; however, compliant pores cannot yet be resolved with current CT-scanners (e.g., Shulakova et al., 2011). Capillary pressure data can also be used to get information about pore throat distributions (uni- or bi-modal) and can further help constraining model assumptions. The proposed workflow should be further tested on a dataset for which key model parameters such as grain elastic properties and pore space heterogeneity are measurable from core.

5.7. Conclusions

Modelling of dispersion and attenuation of elastic waves in fluid-saturated rocks due to the squirt flow requires the knowledge of a number of geometrical parameters of the pore space, in particular, the characteristic aspect ratio of the pores. These parameters are usually inferred by fitting the measurements on saturated rocks to the model predictions.

In this study we have attempted to avoid such fitting. To this end, we have proposed to recover the geometrical parameters of the pore space from the pressure dependency of elastic moduli on dry samples. Once such parameters are obtained, they are substituted into the squirt model to predict the elastic moduli and compressional and

shear velocities for a fluid-saturated rock. The velocity predictions can be compared with the measurements on saturated rocks.

Our analysis shows that the pressure dependency of elastic rock properties (and their deviation from Gassmann's prediction) at ultrasonic frequencies is controlled by the squirt flow between equant pores (with aspect ratio of order 1) and intermediate pores (with aspect ratios between $0.3 \cdot 10^{-4}$- $0.03 \cdot 10^{-4}$). Such intermediate porosity is only expected to hypothetically close at pressures in the 200–2000 MPa range, and thus cannot be directly obtained from ultrasonic experiments performed at pressures below 50 MPa. However, the presence of the intermediate porosity is inferred from two facts (1) the significant linear trend in the pressure dependency of elastic properties of the dry rock and (2) the significant difference between the bulk modulus of the dry rock computed for spherical pores only and the measured modulus at the maximum pressure available in ultrasonic experiments (50 MPa). Furthermore, the linear trend below 50 MPa and the projected modulus in the high-pressure limit are used to infer the magnitude of the intermediate porosity and its characteristic aspect ratio. Substituting these parameters into the squirt model, we have computed elastic moduli and velocities of the water-saturated rock and compared these predictions against laboratory measurements of these velocities. The agreement is very good for a number of clean sandstones, but much worse for a broad range of shaley sandstones. This is understandable since the presence of micro porous clays makes the rock texture more complicated and the stress dependence of the heterogeneous sand-clay mix is no longer adequately described through the poroelastic model with three porosity types.

Our predictions also show that dispersion and attenuation caused by the squirt flow between compliant and stiff pores may occur in the seismic frequency band. Confirmation of this prediction requires laboratory measurements of elastic properties at these frequencies.

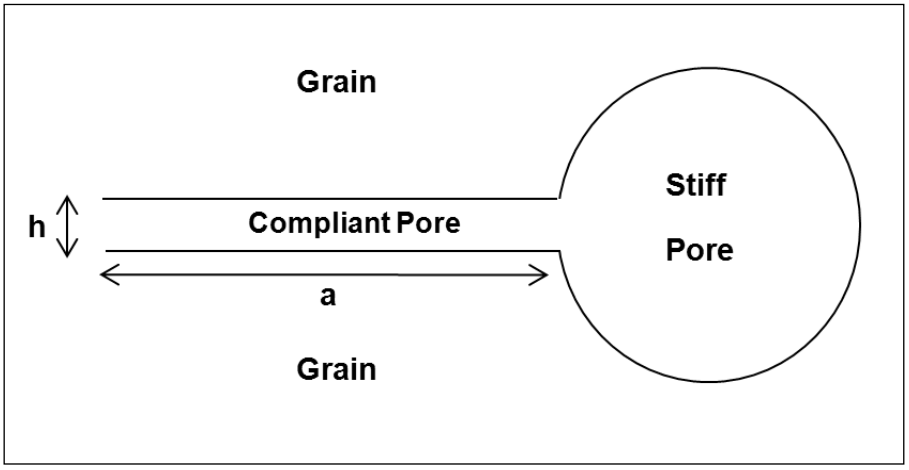

Figure 5.1. Cross-section of the idealised geometry of compliant and stiff pores (Murphy et al., 1986). A disc-shaped compliant pore forms a gap between two grains and its edge opens into a toroidal stiff pore.

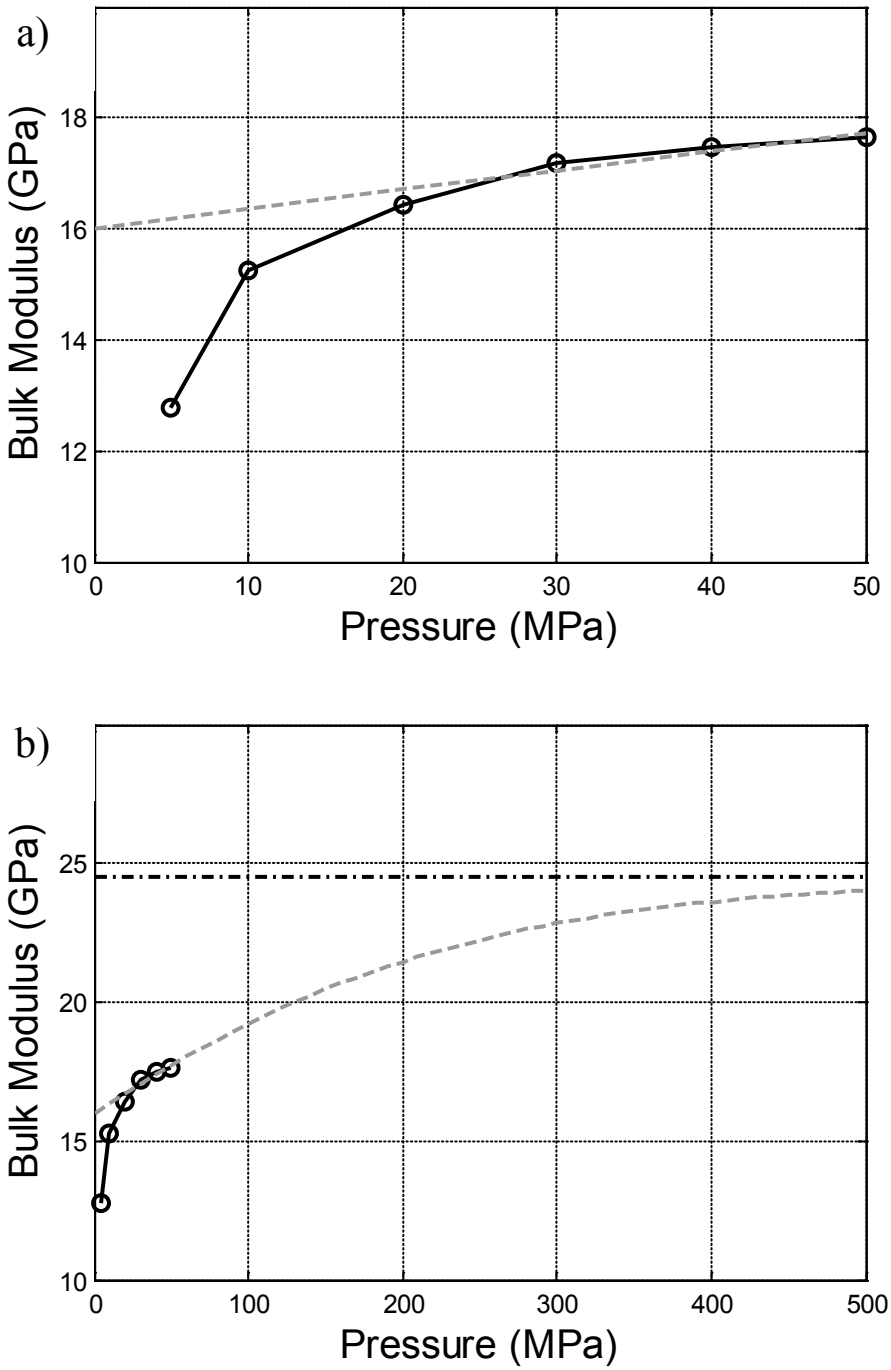

Figure 5.2. Dry bulk modulus stress dependency: (a) up to 50 MPa; (b) up to 500 MPa. Bulk moduli measured on a sample of St. Peter sandstone are shown by open circles and solid lines. Predicted moduli strengthening caused by closure of intermediate porosity exclusively (hypothetical scenario) are shown by dashed grey lines on both plots. A bulk modulus of the same sandstone at a "Swiss-cheese" state is indicated with a dashed-dotted line.

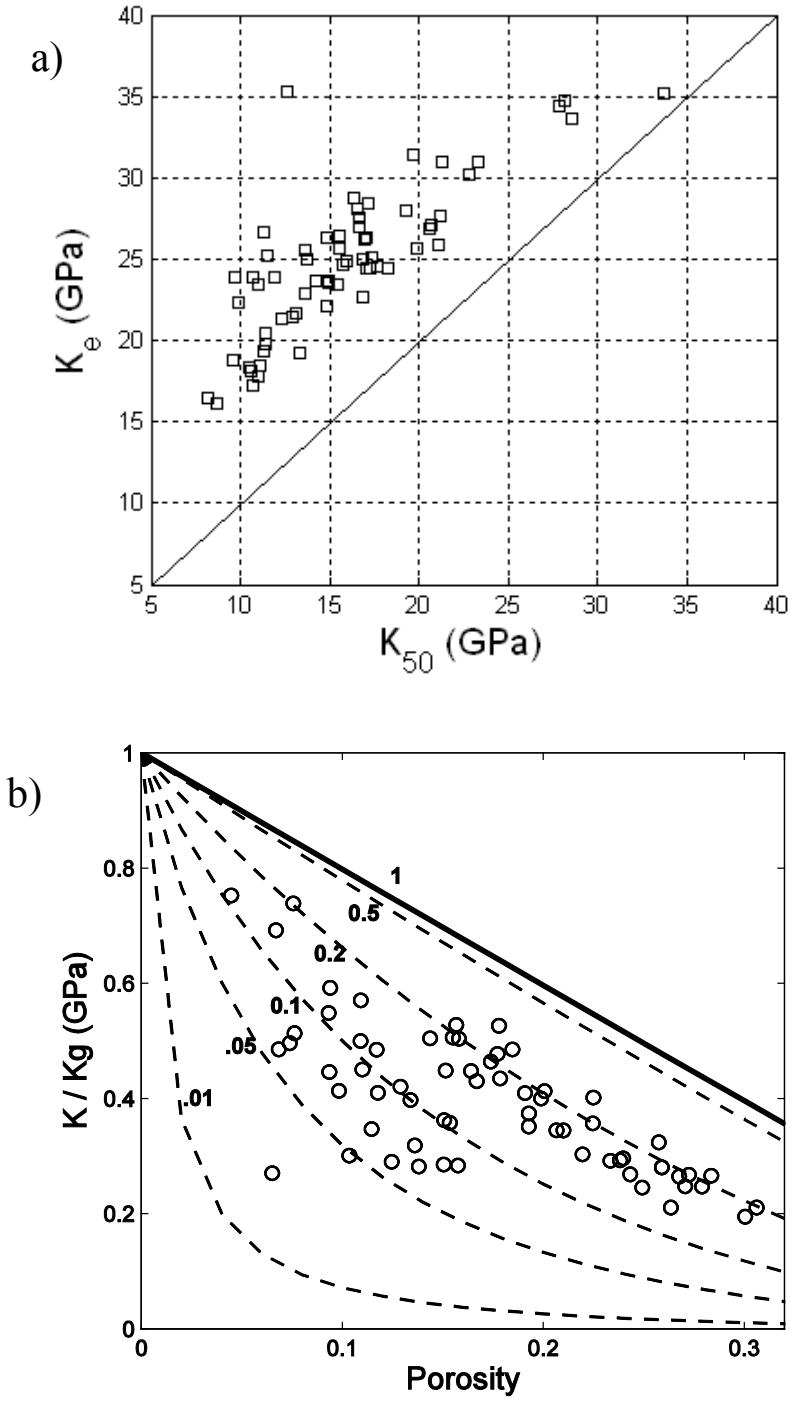

Figure 5.3. Bulk moduli of sandstones calculated from experimentally measured ultrasonic velocities (Han et al., 1986). (a) Dry experimentally measured bulk moduli, K_{50}, at 50 MPa vs. dry bulk moduli, K_e, of the same sandstones at the hypothetic 'Swiss-cheese limit'. (b) K_{50} normalised by grain bulk modulus vs. porosity in comparison with the CPA prediction.

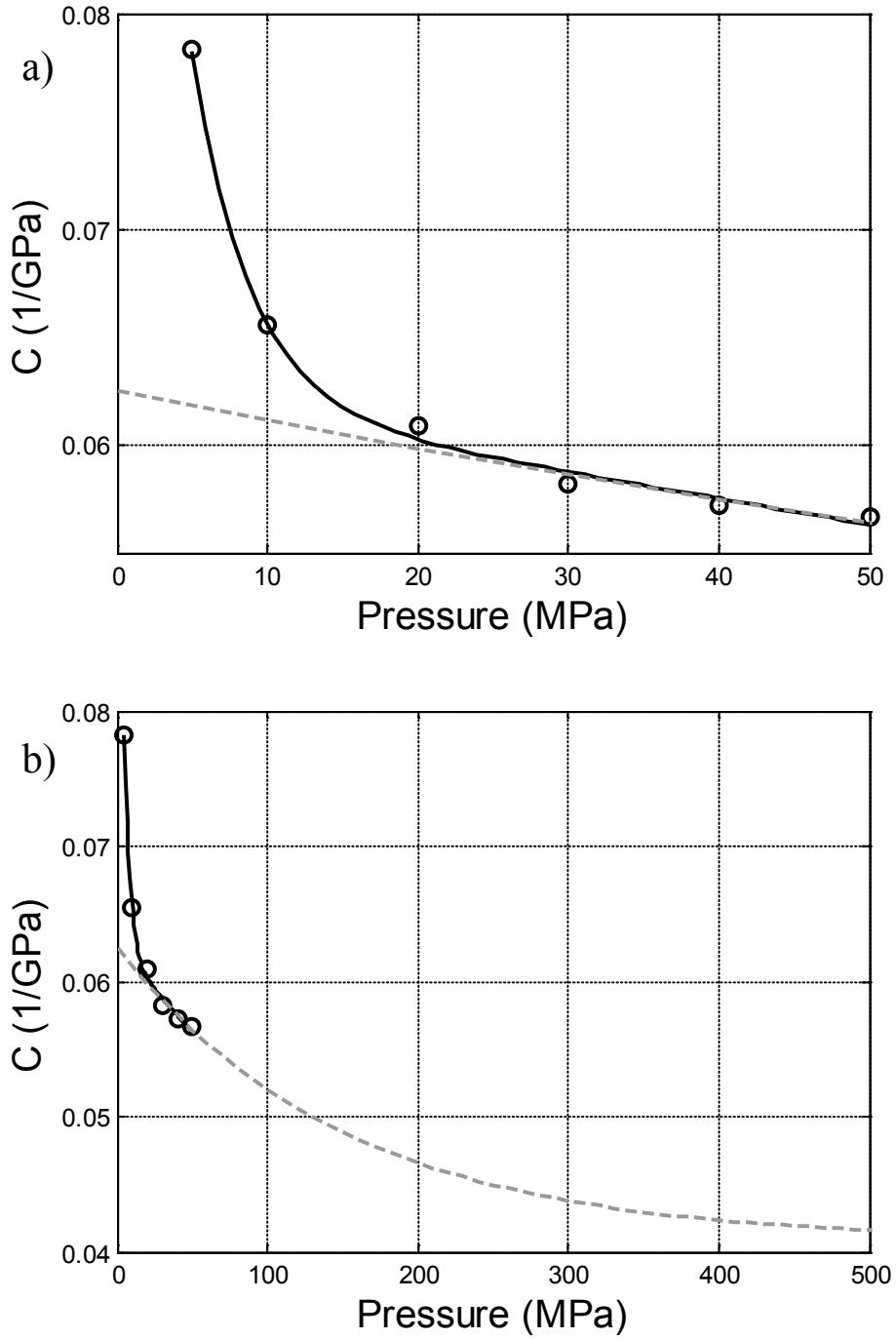

Figure 5.4. Compressibilities of a dry sample of St. Peter sandstone versus pressure: (a) Calculated from ultrasonic velocity measurements up to 50 MPa (open circles), (b) Predicted variations above 50 MPa due to closing of intermediate porosity (dashed line). Solid line shows the best fit of the experimental points with equation 5.12. Note the linear trend of compressibility against pressure after 25 MPa that indicates the collapse of compliant pores at lower stresses.

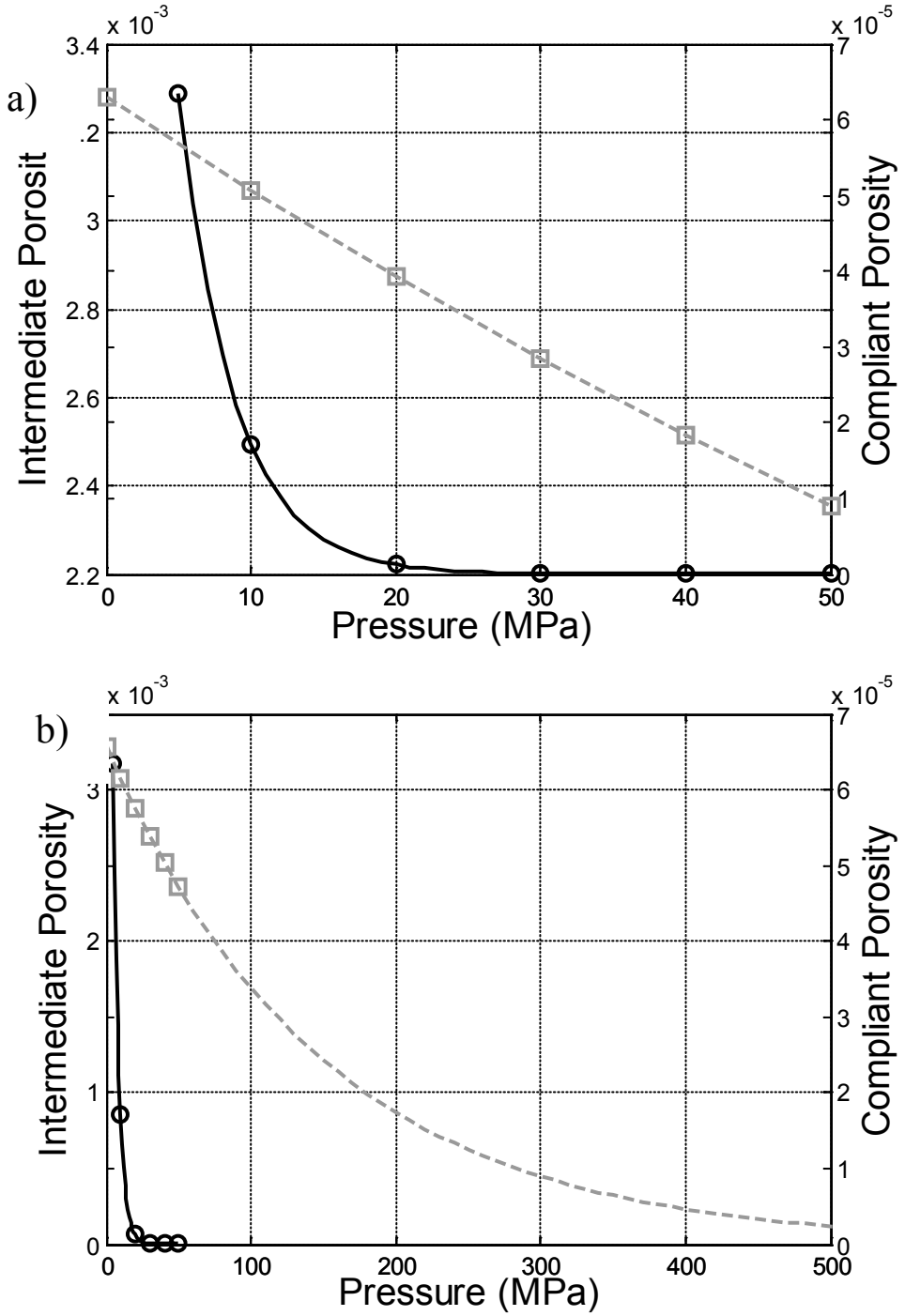

Figure 5.5. Compliant porosity ϕ_c (open circles and solid line) and intermediate porosity ϕ_m (open squares and dotted line) in a sample of St. Peter sandstone as a function of isotropic stress: (a) up to 50 MPa and (b) above 50 MPa. Note that intermediate porosity decreases almost linearly at low stresses. The magnitude of compliant porosity is approximately two orders lower at low stresses and exhibits dramatic decay with the increase of pressure than one of intermediate porosity. Separate axes are used for these entities.

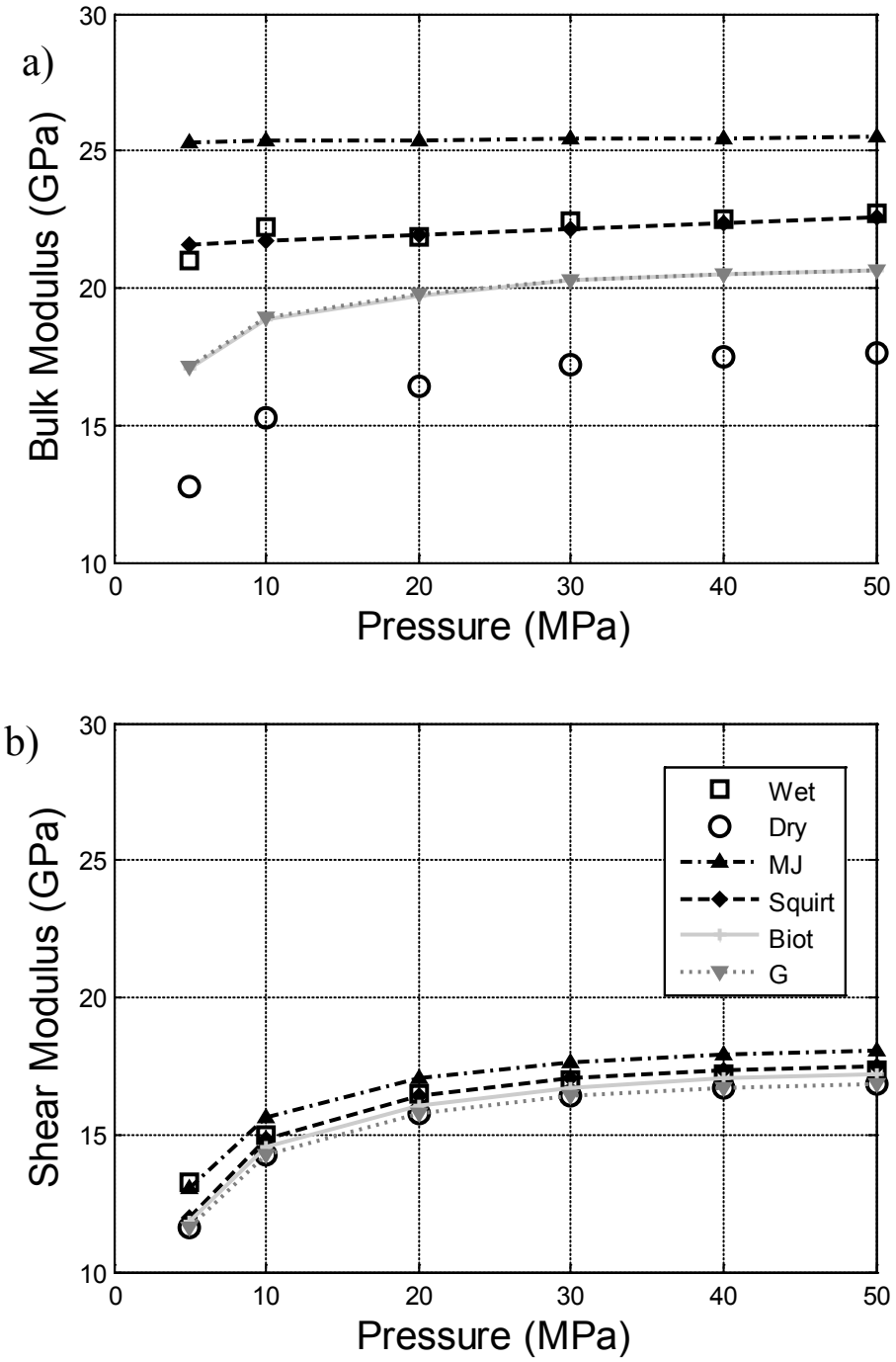

Figure 5.6. Saturated moduli the St. Peter sandstone predicted by a number of theories as a function of pressure: (a) bulk and (b) shear. Gassmann (invert triangles and dotted line) and Bio (cross and solid line) theories underestimate the measured bulk and shear moduli while Mavko and Jizba's model (triangles and dashed-and-dotted line) overestimates them. A good fit for both moduli is obtained with the newly developed squirt model (rhombs and dashed line). Dry and saturated moduli calculated from ultrasonic velocities are shown by open circles and squares, respectively.

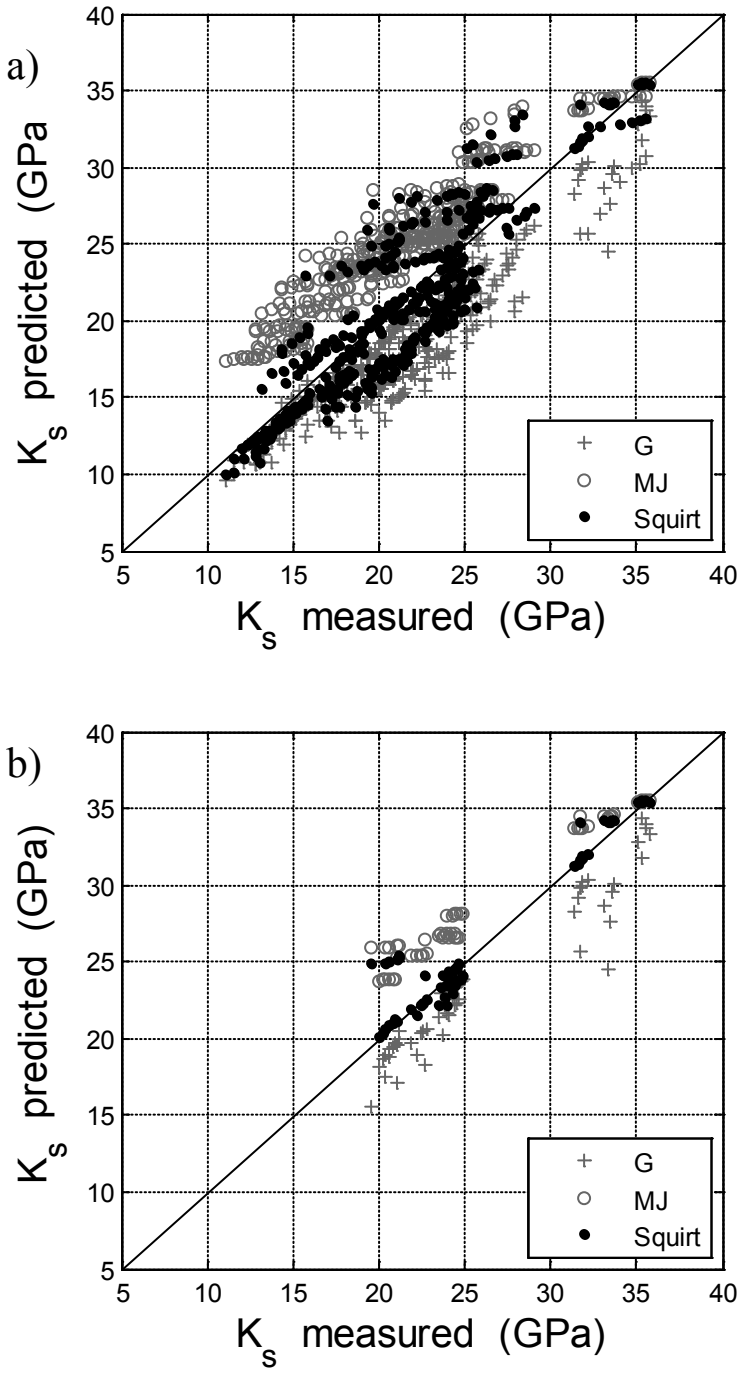

Figure 5.7. Predicted versus measured saturated bulk moduli for the pressure range from 5 to 50 MPa: (a) for all 66 sandstone samples and (b) for clean sandstones only (Han et al., 1986). Gassmann (crosses) predictions underestimate and Mavko and Jizba's model (open circles) overestimates the experimental data. The prediction of the newly developed squirt flow dispersion model (solid circles) with the intermediate porosity is in a better agreement with the data, especially for the clean sandstones.

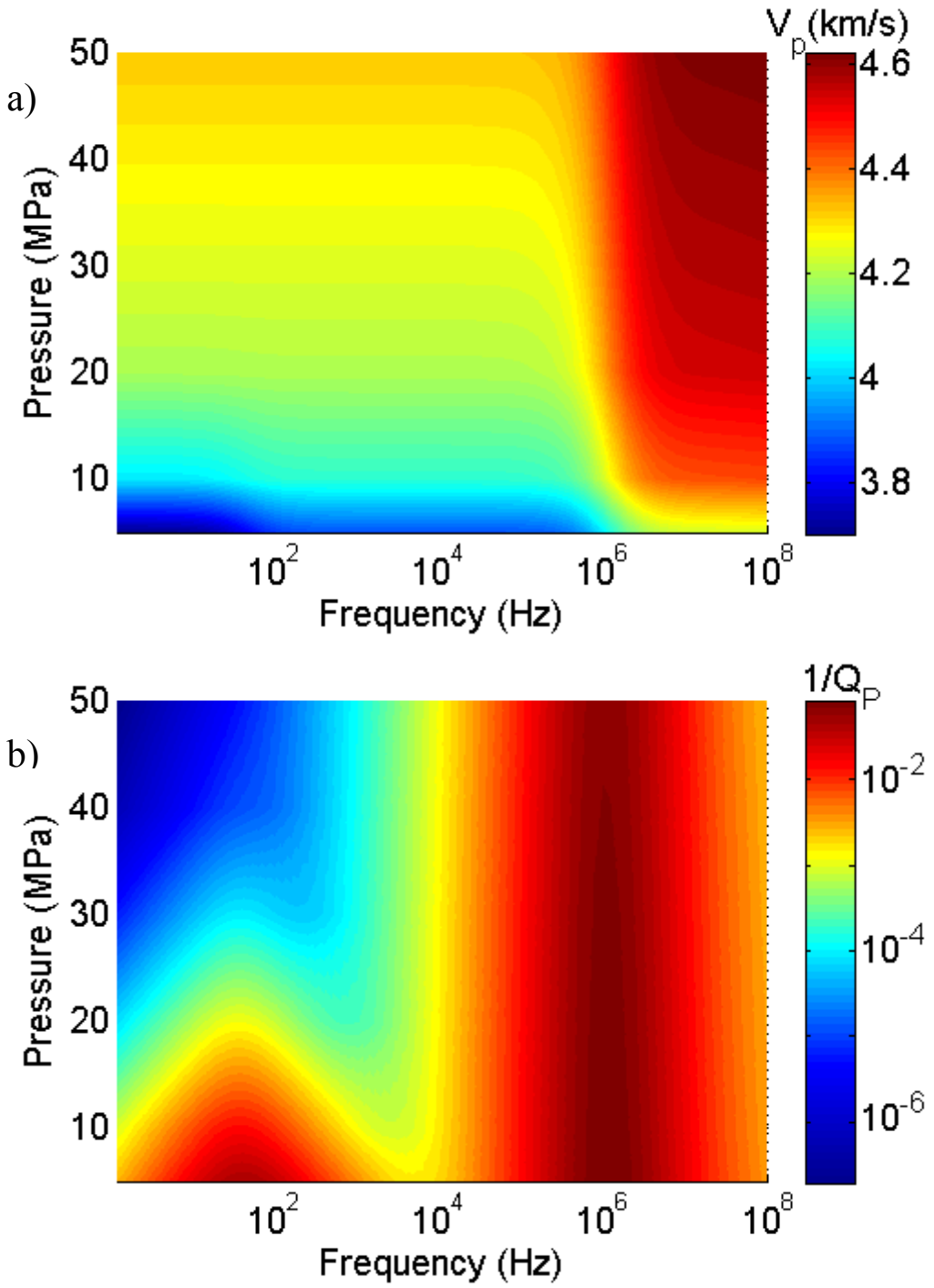

Figure 5.8. Dispersion (a) and attenuation (b) of compressional velocity as a function of pressure and for the wide frequency range from seismic to ultrasonic for St Peter sandstone.

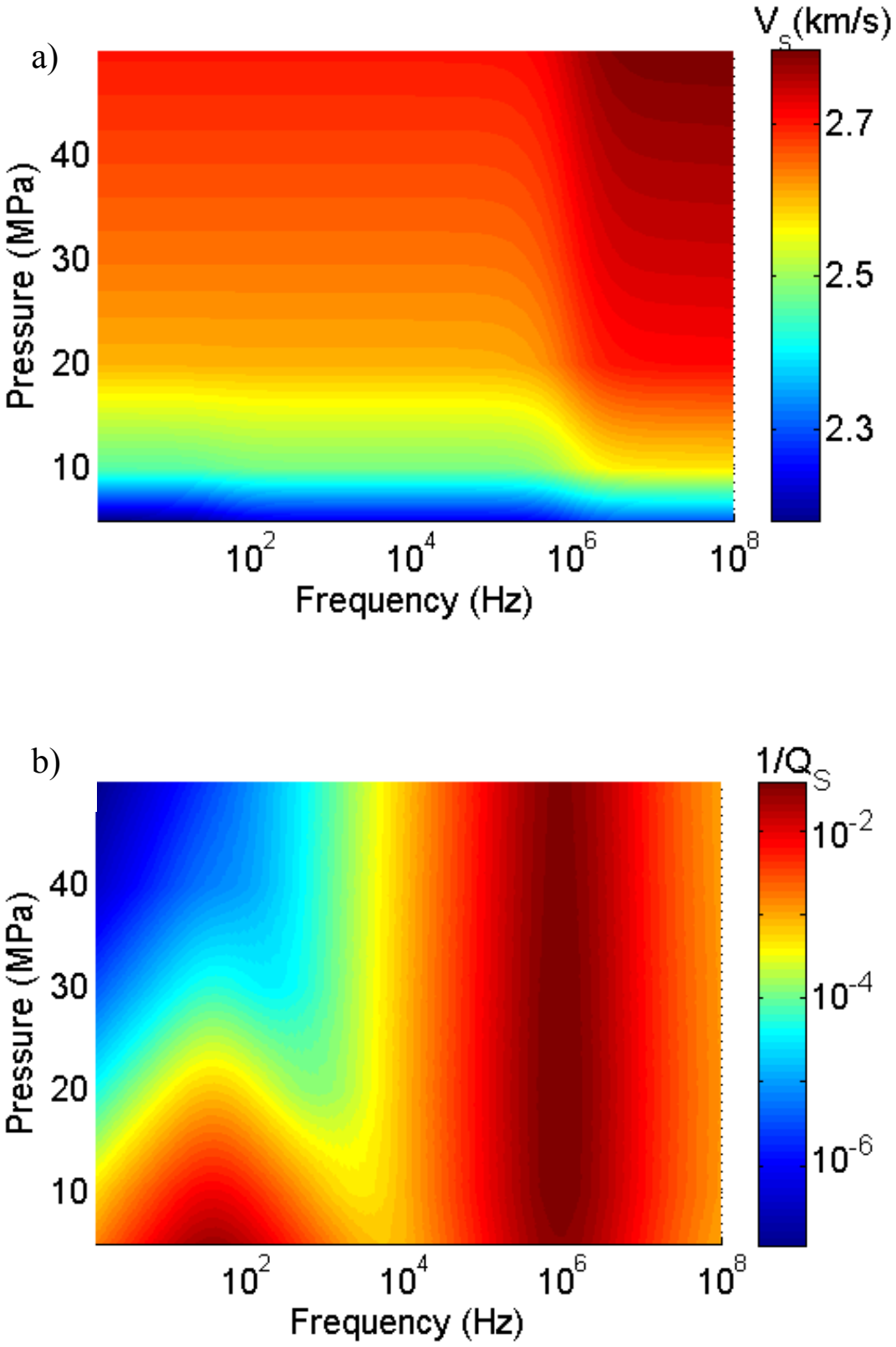

Figure 5.9. Dispersion (a) and attenuation (b) of compressional and shear velocity as a function of pressure and for the wide frequency range from seismic to ultrasonic for St Peter sandstone.

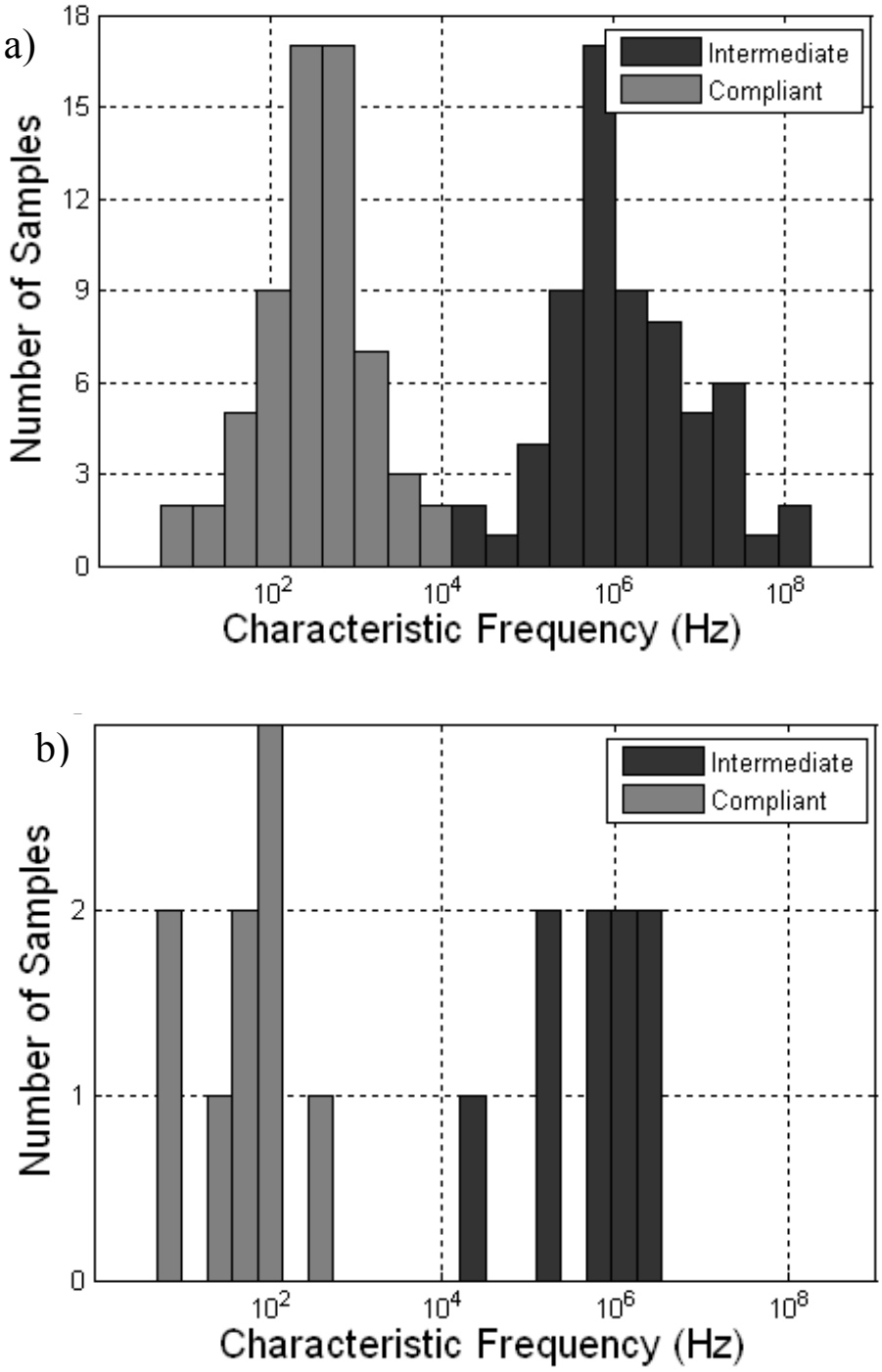

Figure 5.10. Histogram of characteristic frequencies of the squirt: (a) for all 66 samples; (b) subset of clean sandstones (Han et al., 1986). Characteristic frequencies of the squirt between compliant and stiff pores and between intermediate and equant pores are shown by grey and black, respectively.

CHAPTER 6

GPR AND SEISMIC IMAGING OF CARBONATE SEQUENCES IN SHARK BAY, WA – A HOLOCENE RESERVOIR ANALOGUE

6.1. Introduction

All the high resolution data and new technologies that we have seen in the previous chapters need to be connected to solid geological models. Geological models are derived from reconstructions of old depositional systems that are challenging in carbonate systems mainly because the original microstructure can change substantially, in particular porosity and permeability. To minimise the exploration risks when dealing with our carbonate reservoirs the understanding of modern analogues and their facies association are fundamental. We have found a unique modern environment where coquinas, stromatolites and microbial mats near the coast are linked: the Hamelin Pool and L'haridon Bight embayments in the Shark Bay Marine Nature Reserve (Figure 6.1). In particular, Telegraph Station area with its coquina ridge system is the most complete development of this rich environment (Figures 6.2 and 6.3). The study of this modern system of carbonate deposits provides important insights into past Holocene (last 10,000 years) sea levels and climates changes that will help understand the dynamic of depositional system and facies association.

Shark Bay morphology today reflects a NNW-SSE oriented ancient folders system and associated faults. The system confines the bays on the subsiding synclines and the peninsulas over the anticlines (Butcher et al., 1984). A modern regional normal fault system oriented N-S then is superimposed over the ancient system to complete the Holocene scenario. Below the coquina ridges, seismic imaging and well logs confirmed the Pleistocene Tamala Limestone and Tertiary/Cretaceous rocks over an anticline (Playford and Cockbain, 1976) with the axis parallel to the Dirk Hartog Island (Figure 6.1).

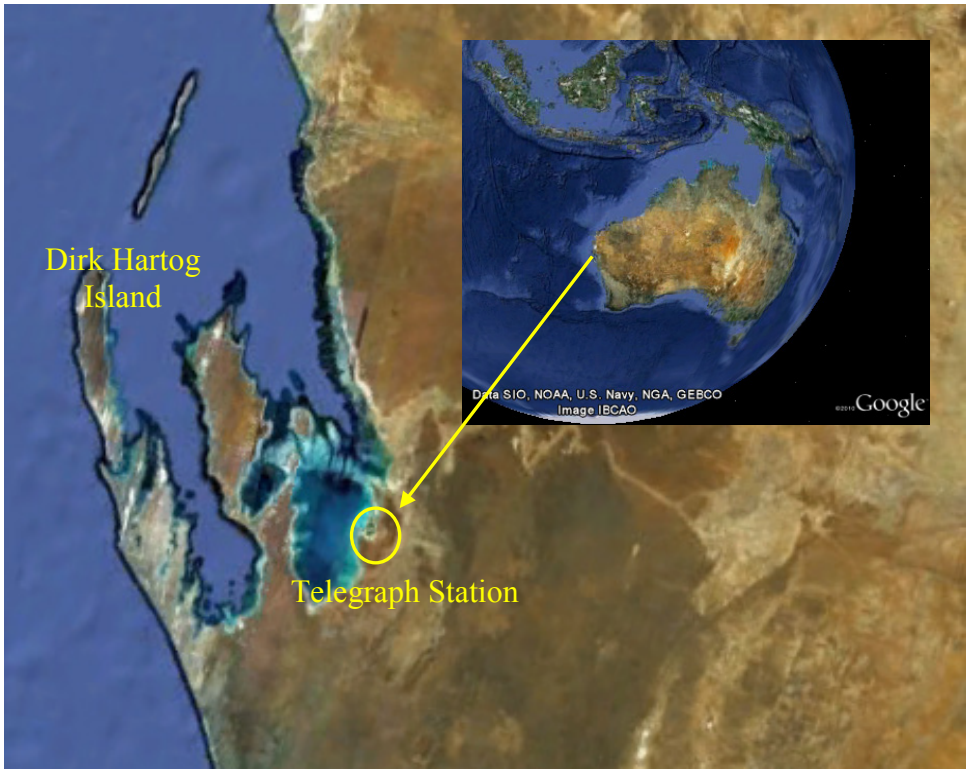

Figure 6.1. Telegraph Station in the Shark Bay Marine Nature Reserve in Western Australia. Hamelin Pool is the embayment close to Telegraph Station with 1400 km^2 of area with maximum water depth of 10 meters.

Figure 6.2. Coquinas ridges still unconsolidated showing the lateral accretion of shell layers parallel to shore line.

Figure 6.3. Telegraph Station coquinas beach ridges consolidated showing the lateral accretion of shell layers parallel to shore line and dipping into sea direction.

Figure 6.4. Telegraph Station coquinas with pronounced bedding and well selected shells.

The coquinas of Telegraph Station can be described as massive shell deposits from accretion of beach ridges. They have been deposited during the Holocene as a 5th order sequence evolution in a highstand sea-level system. The massive deposits are related to prolific mollusc productivity caused by a hypersaline environment that ends with a two meter sea level fall (Logan, 1974). The increased salinity is caused by evaporative concentration as sea water influx was restricted by the Fare Sill sea grass bank (connection with the ocean in Figure 6.1). Coquina ridges reflect the lateral accretion of shell layers produced by waves and winds after the Holocene maximum highstand (+2 m) that happened 6,832 years ago by U/Th dating (Collins et al., 2006). Parallel crests of coquinas occupy more than 2 km width with accretion of 20 crests in tidal flats located in front of the best developed sublittoral platform areas. The normal wave energy plays an important role in transporting and reworking the dead shells, transferring material from the sublittoral platform and producing important washover shell deposits. The long shore transport by currents is also recognised as an important influence in generating the ridge system. Nevertheless probably high energy cyclones are mainly responsible for the construction of the coquina ridges deposits. According to Australian Bureau of Meteorology the cyclone season in Shark Bay area is from November to April, but cyclones are relatively infrequent in the area (one each 5 years).

However, the timing of onset of hypersaline conditions in Shark Bay and initiation of hypersaline facies deposition, the precise nature of coquina ridge genesis and evolution, nature and extent of the preserved Late Holocene storm frequency and sea level record are important questions targeted in this study.

GPR imaging is one of the techniques largely used nowadays to recover high resolution images from reservoir analogues. Most of the published surveys are from siliciclastic deposits and some from carbonates. Examples of 2D GPR imaging come from Neal (2004), recovering a detailed internal structure in beach ridges of mixed sand and gravel at Aldeburg, Suffolk, south-east England. Also Engels et al. (2005), developed a depositional model for sandy gravel beach ridges during the last Holocene highstand in Southern British Columbia, Canada based in 2D GPR lines. More high resolution data comes from 3D GPR surveys that allows better analyses. One 3D example was acquired to detail internal structures of sand dunes, analogue to sandstones reservoirs of Unayzah Formation in Saudi Arabia (Adetunji et al., 2008). Some 3D GPR surveys in carbonates were also acquired in Northern Yucatán, Mexico, with the

purpose of verifying caves and 3D karst features, giving some clues for underground water exploration (Medina et al., 2010). Another 3D high resolution GPR survey was acquired in an oolite grainstone in Turks and Caicos Islands, British West Indie (Guidryet al., 2007). In this case the purpose was to quantify karst features and early fracture networks addressing the preferential fluid flow pathways in ancient carbonates.

We discuss here the acquisition, processing and interpretation of 2D and 3D GPR and a 2D high resolution seismic over Telegraph Station coquinas ridges. We acquired 7.5 km of GPR data to investigate the origin, stratigraphy, internal structure and storm record preserved in the coquinas of the hypersaline zone. These data provided us with a detailed internal architecture of the system. We discuss the correlation between this new high resolution GPR data and field observations, core analysis and sample dating (Figure 6.5) that helps to give us insights about the nature of the ridge system, including past cyclone frequency, climate and sea level changes. The purpose of the seismic experiment is to acquire elastic parameters to calibrate our dataset or to project future surveys.

6.2. Methodology

We designed three independent GPR surveys to cover different scales: Survey S1 is the most regional, covering most of the area (Figure 6.5 in black lines). It is composed of five lines orthogonal to the coquina beach ridges crossed by lines parallel to the deposition trends. Survey S2 (Figure 6.5 in blue lines) was designed to get more details of two main beach ridges, with intervals of 20 meters between the lines. A detailed survey S3 was acquired in a flat surface between two ridges to obtain a maximum spatial resolution, with an interval between lines of 0.2 m (red rectangle in Figure 6.5). The seismic line L1 is a 100 m extension and was acquired with a geophone spacing of 1 m. The shots were also shouted every meter. The seismic line in magenta (Figure 6.5) is coincident with an extra GPR line and it intersects the 3D GPR

The lateral extent of this 3D GPR cube is 10 x 15 m. A total of 7.5 km GPR data was acquired during the survey.

The Data was loaded and processed in ReflexW. The surveys S1 and S2 were interpreted using SeisWorks® 2D Seismic Interpretation Software (Halliburton) and the

survey S3 was interpreted using GeoProbe® Volume Interpretation Software (Halliburton).

6.3. Equipment

For GPR acquisition we used the Mala ProEx system coupled with a high-precision real-time kinematic (RTK) GPS system by Thales for precise localisation. The RTK GPS Rover was mounted on top of the GPR antenna and the system manually dragged as displayed in Figure 6.6a. Measurements were triggered with a measurement wheel at increments of 7 cm. Figure 6.6b shows the RTK base station with a radio transmitter for communication with the RTK-Rover. In order to avoid noise from the radio transmitter, we kept at a distance of approximately 50 m or decreased the power of the radio transmitter. No interference from the Rover's passive radio receiver was experienced while acquiring the data. GPS positions were directly linked to GPR-traces during the acquisition by Mala's GroundVision 2 software at a sampling frequency of 1 Hz. We were not concerned about minor lacks in communication time due to the regional scale of the surveys. For the detailed survey S3, however, we did correct for shifts in position depending on line direction.

GPR antenna frequencies of 250 MHz, 500 MHz (shielded) and 100 MHz (unshielded, separable) were available and have been tested in the field. Before the acquisition we expected the 250 MHz centre frequency antenna to have the best performance in terms of depth-of-penetration and resolving power. After a first field evaluation, however, we decided that the 500 MHz antenna had enough depth of penetration while providing a higher resolution image, which was not too disturbed by clutter and diffractions. Therefore we employed the 500 MHz antenna for subsequent measurements. The 100 MHz separable antennas were used for the common-shot gather for velocity interpretation.

We used a 120 channel EX-6 system for the high resolution seismic acquisition, vertical and horizontal geophones (28 Hz) and a 6 kg Sledge-Hammer and S-wave cage as a source.

6.4. GPR data analysis

We chose line B (Figure 6.4) for testing the antenna performance (Figure 6.7, 250 MHz (lower) verses 500 MHz (upper)). While the 250 MHz antenna provides a better depth of penetration and a simpler image of the major radar facies, it is unable to return information from a depth of less than ~ 1 m due to long air-wave arrival and resolving thin beds. The 500 MHz data, on the other hand, detects more interfaces that can be followed up almost to the surface.

Figure 6.8 shows the energy envelope and its dependency on frequency. It is clear, however, that most of the energy is restricted to portions above the water table level in both sections. The water table level here is the onshore projection of sea level. Both sections don't show a reflection from the water table, probably due to energy absorption from the saline sea water.

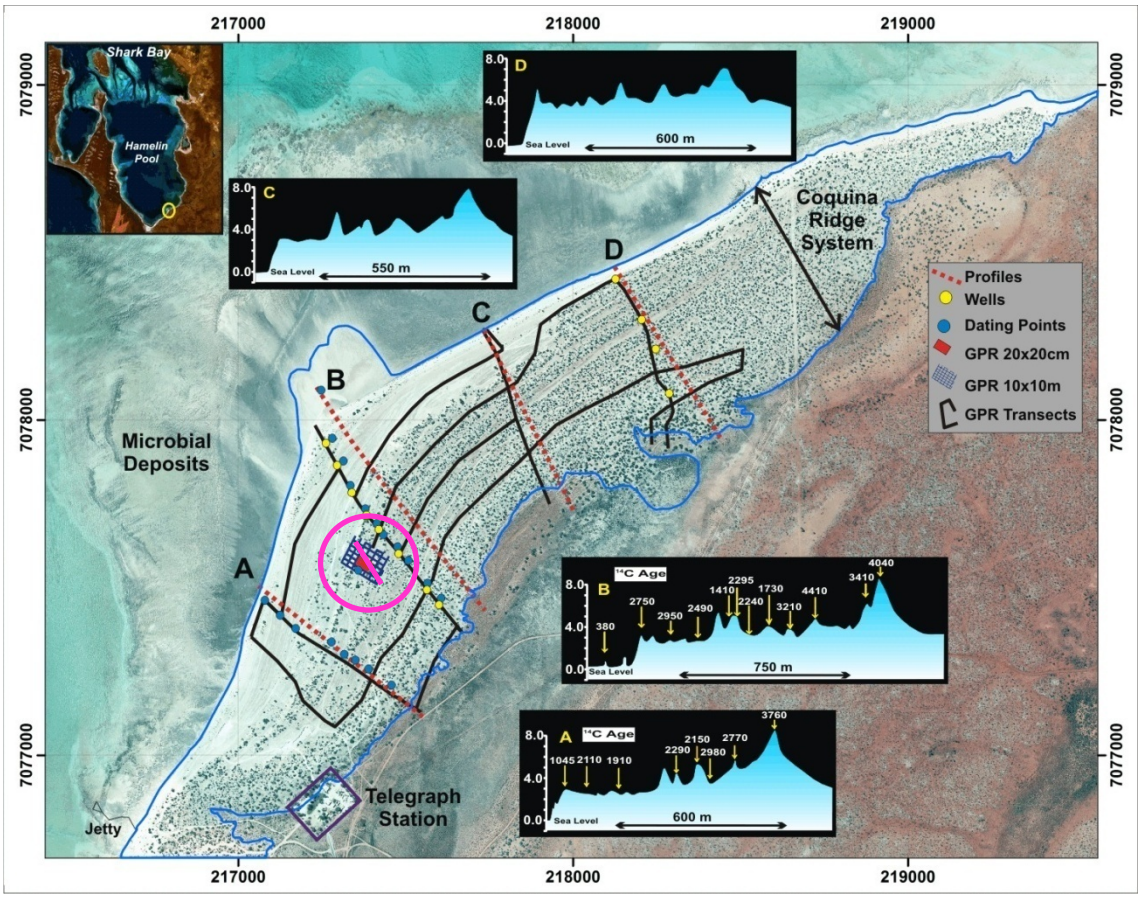

Figure 6.5. GPR surveys in Telegraph station. Surveys S1 (long lines in black), S2 (grid in blue) and S3 (red). The tie wells are in yellow, dating points in blue and 4 topographic profiles with dating ages in red (profiles A and B). The seismic line (magenta) is inside the circle. An extra GPR line was acquired at the same position.

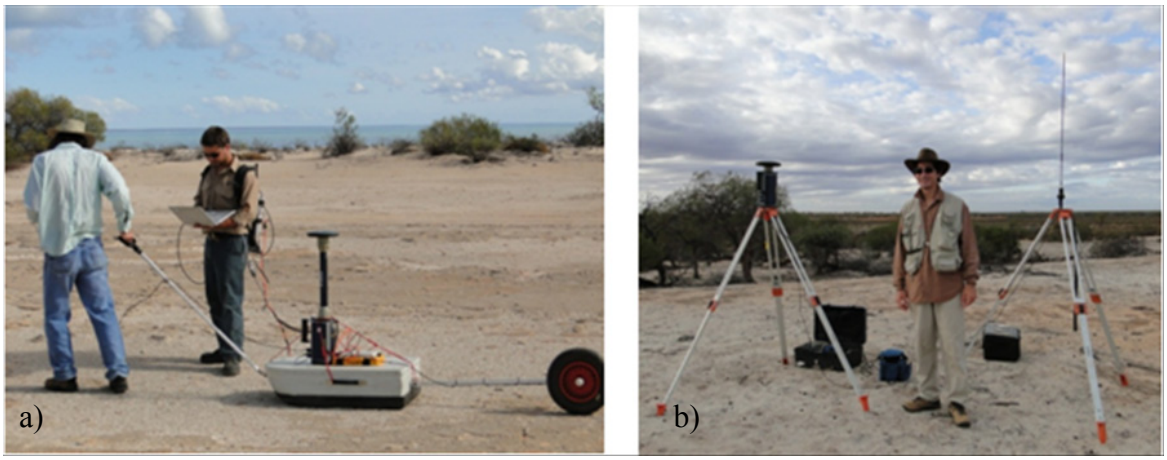

Figure 6.6. (a) ProEx Control Unit and the 250 MHz GPR antenna coupled with the Thales RTK GPS Rover and a custom-built trigger wheel. (b) RTK GPS base unity (on the left) and radio transmitter (on the right).

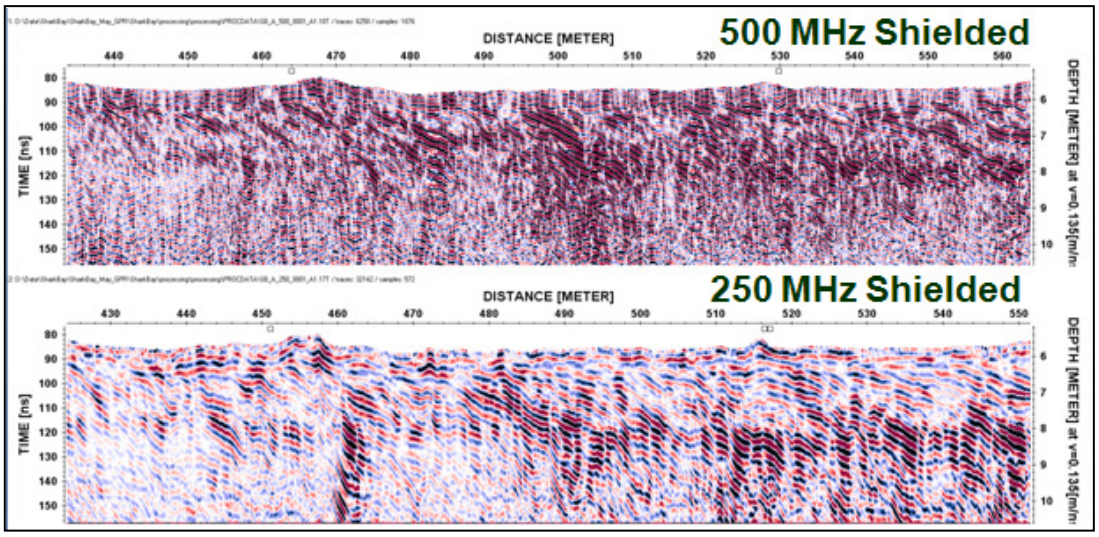

Figure 6.7. GPR line B with 250 MHz antenna (below) and 500 MHz (above) with AGC-gain and trace normalisation applied. Note the higher resolving power of the 500 MHz data while achieving depths of penetration of 4 – 5 m.

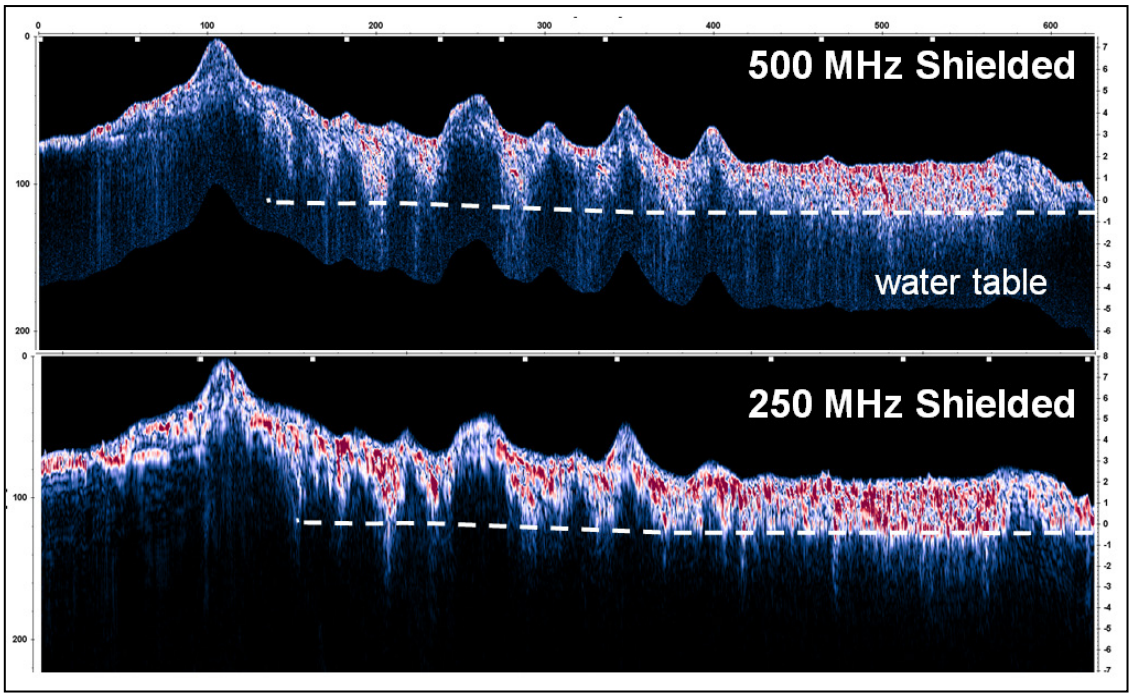

Figure 6.8. Energy envelope of line B with 500 MHz (above) and 250 MHz (below). Note the higher level of energy in the 250 MHz section and the lack of energy retrieval from below the water table.

In order to support field-scale velocity estimates we collected five different coquina samples and analysed them at the dielectric facilities in the petrophysics laboratory at CSIRO with an impedance analyser (40 Hz to 110 MHz) (Josh et al., 2009). Measurements of complex dielectric permittivity were extrapolated to higher frequencies by fitting a curve to the high-frequency end of the measurements (1 – 110 MHz) and analytically calculating values with that curve function. The samples were collected close to the surface and are representatives of the survey area. Figure 6.9 shows the coquina soil samples collected over a main ridge (sample 100), behind the most inward-ridge (sample 101), red soil from a back-barrier wetland rich in iron hydroxides (sample 102), clean coquina (sample 103) and coquina with some dispersed organic material from ephemeral algal mats (sample 104). Water contents vary from 2.0 w% for the clean coquina (sample 103) to 6.4 w% for the coquina behind the ridge (sample 101). The electromagnetic wave propagation velocity v and the material attenuation α have been determined from the complex dielectric permittivity (Daniels, 2004):

$$v = \frac{c}{\sqrt{\varepsilon'_{e,r}}} \tag{6.1}$$

and

$$\alpha = 8.686 \cdot 2d \cdot 2\pi f \cdot \sqrt{\frac{\mu'_0 \mu'_r \varepsilon'_0 \varepsilon'_{e,r}}{2}} \cdot \left(\sqrt{(1 + tan^2\,\delta)} - 1\right); \tag{6.2}$$

$$tan\,\delta = \frac{\varepsilon''_{e,r}}{\varepsilon'_{e,r}}, \tag{6.3}$$

where $\varepsilon'_0, \varepsilon'_{e,r}, \varepsilon''_{e,r}$ are the real and imaginary effective dielectric permittivity (Salat and Junge, 2010), $\tan\delta$ the material loss tangent, d the one-way travelled distance, f the frequency and μ'_0, μ'_r the magnetic permeability of free-space and the medium, respectively. It varies from 0.104 m/ns for sample 102 to a maximum of 0.157 m/ns for the clean coquina (sample 103). Note, however, that the water content for the clean coquina sample could be underestimated due to evaporative water loss during the transportation. As electromagnetic wave velocity and water content are inversely correlated due to the high dielectric permittivity of water (e.g., Topp-relationship, see also equation 6.1), the radar wave velocities can expected to be lower than the 0.157 m/ns. For the more clayey and organic samples this water loss is most likely less prominent. Sample 102 shows the maximum material attenuation with 19.35 dB/m at

100 MHz while the smallest attenuation was determined for sample 104 with 1.25 dB/m. In Figure 6.9 (left) we calculated the signal level taking into account all loss mechanisms described by Daniels, (2004).

The coquinas are mainly made by carbonate shells, cemented by calcite with practically no clay in the system and have a very high porosity and permeability. These factors make the coquina ridges a low loss dielectric medium, almost ideal for GPR surveys. A large portion of the attenuation most likely derives from scattering losses and at higher frequencies from the water in the system. Figures 6.10a and 6.10b show respectively one contact between two coquina layers at different scales. The nature of this contact is the key for the GPR response. At the contact, porosity and permeability are at least three times lower compared to the surrounding rock, characterised by a smaller grain size and a higher degree of cementation (see microstructure of the CTscan in Figure 6.10b with pores in yellow). These contact conditions provide enough dielectric contrast for strong GPR reflections along the stratigraphic interfaces, possibly due to structural or bedding contrast and elevated water content in the finer grain and pore section.

Before loading to Seiwork2d® and Geoprobe® (TD Halliburton) the 500 MHz data was processed using ReflexW and Promax® according to the processing flow described in Figure 6.11. One of the most important steps is the integration with high quality topographic data acquired using the differential GPS system. The few centimetres resolution of the spatial coordinates proved to be fundamental for revealing the geometry of the coquina layers.

For the time-depth conversion a walk-away common-shot point (CSP) experiment was done with 0.2 m increments between successive CSPs and a maximum of 20 m aperture. The velocity analysis is shown in Figure 6.12, with an optimum stack obtained with a velocity of 0.1347 m/ns from the ‘travel-time curve’. The semblance plot (Figure 12, right) shows the maximum energy from a reflection originating at a depth of 3 m with velocities of 0.135 m/ns. Also the slope of the direct arrival (brown line) supports this value. Note that this velocity is in good agreement with the values obtained from laboratory measurements for samples containing organic and finer materials (samples 101 and 104 in Figure 6.9).

The geometry for the 3D GPR acquisition is shown in Figure 6.13. Note the almost horizontal topography (in colour) superposed by a regular grid used for interpolation (every 5th inline/xline shown). A total of 53 lines were acquired with a 20 cm line spacing and a trace step of 7 cm. The 3D GPR data was processed using RadExPro software and a dedicated Matlab script was designed to assemble 3D volume from individual 2D lines. The processing flow can be summarised in the following:

1. Data load from Mala GPR files.
2. Navigation data processing (GPS coordinates of every line were transformed to UTM, filtered using 7-point alpha-trimmed running averaging and interpolated to obtain coordinate for every trace location).
3. DC removal.
4. Amplitude correction (AGC, 30 ns)
5. Interpolation to regular grid (10 x 10 cm, see Figure 6.13)
6. Bandpass filter (5-10-500-800 MHz)
7. 3D FK Stolt Migration (constant velocity, 14 cm/ns)
8. Terrain correction

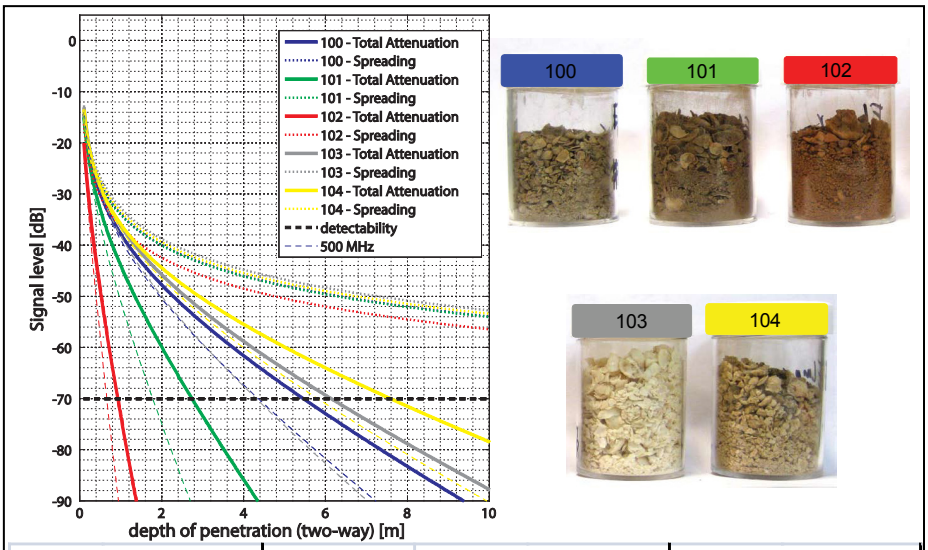

			110 MHz		250 MHz	
sample	comment	water content [w%]	velocity [m/ns]	attenuation [dB/m]	velocity [m/ns]	attenuation [dB/m]
100	on ridge	5.1	0.130	1.954	0.135	2.331
101	behind ridge	6.4	0.129	4.999	0.140	6.958
102	red	5.9	0.104	19.351	0.117	24.490
103	shell	2.0	0.157	1.752	0.165	2.278
104	organic	3.2	0.141	1.252	0.145	1.540

Figure 6.9. Laboratory analysis of water content, propagation velocity and attenuation for 5 representative samples of coquina. On the left we calculated the signal level of a reflection from a horizontal layer as a function of depth. Note that this signal level is not only dependent on material attenuation, but also on scattering losses and spreading losses (both dependent on wave length).

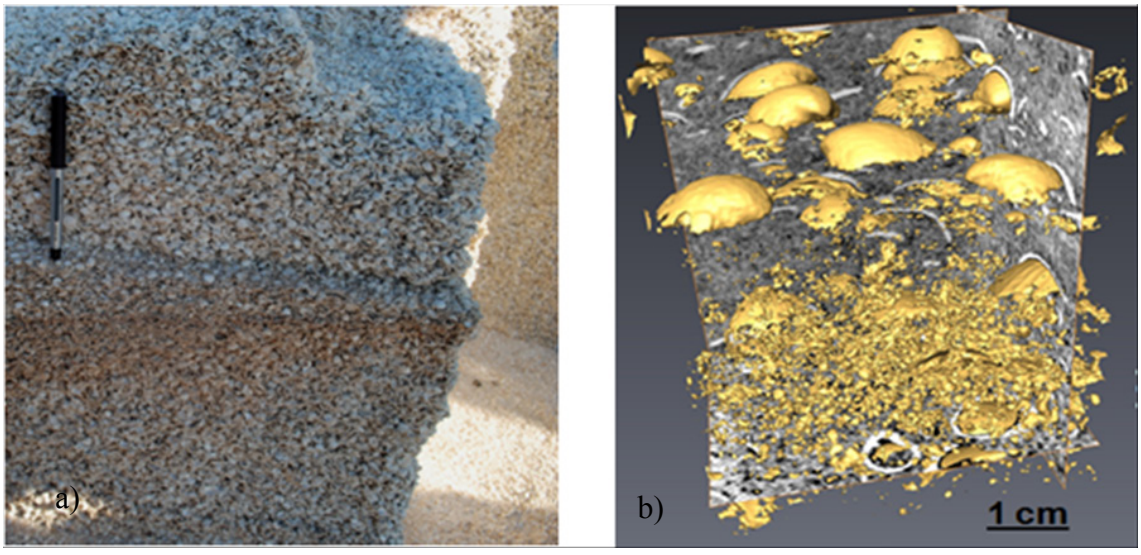

Figure 6.10. (a) Contact between two Coquina layers. Note how the shells are melted together with calcite cement, the different grain size in the contact and a small dip of the layer below. (b) Contact between two Coquina layers shown in a microCT scan. Note that the pore space in yellow is much smaller along the contact between the two layers.

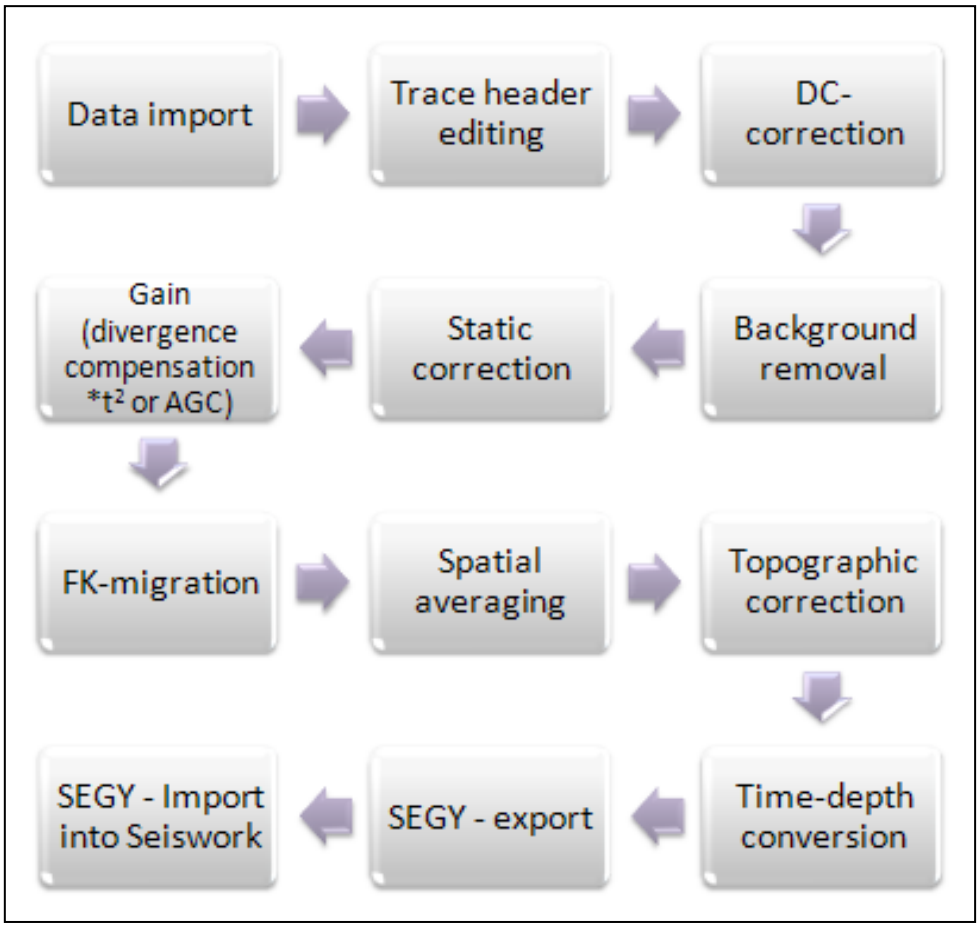

Figure 6.11. Processing flow used for 2D GPR data processing using ReflexW and ProMAX.

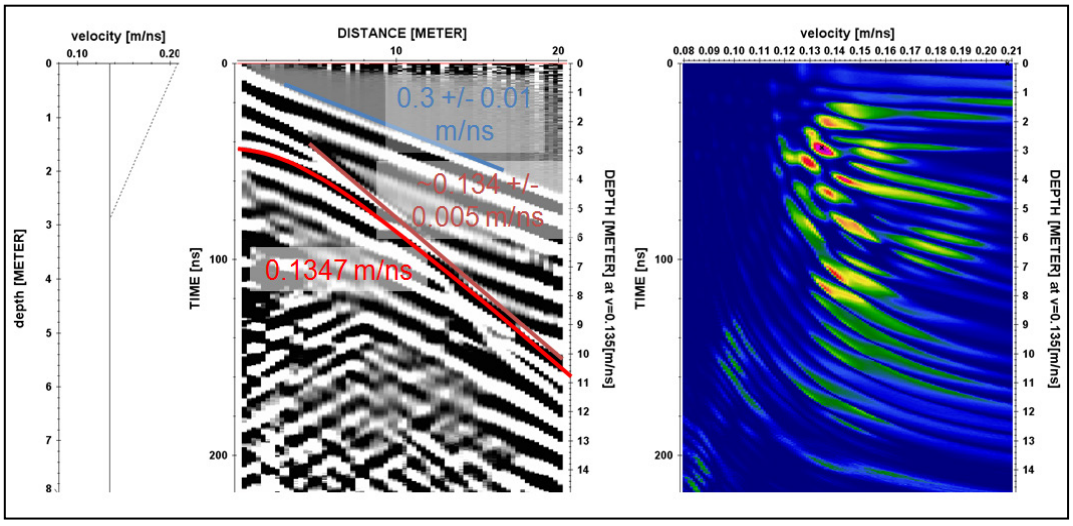

Figure 6.12. CSP velocity analysis in a section made of clean coquina layers overlain by ephemeral algal mat material. Note that we use the value of 0.135 m/ns for time-depth conversion of the GPR data. This value is in good agreement with the laboratory measurements of the velocity (Figure 6.9).

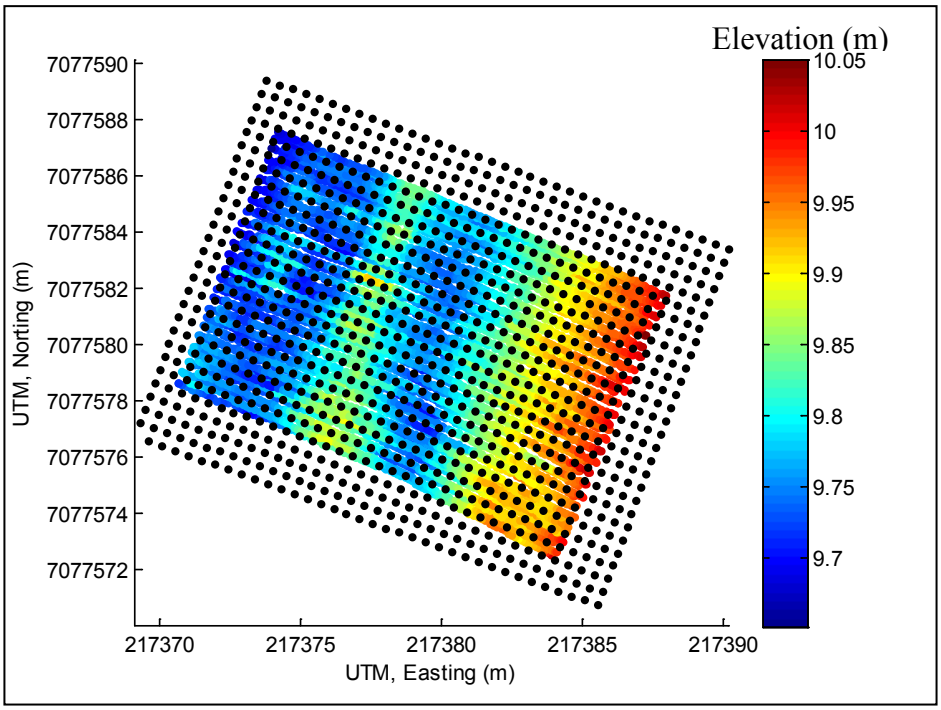

Figure 6.13. Geometry for the 3D GPR acquisition. Note the almost horizontal topography (in color) superposed by a regular grid used for interpolation (every 5th inline/xline shown). A total of 53 lines were acquired with a 20 cm line spacing and a trace step of 7 cm.

6.5. Seismic data analysis

Two main factors to consider in our seismic test line are the absence of long offsets and strong ground roll. These factors prevent the creation of a stacked section. Figure 6.14 is an example of CSP gathers in the middle of the section (green) showing also the lack of reflections. At the end points of the seismic line we get at least one reflector (Figure 6.15) at 45 ms with a stacking velocity of 1400 m/s. The depth of 32 m is probably a reflection from the top of Cretaceous (Toolonga Formation). This depth and P-wave velocity is consistent with the values obtained in the other extreme of the seismic line.

Nevertheless, the analyses of refraction data give us some clues about the elastic parameters of the coquinas layers. Figure 6.16 shows the travel time against offset. There are no shallow refractors, but an increase in P-wave velocity with depth and also a slightly lateral P-wave velocity change can be seen. We use the Herglotz-Wiechert formulation to perform a 1.5D inversion in the travel-time data. The inversion is based in a specialised tomographic-like algorithm that has been traditionally used in seismology (Nowack, 1990).

Figure 6.17 shows the velocities that come from the inversion of travel time curves using the Herglotz formula. The velocities change from almost 500 m/s at the top of coquina ridges to more than 2000 m/s at 10 meters depth. Note that the seismic line starts and ends at the top of two main ridges (high topography) classified as convex-up crest (see Chapter 6) and with tabular layers in between (Figure 6.18). The convex-up crests have more unconsolidated material and finer grains than the tabular layers. These factors can explain the lowest velocities obtained at the crests. The increasing P-wave velocity with depth probably reflects the increasing of compaction and cementation with depth. A slightly lateral change in P-wave velocities also can be seen from right to left in Figure 6.17 (dashed black lines) that reflects the tabular layers dipping to the ocean direction (smaller velocities to the ocean side). Figure 6.19 shows the P-wave velocities from the inversion using Herglotz formula against depth. The line in black describes the increase of velocity with depth. The following relation was obtained by fitting the compressional velocity V_P in meters per second with the depth Z in meters:

$$V_P(Z) = 1227 + 101.1Z, \tag{6.4}$$

The ultrasonic measurements were taken in three samples of coquinas to obtain P-wave velocities. They are all well cemented, but their porosities and internal microstructure change considerably. Porosities range from 35% to 56%, a dry density from 1.7 to 2.4 and the P-wave velocities from 1800 to 2300m/s. These velocities are higher than the values obtained from the inversion of refraction travel-time curves. One possible reason for that is some bias on sampling: the presence of intercalated coquina layers less cemented and sometimes not well consolidated are able to lower the average P-wave velocities derived from the refraction curves. We did not collect samples of these layers for our ultrasonic measurements.

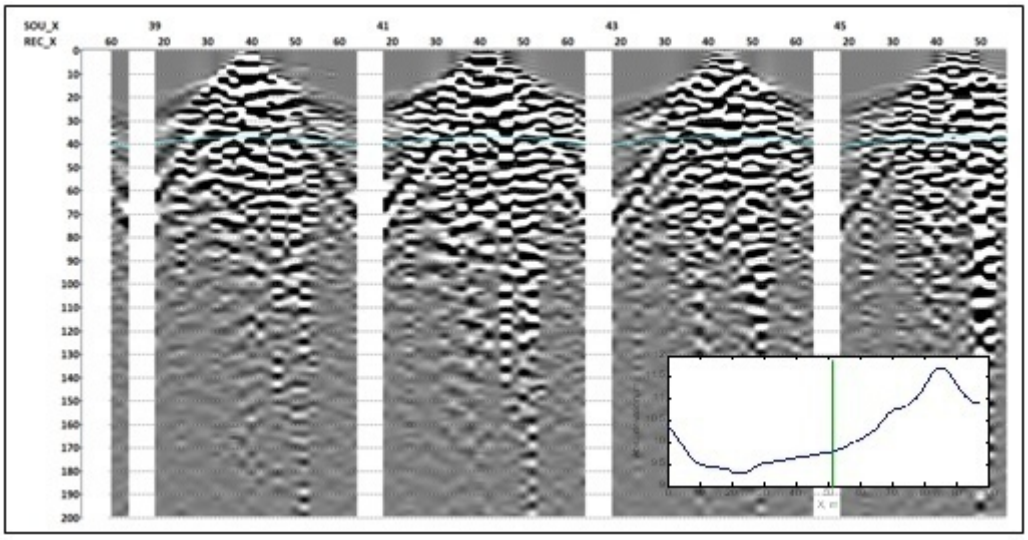

Figure 6.14. CSP gather in the middle of the section (line in green) showing the lack of reflections. The absence of long offsets and strong ground roll prevents from creating stacked section.

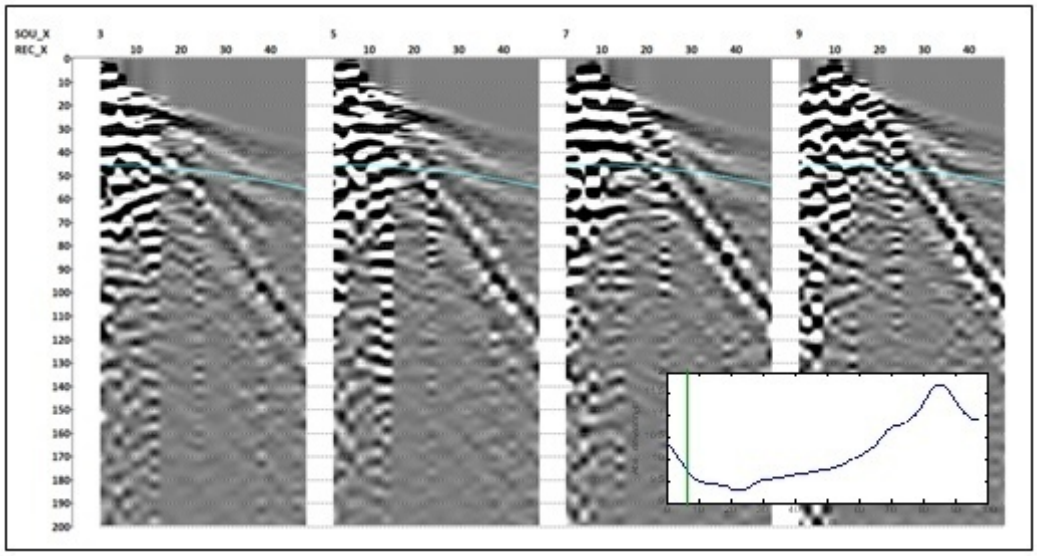

Figure 6.15. CSP gather in the beginning of the section (line in green) showing one reflection at 45 ms with velocity of 1400 m/s. The deep of 32 m are probably the Cretaceous boundary.

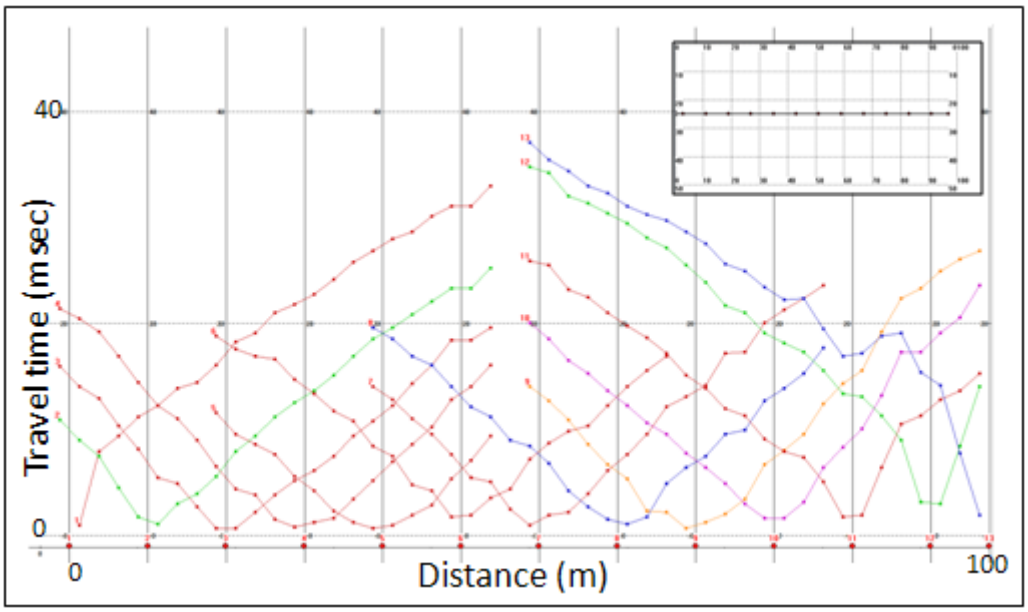

Figure 6.16. Travel-time curve analysis showing no shallow refractors, but a constant changing in the curve gradient due to increasing velocity with depth.

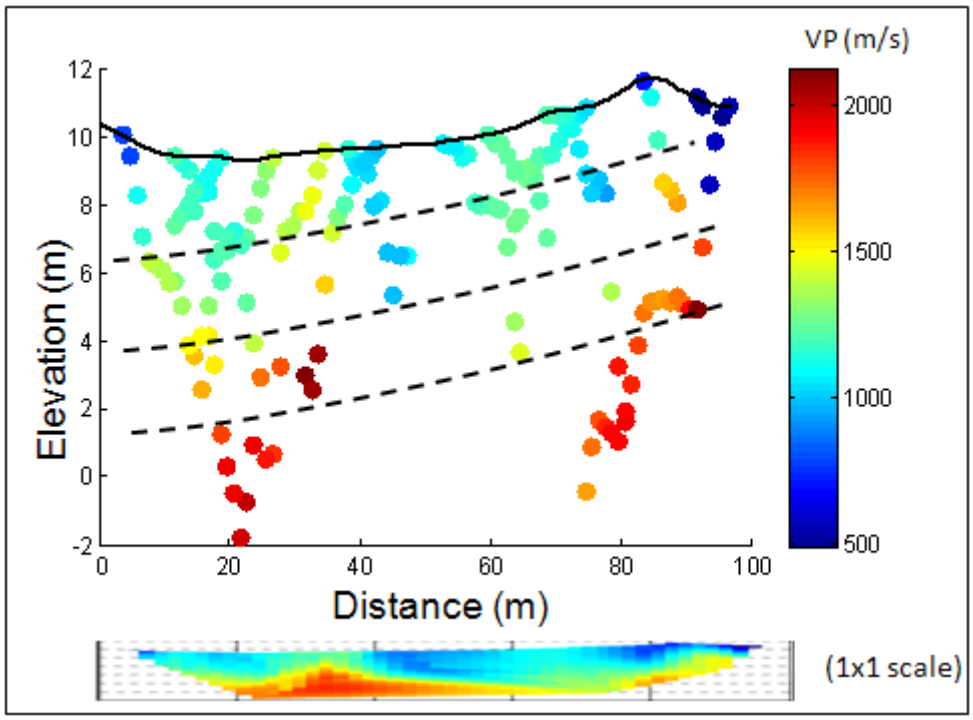

Figure 6.17. Inversion of travel-time curves using 1.5D inversion using the Herglotz formula. Note the velocities changing from close 500 m/s (circles in dark blue) at the top of coquina ridges to more than 2000 m/s at 10 m depth.

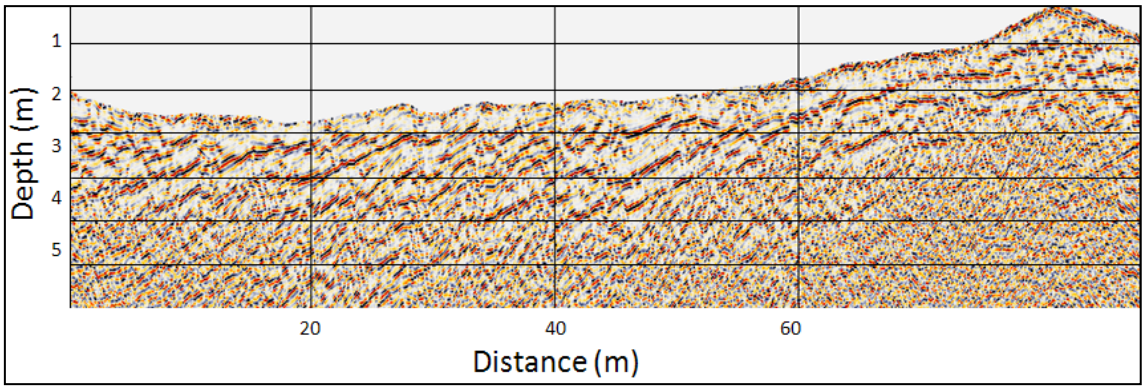

Figure 6.18. GPR section at the same location of seismic line 01. Note the coquina layers dipping towards the ocean side. A similar trend of velocities is observed in Figure 6.17.

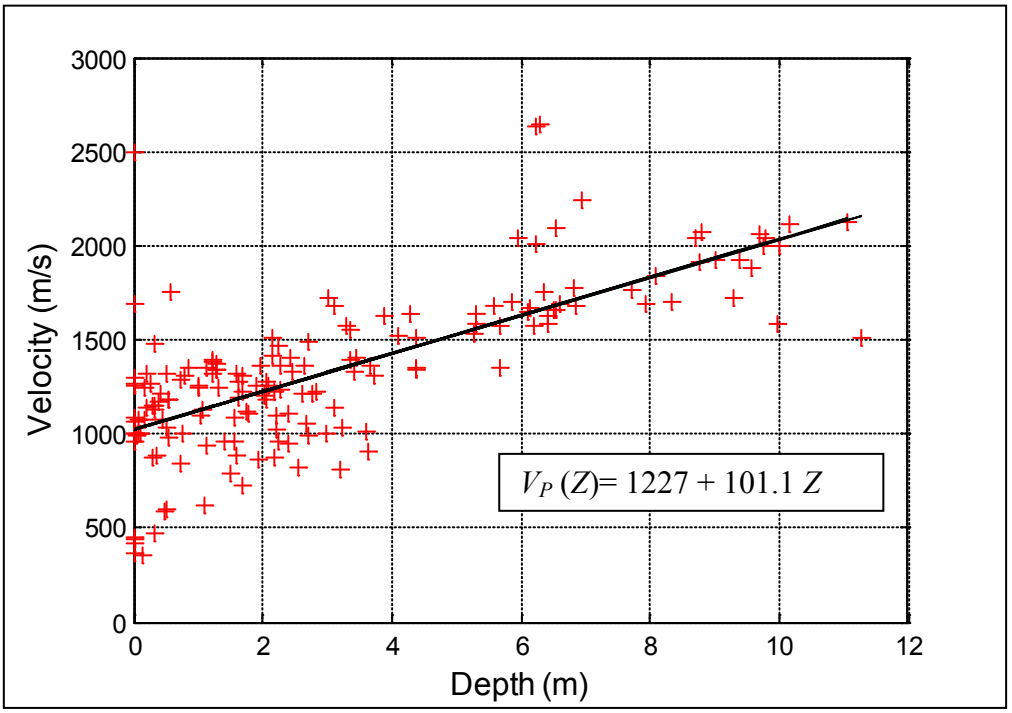

Figure 6.19. P-wave velocities obtained from inversion using the Herglotz formula against depth. The line in black describes the increasing of P-wave velocity (V_P) with depth (Z). The equation for $V_P(Z)$ is the best linear fit for all points.

6.6. Discussion

We discuss here the main results from the integration of field observations, drilling cores and ^{14}C dating along the surface of two sections and from a trench (2.6 m depth) and the correlation with the high resolution images provided by GPR surveys. The ^{14}C dating was measured at the Radiocarbon Data Centre of Australian National University (ANU)

Figure 6.20 shows a portion of GPR section acquired in one of highest coquina ridges. The contact between the Bibra and Dampier Formations (both Pleistocene) are projected based on well information along the section. As the GPR can only image above the water table, most of the sections will image only the Holocene coquinas layers well. In this section three classes based on morphology were classified: tabular layers, convex-up crest and washover fan. The ocean is in the left side of the Figure 6.20, with a clear accretion of coquina layers in that direction.

Figure 6.21 shows a GPR section close to a trench where nine carbonate samples were collected and dated. The ^{14}C dating starts from 2775 years at the bottom to 2240 years at the top meaning that 2.6 m of coquina takes around 500 years to be deposited. An average deposition rate of 0.5 cm/year does not mean much, because coquina deposition is a catastrophic event. Figure 6.21 also shows sequences of tabular layers (in colours) dipping to the ocean side (left side of the figure). Some erosion patterns can also be interpreted from the discordances present in the GPR section.

From the correlation of ^{14}C dating of 50 samples distributed along the two transects (Figure 6.22) and the events mapped with the GPR sections we can estimate an average rate of one event every 13 years. From the trench of Figure 6.23 we interpreted five sequences composed of 20 layers deposited in 500 years. This gives one event every 25 years. The rates from the transect (1/13) are lower than the rate from the trench dating (1/25), but represents better the whole area.

The cycle obtained here (1/13) does not fit with the cyclones cycles observed by Australian Bureau of Meteorology (1/5) therefore the coquinas deposition are due to cyclones (Category 5?) not computed by the Australian Bureau of Meteorology.

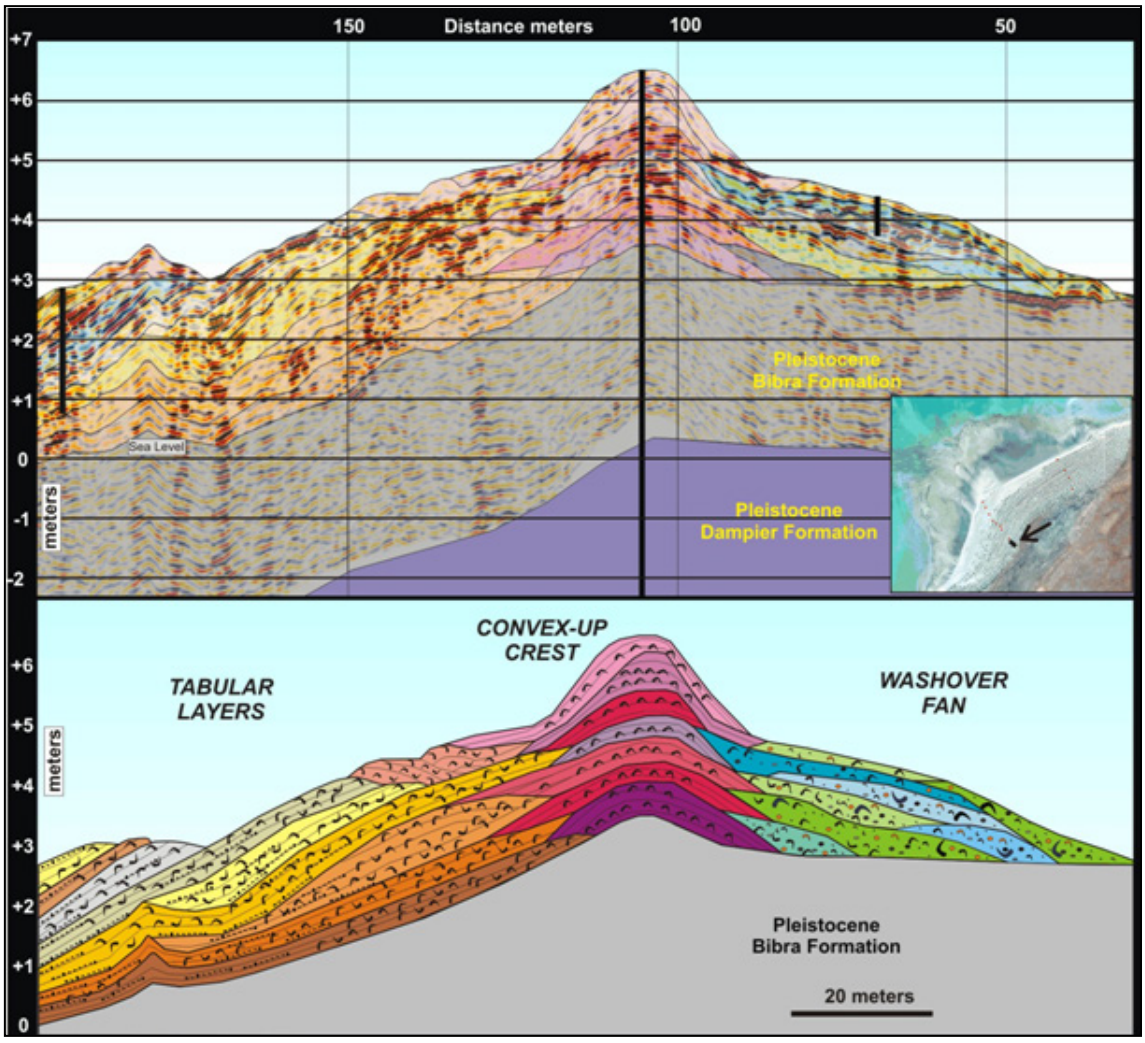

Figure 6.20. Part of a GPR section (above) in one of highest coquina ridges showing with the interpretation of the contact between Bibra and Dampier Formations (both Pleistocene) calibrated by one well. Below are the Holocene coquinas layers, classified here in three classes: tabular layers, convex-up crest and washover fan. The ocean is on the left side of this figure, with a clear accretion of layers in that direction.

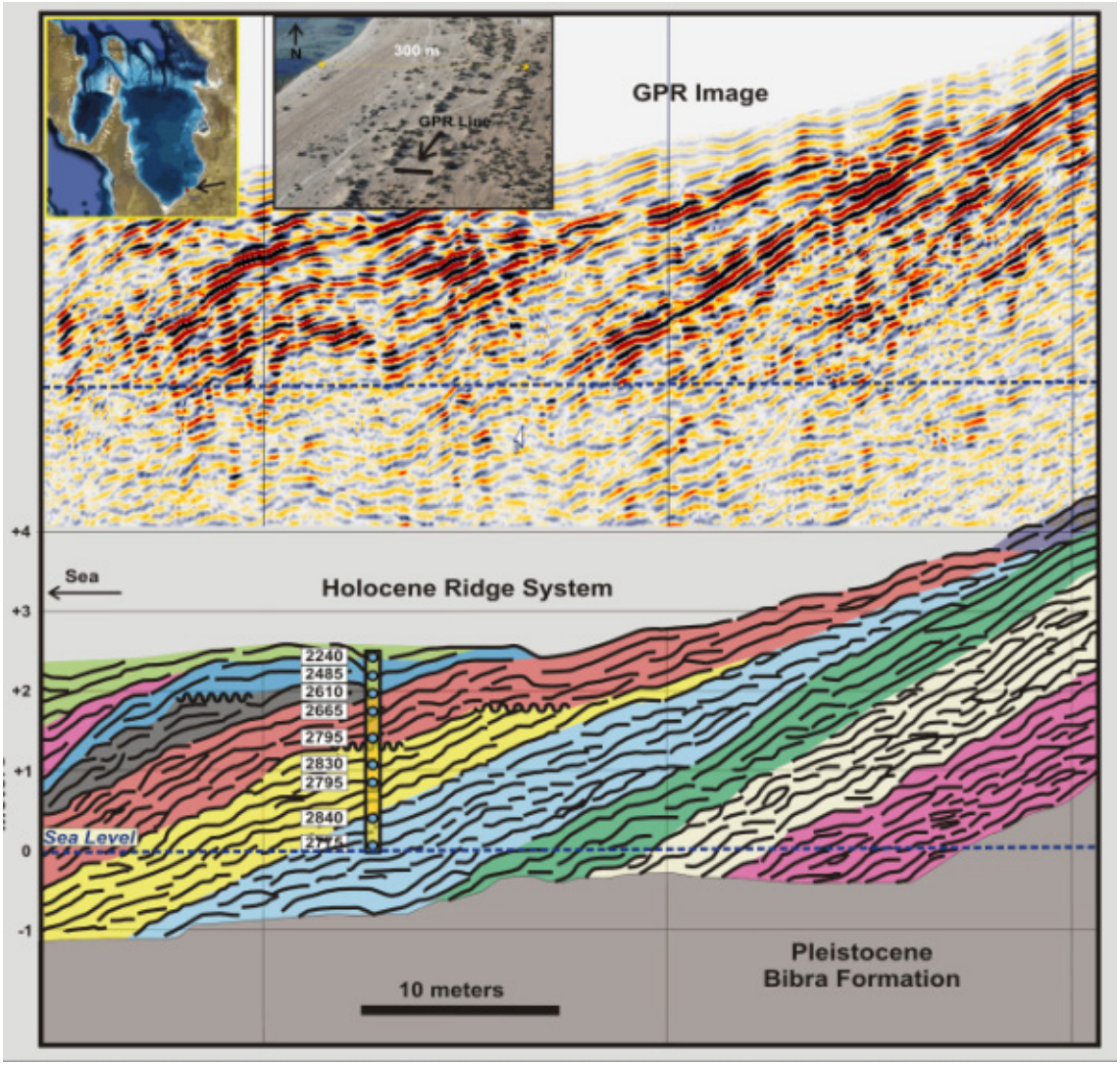

Figure 6.21. Part of a GPR section close to a trench where carbonate samples were collected and dated. The ^{14}C dating from 2775 years at the bottom to 2240 years at the top. These 2.2 m of coquina takes around 500 years to be deposited. This section shows sequences of tabular layers (in colours) dipping to the ocean side. Some erosion patterns also can be interpreted from the discordances present in the GPR section.

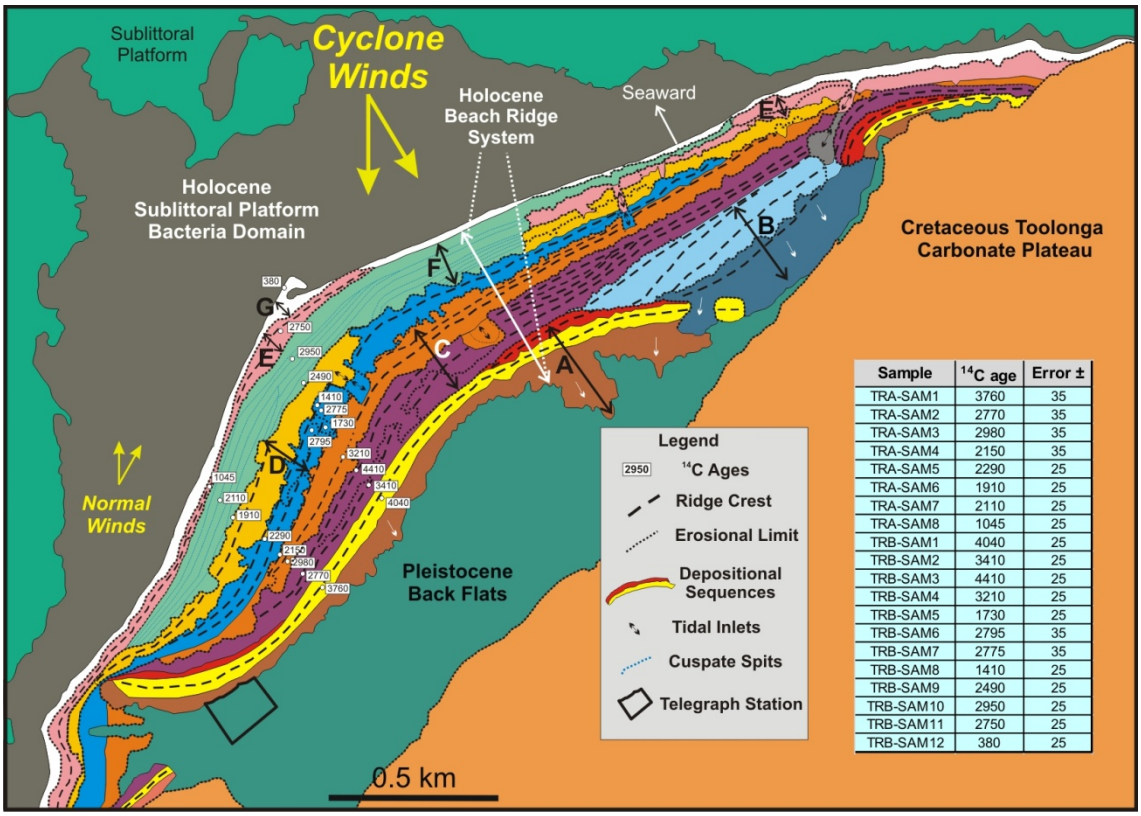

Sample	^{14}C age	Error ±
TRA-SAM1	3760	35
TRA-SAM2	2770	35
TRA-SAM3	2980	35
TRA-SAM4	2150	35
TRA-SAM5	2290	25
TRA-SAM6	1910	25
TRA-SAM7	2110	25
TRA-SAM8	1045	25
TRB-SAM1	4040	25
TRB-SAM2	3410	25
TRB-SAM3	4410	25
TRB-SAM4	3210	25
TRB-SAM5	1730	25
TRB-SAM6	2795	35
TRB-SAM7	2775	35
TRB-SAM8	1410	25
TRB-SAM9	2490	25
TRB-SAM10	2950	25
TRB-SAM11	2750	25
TRB-SAM12	380	25

Figure 6.22. Main depositional sequences of coquinas mapped in Telegraph Station with location of the samples dated with of ^{14}C. Note the range of dating from 380 years close to shore line to 4040 years over the oldest ridge crest (yellow).

6.7. 3D GPR interpretation

The SGY cube loaded in Geprobe® consists of 152 traces by 88 lines corresponding to 15 x 12 meters in area extension. The GPR trace sampling frequency was 8.8 GHz and the distance between traces of 5 cm. The reflection strength amplitude (Figure 6.23a) reveals details that cannot be detected in surface observation. As described before, this survey is in the domain of tabular layers, between two huge convex-up crests. As we will see in the following paragraphs, these tabular ridges are not monotonous, but show a relatively complex spatial relation including variations in geometry, thickness, azimuth and slope. The coquina sets are mainly parallel to shoreline and dipping towards offshore. Nevertheless, sometimes discontinuities can be observed only a few meters apart, probably driven by wave energy, topography and availability of shells.

The discontinuities can also be post-depositional, caused by carbonate dissolution along preferred fractures or even small faults. This spatial behaviour can be better seen in the structural cube (Figure 6.23b) obtained from dip and azimuth attributes. Other indications of the carbonate dissolution with possible collapse along small faults are shown in the GPR sections, like the one displayed in Figure 6.24. The features isolated in the left of Figure 6.24 show a collapsed structure with the movement following the red arrow and along two vertical faults in black dashed lines. This event is much localised in time since the following coquina layer deposited over the feature is not affected by it. On the other hand, the event mapped on the right side of Figure 6.24 is clearly much younger, since the left fault that isolated the collapsed wedge is continuous close to the surface (dashed line in black).

Figure 6.25 shows the absolute amplitude attribute for increasing time slices, from the surface (upper left) to 3.3 meters depth (lower right). This sequence shows that the events were very distinct, with a difference of at least 30 degrees for the older events related to the actual shore line and the main directions of younger layers as shown at 0.00m and 0.60m time slices.

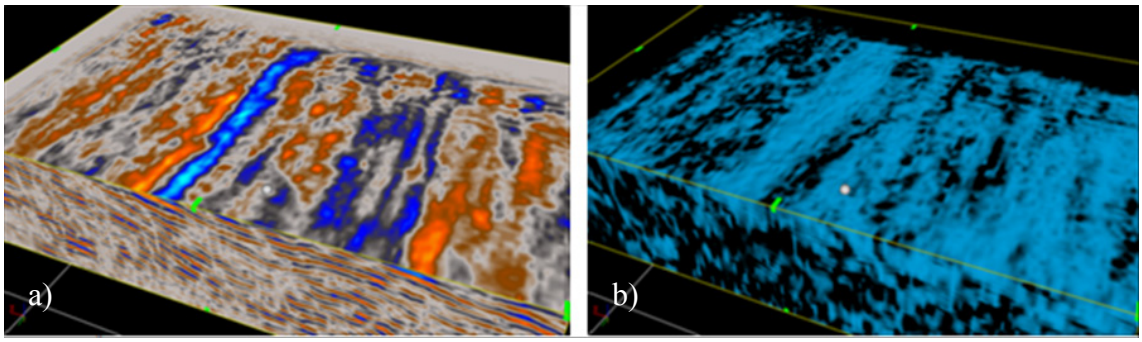

Figure 6.23. (a) GPR Reflection strength cube. Note the lack of lateral continuity along certain layers in the time slice and the changing layers deeps along the depth section; (b) GPR Structural Cube. Note some lineaments in black that are not concordant with the layering directions, suggesting some small faulting, clearly post depositional events.

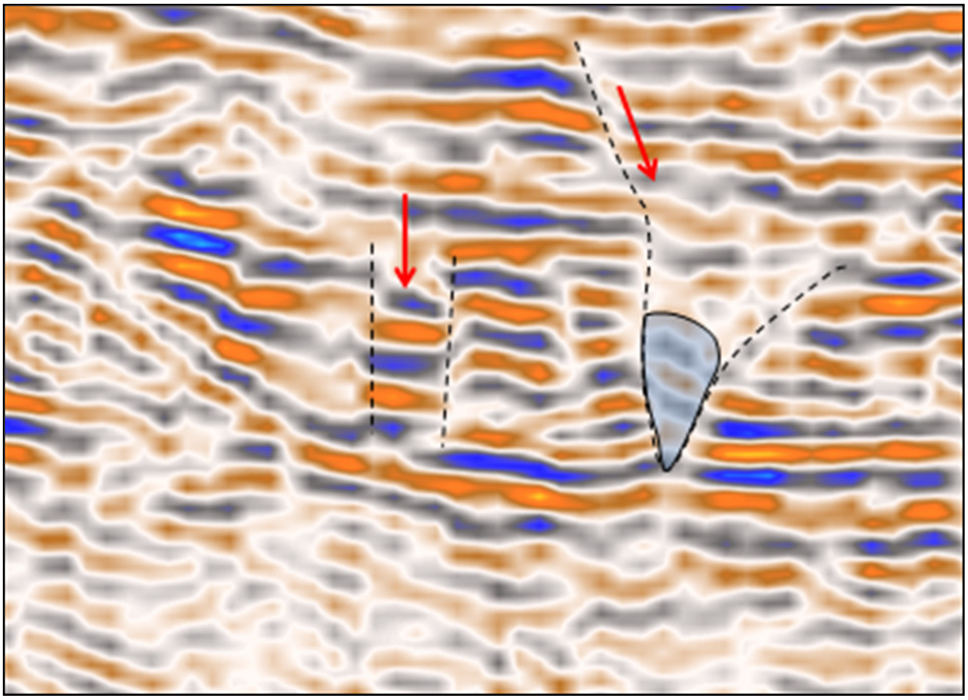

Figure 6.24. Amplitude attribute section showing small faulting related to collapsing blocks. These features are probably caused by caves originated by carbonate dissolution.

Figure 6.26 shows a detailed interpretation of coquina layers along a 2D GPR section. In a small interval of less than 3 m we can detail at least two main transgressive layers caused by strong storms (black arrows) overlaying a sequence of three layers that represent the overall regression of the system (dashed black arrow). The 3D representation of this context is shown in Figure 6.27, where the coloured (by depth) surface represents one of the transgressive events described above and the layer in grey represents one set of the regression system. This is the 3D representation of the head snake normally seen in 2D sections.

The RMS attribute using a window of +/- 1m and projected in the transgressive horizon described above is shown in Figure 6.28. The RMS anomalies in red show trends that suggest this surface was exposed for a longer period of time (relative to the overlaying layers). The picture on the right side of Figure 6.28 shows an exposed surface today that should have a similar GPR response once buried. In this picture the coquinas (beach rocks) show two distinct cementation degrees and microstructures that definitely will affect the reflectivity as shown in the laboratory measurements (Figure 6.9).

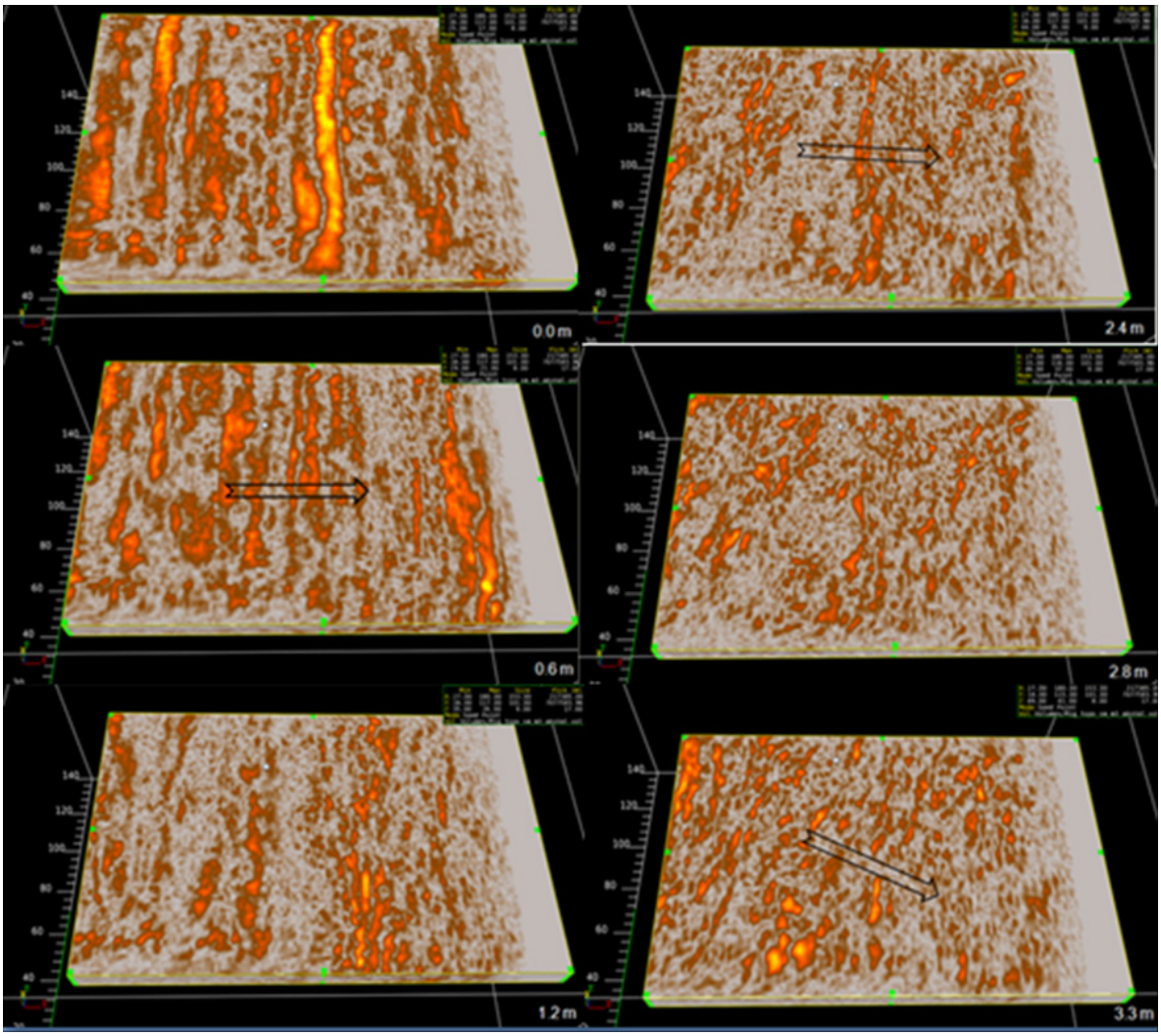

Figure 6.25. Absolute amplitude attribute for increasing time slices, from the surface (upper left) to 3.3 meters depth (lower right). Note the distinct depositional direction of the overlapping events.

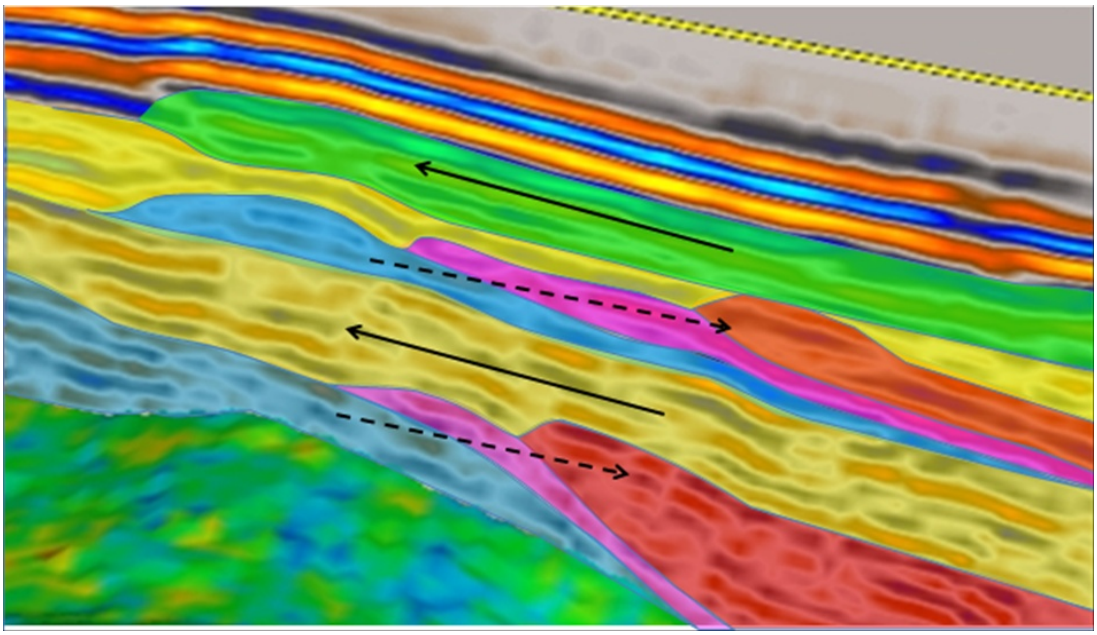

Figure 6.26. GPR amplitude section showing a sequence of events. The dashed black lines represent a regression while the black lines are small transgressions due to strong storms.

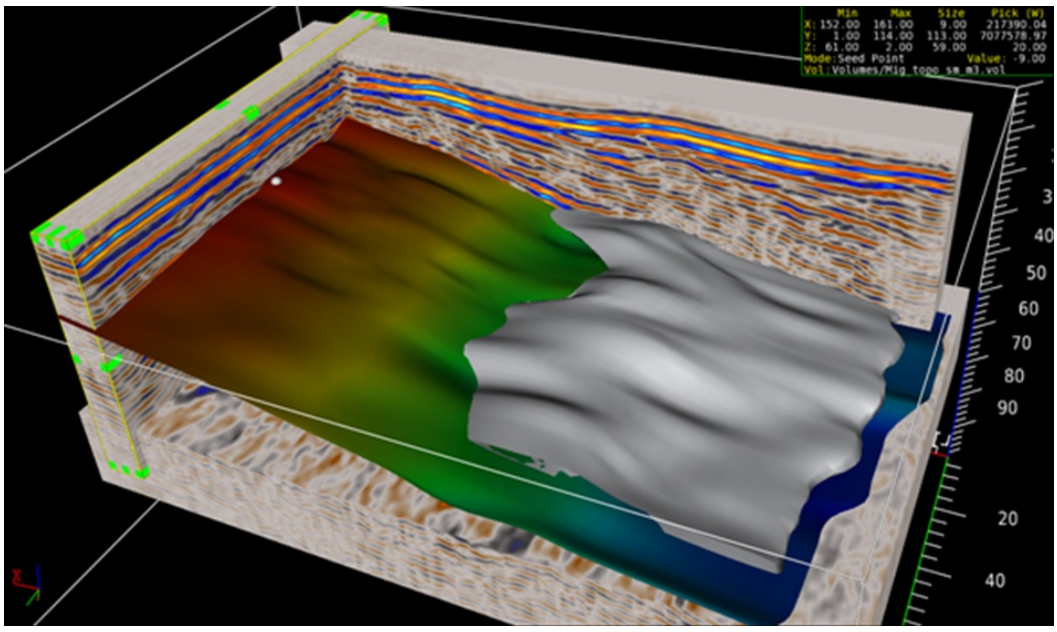

Figure 6.27. Spatial relation between one transgressive event (coloured by depth) and one set of the regression events (layer in grey).

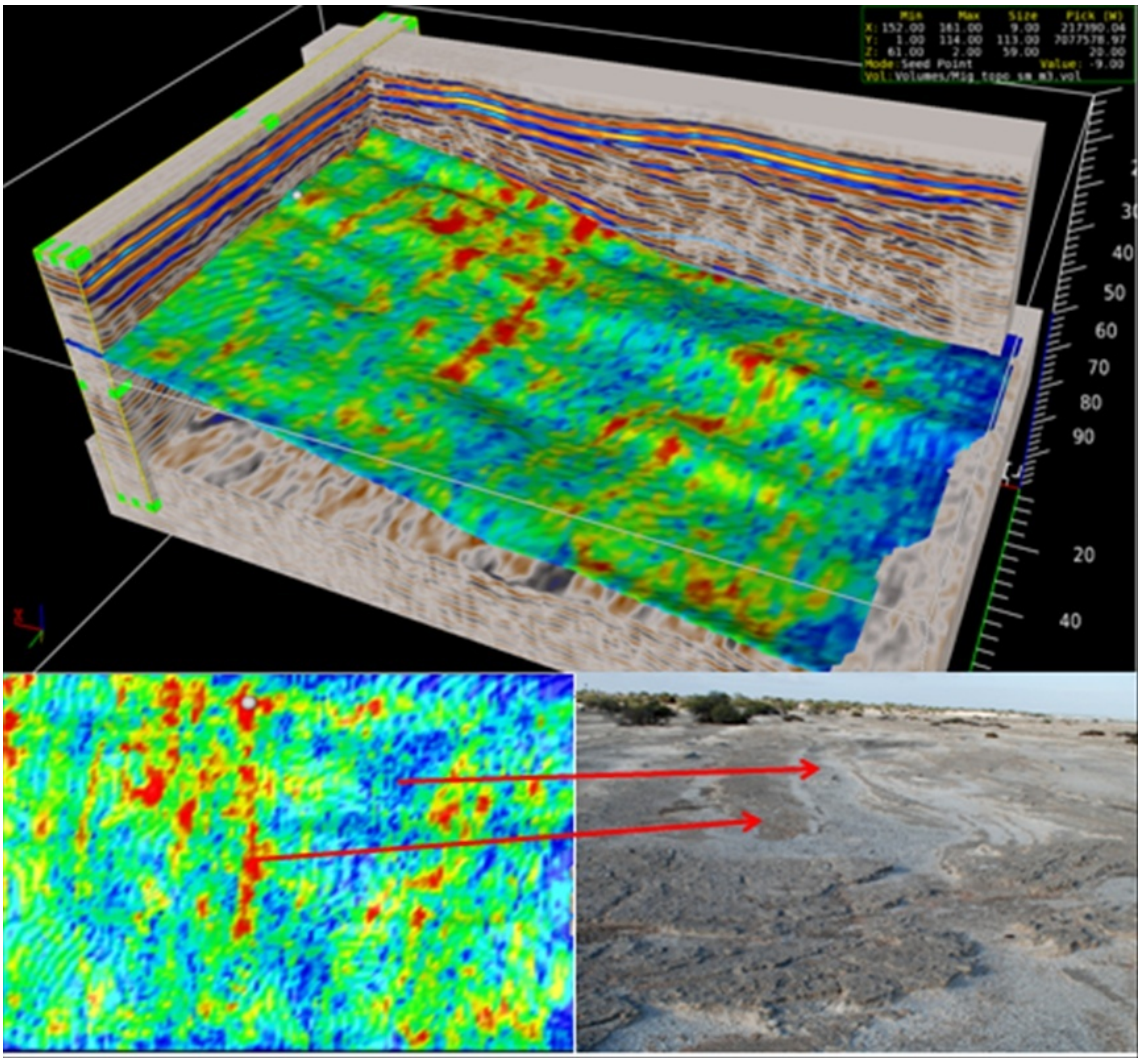

Figure 6.28. The RMS attribute using a window of +/- 1m and projected in the transgressive horizon. The anomalous trends in red suggest that this surface was exposed. The picture on the right side shows an exposed surface today that should have a similar GPR response once buried. In this picture the coquinas (beach rocks) shows distinct cementation degrees and microstructures that definitely will affect the reflectivity and attenuation as shown in the laboratory measurements (see Figure 6.9).

6.8. Conclusions

GPR worked very well in the carbonate sequences of Shark Bay. This is due mostly to the fact that the coquinas are mainly made by carbonate shells and cemented by calcite with practically no clay in the system. These factors, combined with the characteristics of the contacts between coquina layers (smaller grain size highly cemented) and the dry weather experienced during the acquisition gives the conditions for the good GPR response of Shark Bay carbonate sequences. The coquina ridges are a low loss dielectric medium, almost ideal for GPR surveys.

The absence of long spreads and high level over ground roll in the seismic data were responsible for poor imaging of coquina ridges and reflections from underlying surfaces in Telegraph Station. Even with the low coverage we were seeing a reflection from the end of spreads from a depth of 32 m, which is probably the Cretaceous boundary (Toolonga Formation).

Inversion of the refraction curve gives us the velocity profile for the coquina layers, with an increasing P-wave velocity with depth and a slightly lateral decreasing P-wave velocity towards the ocean. This is also compatible with the trends shown by the GPR images.

Ultrasonic velocities taken from representative coquina samples give higher velocities than those derived from reflection and refraction seismic data. The possible reason for that, besides the distinct frequency of measurements, is the bias introduced by sampling. The averaged smaller values of P-wave velocities from seismic data are probably due to less consolidated and less cemented coquinas layers not sampled.

The lateral accretion of coquina layers towards the ocean is a clear signal of the sea regression during the Holocene. The high resolution of GPR sections allows the mapping of the Holocene sequence of coquinas layers. Three classes were identified: tabular layers, convex-up crest and washover fan. Besides their spatial relations, erosion patterns can also be interpreted from the discordances that appear in the GPR section. The contact between the Bibra and Dampier Formations (both Pleistocene) is not always possible to detect, because most of the time the contact is below the water table.

From the correlation of ^{14}C dating of 50 samples distributed along the two transects and the events mapped with the GPR sections, we estimate an average rate of one cyclone (probably Category 5) every 13 years.

Detailed information of internal structures of the coquina layers is possible due the high quality 3D GPR dataset. The 3D data was acquired in an area where the tabular layers are dominant. The snake head geometry of some coquina layers is evident, as well as the superposition of events, which are very dependent of energy availability in the system. From our interpretation, the Holocene regression is continuous but not homogeneous.

Carbonate dissolution features were able to be interpreted using 3D amplitude attributes. Small faults were mapped and probably related to features of collapsing blocks in ancient caves. The data also show that the main direction of coquina deposition changes with time. Horizon attribute interpretation also reveals trends and discontinuities that can add value to the understanding of porosity and permeability in coquina reservoirs in the earlier stages of diagenesis.

CONCLUDING REMARKS

In this thesis we have explored petrophysical and elastic properties of carbonates that directly impact quantitative seismic interpretation of carbonate systems. Our multi scale approach starts from (1) the nano and micro scale, through nanoindentation and digital rock techniques, (2) ultrasonic measurements and elastic modelling through computational rock physics, (3) testing the validity of Gassmann's fluid substitution using cores and well logs, (4) analysis of the parameters that control stress dependency of elastic parameters , (5) squirt flow modelling at ultrasonic frequencies that give a new understanding of seismic wave attenuation and dispersion and (6) seismic and GPR interpretation of the carbonate reservoir analogue in Shark Bay, WA, which provide information about carbonate properties distribution in an early diagenesis and facies association. All these approaches are linked and the developed workflows can be used in complex carbonate reservoirs to minimise the risks of the hydrocarbon exploration business. The main results of each chapter can be summarised as follows:

- Chapter 2. Calcite elastic parameters such as bulk and shear moduli, Poisson ratio and Young Modulus are basic in any modelling and normally taken from rock-physics tables. We show here that this might not be accurate, because these parameters can change considerably due to variations of the carbonate framework. We use the nanoindentation technique in an oolitic limestone to directly measure the Young modulus. We have found a large variation in the Young modulus E, clustered in two classes and centred at 56 and 144 GPa (from the tables E=70 GPa). We interpreted the high values of the Young moduli as genetically associated to bio generated calcite (biocalcite). We associate the small values with microporosity, undetectable by our microCT or even SEM images. We also use computational rock physics in the X-ray CT images of the oolite using FDM with our measured Young modulus E values. The microCT image segmentation considered the two phases of calcite and the results are in good agreement with ultrasonic measurements.
- Chapter 3. Fluid substitution using Gassmann's equations in carbonates is always challenging because they are much less predictable than in sandstone reservoirs. Also, the upscale from ultrasonic measurements (KHz) to log domain (MHz) and to seismic domain (Hz) is not straightforward since one of the

assumptions of Gassmann's equations says that they are valid only in the low frequency domain. For this study we use ultrasonic data from 50 samples from a single well interval and a sonic log data. The reservoir interval is water fully saturated and the ultrasonic velocities were taken in a range of confining pressures from dried samples. We obtain a good agreement between the elastic properties obtained from core and log measurements. This shows that Gassmann fluid substitution is applicable to these carbonates, at least at sonic log frequencies.

- Chapter 4. Porosity and permeability prediction is challenging in carbonates because of the dynamic of post-depositional history involving dissolution and mineral transformations. To address this problem we investigate the relations between porosity and ultrasonic wave propagation in dry carbonate samples. We use a complex dual porosity, where the total porosity is composed of stiff (more rounded pores) and compliant pores (like fracture or penny shaped pores) (Murphy et al., 1986). We then estimate compliant porosity and aspect ratio from the stress dependency of dry rock compressibility using the Shapiro isotropic model (Shapiro, 2003). In this study we use the same carbonate dataset from the Santos Basin as previously described, that have ultrasonic measurements in a range of pressures from 5 to 40 MPa. The results show a good correlation between compliant porosity and dry bulk modulus, and total porosity and density for the 29 samples of carbonates from the Santos Basin. The data show different correlations for different facies.
- Chapter 5. When dealing with ultrasonic measurements, one effect that needs to be taken in account is the squirt flow which is caused by the interaction between the saturating fluid and the passing ultrasonic wave used in the experiments. This effect stiffens the bulk modulus of the saturated sample and needs to be considered when modelling ultrasonic lab data. Here we use an alternative approach to model squirt flow using the model derived by Gurevich et al. (2010), which includes the dual porosity concept of Shapiro (2003) and assumes the existence of undetectable compliant pores at the level of laboratory confining pressures. We add the contribution of stiff pores in the stress dependency of elastic parameters, taking into account the small compliance of stiff pores at ultra-high pressures (500-600 GPa). For our test we use 66 samples of sandstones (Han et al., 1986). Our predictions of saturated elastic parameters as

a function of confining pressures fits better with the measured elastic parameters than the low or high frequency limits of Gassmann (1951) or Mavko and Jizba (1991).

- Chapter 6. The carbonate system of Telegraph Station, Shark Bay (WA) is one the most complete developments of a unique environment where coquinas, stromatolites and microbial mats near the coast are linked. It is an excellent analogue to the carbonate pre-salt reservoir offshore Brazil. To investigate the origin, stratigraphy, internal structure and storm record preserved in the coquinas we acquired and interpreted 7.5 km of GPR data and high resolution seismic data. Although the seismic data did not show clear images due the absence of long offset and strong ground roll, the coquina ridges showed excellent high resolution GPR images. The coquina ridges of Telegraph Stations are a low loss dielectric medium, almost ideal for GPR surveys. Three classes of coquinas were identified and mapped: tabular layers, convex-up crest and washover fan. From the correlation of 14C dating of 50 samples distributed along the two transects and the events mapped with the GPR sections, we can estimate an average rate of one (Category 5) cyclone every 13 years. The high quality 3D GPR dataset shows clearly the snake head geometry of some coquina layers, and the superposition of events. The Holocene regression is continuous but not homogeneous from our interpretation. Carbonate dissolution features were also possible to be interpreted using 3D amplitude attributes, with small faults probably related to features of collapsing blocks in ancient caves. The data also shows that the main direction of coquina deposition changes with time. Horizon attribute interpretation also reveals trends and discontinuities that can add value to the understanding of porosity and permeability in coquina reservoirs in the earlier stages of diagenesis. Analysis of these features increases our understanding of reservoir porosity and permeability distribution in carbonate deposits, and can be used to constrain reservoir properties in pre-salt carbonates in Brazilian basins.

REFERENCES

Adam, L., M. Batzle, and I. Brevick, 2006, Gassmann's fluid substitution and shear modulus variability in carbonates at laboratory seismic and ultrasonic frequencies: Geophysics, **71**, 173-183.

Adelinet, M., J. Fortin, Y. Gueguen, A. Schubnel, and L . Geoffroy, 2010, Frequency and fluid effects on elastic properties of basalt: Experimental investigations: Geophys. Res. Lett., **37**, doi, L02303 10.1029/2009GL041660.

Adetunji, A. Q., A. Al-Shuhail, and G. Korvin, 2008, Mapping the internal structure of sand dunes with GPR: A case history from the Jafurah sand sea of eastern Saudi Arabia: The Leading Edge, 1446-145.

Agersborg R., T. A. Johansen, M. Jakobsen, J. Sothcott, and A. Best, 2008, Effects of fluids and dual-pore systems on pressure-dependent velocities and attenuations in carbonates: Geophysics, **73**, 35-47.

Arns, C.H., M. A. Knackstedt, W. V. Pinczewski, and E. J. Garboczi, 2002, Computation of linear elastic properties from microtomographic images: Methodology and agreement between theory and experiment: Geophysics, **5,** 1396-1405.

Baechle, G. T., R. J. Wegner, , G. Eberli, J. L. Massaferro, and Y. F. Sun, 2005, Changes of shear moduli in carbonate rocks: implications for Gassmann applicability: The Leading Edge, **24**, 507-510.

Batzle, M.L., D.-H. Han, and R. Hofmann, 2006, Fluid mobility and frequency dependent seismic velocity: direct measurements: Geophysics, **71**(1), N1–N10.

Berry, P. F., and P. E. Playford, 1997, Biology of modern Fragum erugatum (Mollusca, Bivalvia, Cardiidae) in relation to deposition of the Hamelin Coquina, Shark Bay, Western Australia: Marine and Fresh Water Research, **48,** 415-420.

Berryman, J. G., 1980, Long-wavelength propagation in composite elastic media—I. spherical inclusions: Journal of the Acoustical Society of America, **68**, 1809–1831.

Biot, M. A., 1962, Mechanics of deformation and acoustic propagation in porous media: Journal of Applied Physics, **33**, 1482-1498.

Bruet, B. J. F., H. J. Qi, M. C. Boyce, R. Panas, K. Tai, L. Frick, and C. Ortiz, 2005, Nanoscale morphology and indentation of individual nacre tablets from the gastropode mollusk Trochus niloticus: Journal of Materials Research, **20**, 2400-2419.

Chapman, M., S. V. Zatsepin, and S. Crampin, 2002, Derivation of a microstructural poroelastic model: Geophysical Journal International, **151**, 427-451.

Choquete, P. W. and L. C. Pray, 1970, Geologic nomenclature and classification of porosity in sedimentary carbonates: AAPG Bulletin, **54**, 207-244.

Collins, L. B., J-X. Zhao, and H. Freeman, 2006, A high precision record of mid-late holocene sea-levels events from emergent coral pavements in the Houtman Abrolhos Islands, southern Australia: Quaternary International, **145/146**, 78-85.

Constantinides, G., K. S. R. Chandranc, F. J. Ulma, and K. J. V. Vliet, 2006, **G**rid indentation analysis of composite microstructure and mechanics, principles and validation: Material Science and Engineering, **430**, 189-202.

Christensen, R.M., 2005, Mechanics of composite materials: Dover Publications.

Daniels, D. J., 2004, Ground penetrating radar: The institute of Electrical Engineers, London, UK.

De Paula, O. B., M. Pervukhina, and B. Gurevich, 2008, Role of compliant porosity in stress dependency of ultrasonic velocities in carbonates and sandstones: III Simposio Brasileiro de Geofisica, SBGf, Expanded Abstracts.

De Paula, O. B., B. Gurevich, M. Pervukhina, and D. Makarynska, 2009, Application of a new model of squirt-flow attenuation and dispersion in carbonates: 71th EAGE Conference & Exhibition, Expanded Abstracts.

De Paula, O. B., M. Pervukhina, and B. Gurevich, 2010, Testing Gassmann fluid substitution in carbonates: sonic log versus ultrasonic core measurements: 80th International Annual Meeting, SEG, Expanded Abstracts.

De Paula, O. B., M. Pervukhina, B. Gurevich, M. Lebedev, M. Martyniuk, and C. Delle Piane, 2010, Estimation of carbonate elastic properties from nanoindentation experiments to reduce uncertainties in reservoir modelling: 21th International Geophysical Conference & Exhibition, Expanded Abstracts.

De Paula, O. B., B. Gurevich, M. Pervukhina, M. Lebedev, M. Martyniuk, and C. Delle Piane, 2010, Estimation of carbonate elastic properties using nanoindentation and digital images: 72th EAGE Conference & Exhibition, Expanded Abstracts.

De Paula, O. B., M. Pervukhina, D. Makarynska, and B. Gurevich, 2012, Modeling squirt dispersion and attenuation in fluid saturated rocks using pressure dependency of dry ultrasonic velocities: Geophysics, **77**, 157-168.

Dunhan, R. J., 1962, Classification of carbonate rocks according to their depositional texture, in W.E. Ham, ed., Classificatio of Carbonate Rocks – a symposium: Tulsa, OK, AAPG Memoir 1, 108-121.

Dvorkin, J., G. Mavko, and A. Nur, 1995, Squirt flow in fully saturated rocks: Geophysics, **60,** 97–107.

Dvorkin, J., N. Derzhi, E. Dias, and Q.Fang, 2011, Relevance of computational rock physics: Geophysics, **76,** 141-153.

Eberhart-Phillips, D., D.-H. Han, and M. D. Zoback, 1989, Empirical relationships among seismic velocity, effective pressure, porosity and clay content in sandstone: Geophysics, **54**, 82–89.

Eberli, G. P., G. T. Baechle, F. S. Anselmetti, and M. L. Incze, 2003, Factors controlling elastic properties in carbonate sediments and rocks, The Leading Edge, **22,** 654-660.

Engels, S., and M. C. Roberts, 2005, The architecture of progading sandy-gravel ridges formed during the last Holocene Highstand; Soutwestern British Columbia, Canada: Journal of Sedimentary Research, **75**, 1052-1064.

Fortin, J., Y. Guéguen, and A. Schubnel, 2007, Effects of pore collapse and grain crushing on ultrasonic velocities and V_P/V_S: Journal of Geophysical Research, **112**, B08208, doi:10.1029/2005JB004005.

Gassmann, F., 1951, Über die elastizität poröser medien (Elasticity of porous media), Vierteljahrsschrift der Naturforschenden Gesselschaft in Zürich, **96**, 1-23.

Grochau, M., and B. Gurevich, 2007, Investigation of core data reliability to support time-lapse interpretation in Campos Basin, Brazil: 77th Annual International Meeting, SEG, Expanded Abstracts, 2969-2973.

Grochau, M., and B. Gurevich, 2009, Testing Gassmann fluid substitution: sonic logs versus ultrasonic core measurements: Geophysical Prospecting, **57**, 75-79.

Guidry, S. A., M. Grasmueck, D. G. Carpenter, A. M. Gombos,S. L. Batchtel, and D. A. Viggiano, 2007, Karst and early fracture networks in carbonates, Turks and Caicos Islands, British West Indies: Journal of Sedimentary Research, **77**, 508-524.

Gunda, R., and A. A. Volinsky, 2008, Tip-induced calcite single crystal nanowear: Mat. Res. Soc., Symp. Proc.

Gurevich, B., D. Makarynska, M. Pervukhina, and O. B. De Paula, 2009, A new model for squirt-flow attenuation and dispersion in fluid-saturated rocks: 71st EAGE Conference & Exhibition, Amsterdam, the Netherlands.

Gurevich, B., D. Makarynska, and M. Pervukhina, 2009, Ultrasonic moduli for fluid-saturated rocks: Mavko-Jizba relations rederived and generalized: Geophysics, **74**, 25–30.

Gurevich, B., D. Makarynska, M. Pervukhina, and O. B. De Paula, 2009, A new squirt-flow model of elastic wave attenuation and dispersion in fluid-saturated rocks: Poromechanics IV, Proceedings of 4th Biot Conference on Poromechanics, Paper 92.

Gurevich, B., and J. Carcione, 2011, Differential form and numerical implementation of Biot's poroelasticity equations with squirt dissipation: Geophysics, Accepted for publication June 2011.

Gurevich, B., D. Makarynska, O. B. De Paula, and M. Pervukhina, 2010, A simple model for squirt-flow dispersion and attenuation in fluid-saturated granular rocks: Geophysics, **75**, 109-120.

Han, D-H., A. Nur, and D. Morgan, 1986, Effects of velocity and clay content on wave velocities in sandstones, Geophysics: **51**, 2093-2010.

Huerta, A. P., M. Cusack, W. Zhu J. England, and J. Hughes, 2007, Material properties of brachiopod shell ultrastructure by nanoindentation, Journal of Royal Society Interface: **4**, 33-39.

Jahnert, R., O. B. De Paula, L. Collins, E. Strobach, and R. Pevzner, 2011, Evolution of a carbonate barrier in Shark Bay by GPR Imaging: Architecture of a holocene reservoir analogue: Sedimentary Geology (submitted).

Jones, T. D., 1986, Pore fluids and frequency dependent wave propagation in rocks: Geophysics, **51**, 1939–1953.

Josh, M., B. Clennell, and T. Siggins, 2009, Practical broadband dielectric measurement of geological samples: 50th SPWLA Annual Logging Symposium, Woodlands Texas, June 21-24.

Lebedev, M., M. Pervukhina, O. B. De Paula, B. Clennell, and B. Gurevich, 2009, Dynamic elastic properties from micro-CT images: modeling and experimental validation: EGU General Assembly, Expanded Abstracts.

Kuster G. T., and Toksöz, M. N., 1974, Velocity and attenuation of seismic waves in two phase media: Geophysics, **39**, 587-618.

Logan, B. W., G. R. Davies, J. F. Read, and D. E. Cebulski, 1970, Carbonate sedimentation and environments, Shark Bay, Western Australia: Memoir of the American Association of Petroleum Geologists, **13**, 223.

Logan, B.W., J. F. Read, G. M. Hagan, P. Hoffman, R. G. Brown, P. J. Woods, and C. D. Gebelein, 1974, Shark Bay, Western Australia: Memoir of the American Association of Petroleum Geologists, **22**, 358.

Lucia, J. F., 2007, Carbonate reservoir characterization, an integrated approach: 2nd Edition.

Mackenzie, K.V., 1981, Nine-term equation for the sound speed in the oceans: J. Acoust. Soc. Am., **70**, 807-812.

Martyniuk, M., 2006, Low-Temperature micro-opto-electro-mechanical technologies for temperature sensitive substrates: PhD Thesis, The University of Western Australia.

Mavko, G., and A. Nur, 1975, Melt squirt in the aesthenosphere: Journal of Geophysical Research, **80**, 1444–1448.

Mavko, G., and A. Nur, 1979, Wave attenuation in partially saturated rocks: Geophysics, **44**, 161-178.

Mavko, G., and D. Jizba, 1991, Estimating grain-scale fluid effects on velocity dispersion in rocks: Geophysics, **56**, 1940–1949.

Mavko, G., T. Mukerji, and J. Dvorkin, 1998, The rock physics handbook: Cambridge University Press.

Medina, H. E., W. Tuttle, R. C. Graham, M. F. Allen, and J. J. J. Osornio, 2010, Identification of underground Karst features using ground-penetrating radar in Northern Yucatán, México: Vadose Zone Journal, **9**, 653-661.

Merkel, C., J. Deushle, E. Griesshaber, , S. Enders, E. Steinhauser, R. Hochleitner, U. Brand, and W. W. Schmahl, 2009, Mechanical properties of modern calcite-(Mergerlia truncata) and phosphate-shelled brachiopods (Discradisca stella and Lingula anatina) determined by nanoindentation: J Struct Biol, **168**, 396-408.

Mikhaltsevitch, V., M. Lebedev, and B. Gurevich, 2011, A low-frequency laboratory apparatus for measuring elastic and anelastic properties of rocks: SEG, Expanded Abstract.

Murphy, W. F. III., K. W. Winkler, and R. L. Kleinberg, 1986, Acoustic relaxation in sedimentary rocks: Dependence on grain contacts and fluid saturation: Geophysics, **51**, 757–766.

Neal, A., 2004, Ground-penetrating radar and its use in sedimentology: principles, problems and progress: Earth-Science Reviews, **66**, 261-330.

Nowack, R. L., 1990, Tomography and the Herglotz-Wiechert inverse formulation: Pure and Applied Geophysics, **133**, 305-315.

Ortega, J. A., F. J. Ulm, and Y. Abousleiman, 2007, The effect of the nanogranular nature of shale on their poroelastic behavior: Acta Geotechnica, **2**, 155-182.

O'Connell, R., and B. Budiansky, 1977, Viscoelastic properties of fluid-saturated cracked solids: Journal of Geophysical Research, **82**, 5719–5735.

Palmer, I. D., and M. L. Traviolia, 1980, Attenuation by squirt flow in undersaturated gas sands: Geophysics, **45**, 1780-1792.

Pervukhina M., D. N. Dewhurst, B. Gurevich, U. Kuila, T. Siggins, M. Raven, and H. M. Nordgård Bolås, 2008, Stress-dependent elastic properties of shales: measurement and modeling: The Leading Edge, **27**, 772-779.

Pervukhina M., B. Gurevich, D. N. Dewhurst, and A. F. Siggins, 2010, Applicability of velocity-stress relationship based on the dual porosity concept to isotropic porous rocks: Geophysical Journal International.

Playford, P.E., and A. E. Cockbain, 1976, Modern algal stromatolites at Hamelin Pool, a hypersaline barred basin in Shark Bay, Western Australia, In M. R. Walter, Developments in sedimentology, Stromatolites, **20**, 389-411.

Salat, C., and A. Junge, 2010, Dielectric permittivity of fine-grained fractions of soil samples from eastern Spain at 200 MHz: Geophysics, **75**, 1-9.

Sayers, C. M., and M. Kachanov, 1991, A simple technique for finding effective elastic constants of cracked solids for arbitrary crack orientation statistics: International Journal of Solids and Structures, **27**, 671–680.

Sayers, C. M., and M. Kachanov, 1995, Microcrack-induced elastic wave anisotropy of brittle rocks: Journal of Geophysical Research, **100**, 4149–4156.

Siggins A.F., and D. N. Dewhurst, 2003, Saturation, pore pressure and effective stress from sandstone acoustic properties: Geophysical Research Letters, **30**, 1089.

Shapiro, S. A., 2003, Elastic piezosensitivity of porous and fractured rocks: Geophysics, **68**, 482–486.

Shulakova, V., M. Pervukhina, T. M. Muller, M. Lebednev, S. Schmidt, P. Golodoniuc, O. B. De Paula, B. M. Clennel, and B. Gurevich, 2011, Computational elastic up-scaling of sandstones on the basis of X-ray microtomographic images: Geophysical Prospecting (submitted).

Smith, T. M., C. H. Sindergeld, and C. S. Rai, 2003, Gassmann fluid substitutions: A Tutorial: Geophysics, **68**, 430-440.

Ulm, F. J., and Y. Abousleiman, 2006, The nanogranular nature of shale: Acta Geotechnica, **1**, 77-88.

Thomsen, L., 1995, Elastic anisotropy due to aligned cracks in porous rock: Geophysical Prospecting, **43**, 805–829.

Tod, S. R., 2002, The effects of stress and fluid pressure on the anisotropy of interconnected cracks: Geophysical Journal International, **149**, 149–156.

Vanorio, T., C. Scotellaro, and G. Mavko , 2007, "To fluid-substitute or not to fluid-substitute": How pore shape and chemical processes affect Gassmann's predictability: SEG, Expanded Abstracts.

Vernik, L., and J. Hammam, 2009, Stress sensitivity of sandstones and 4D applications: The Leading Edge, **28**, 90-93.

Zhang, J. J., T. F. Wong, and D. M. Davis, 1990, Micromechanics of pressure-induced grain crushing in porous rocks: Journal of Geophysical Research, **95**, 341-352.

Zimmermann R. W., W. H. Somerton, and M. S. King, 1986, Compressibility of porous rocks: J. Geophys. Res., **91**, 12765-12777.

Walsh, J. B., 1965, The effect of cracks on the compressibility of rock: Journal of Geophysical Research, **70**, 381–389.

Wang, Z., 2000, The Gassmann equation revised: Comparing laboratory data with Gassmann's predictions in Z. Wang, A. Nur and D. A. Ebron eds.: Seismic and Acoustic Velocities in Reservoir rocks, SEG, 8-23.

Weiner, S., L. Addadi, and H. D. Wagner, 2000, Materials Design in Biology, Material Science.

Wong, T.-F., C. David, and W. Zhu, 1997, The transition from brittle faulting to cataclastic flow in porous sandstone: Mechanical deformation: J. Geophys. Res., **102**, 3009-3026.

Zhang, J., T.-F. Wong, and D.M. Davis, 1990, Micromechanics of pressure-induced grain crushing in porous rocks: J. Geophys. Res., **95**, 341-352.

Every reasonable effort has been made to acknowledge the owners of copyright material. I would be pleased to hear from any copyright owner who has been omitted or incorrectly acknowledged.

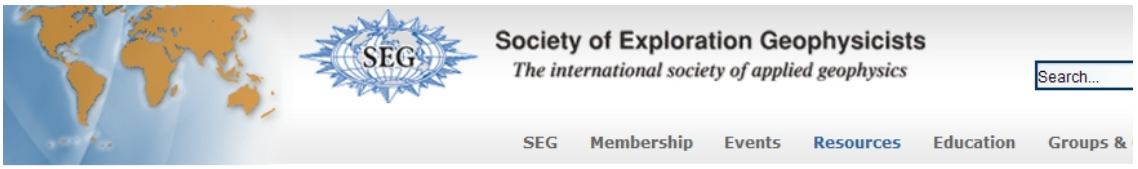

Permissions

SEG publishes journals, books, and digital works with the primary aim of disseminating research in and theory and applications of applied geophysics. Consistent with this objective, the Society provides mechanisms for those who seek to reuse or republish material from SEG publications while protecting the viability of the SEG publications program. Any further questions about permissions can be sent via e-mail to the SEG publications department at permissions@seg.org.

Fair use
Authors and publishers may present or republish up to two figures or tables per SEG article or per SEG book without seeking written permission from SEG, provided that full acknowledgment of the source is provided in the new work. If SEG has cited a publication for which it is not the publisher, rights should be obtained from that publisher. SEG considers this fair use. There are no fees associated with this permission. Authors who need documentation that SEG is extending this permission are encouraged to print this message and present it to their publishers. Those who require further documentation should contact the SEG publications director. SEG recommends that authors and publishers who intend to reuse SEG figures or tables also seek consent of the original work's lead author, if possible. The member search on the SEG Web site might prove a helpful resource in locating these authors. Requests to use any portion of "Seismic Data Analysis: Processing, Inversion, and Interpretation of Seismic Data" should be directed to the SEG publications director.

Permission granting
Those seeking permission to republish more material than described above should contact the SEG publications director. Such requests should include complete citations of works for which permission to republish is sought. If permission for specific figures or tables is sought, please provide figure and table numbers. Requests should include a description of the work in which the SEG material would be republished. Information about the audience and the intended distribution also should be included. The requests should be prepared on institutional letterhead if the requesting party is representing an institution. License fees are assessed only when the request is for a large amount of material or when the proposed usage is commercial in nature or would limit SEG's market. If a license fee is assessed, it must be paid prior to use or the permission is void.

Purchase redistribution rights online
Those seeking to redistribute SEG publications or portions thereof in print, by fax, or online may purchase permission to do so online. SEG publications are registered with the Copyright Clearance Center, and licenses to redistribute SEG articles and portions of books are obtained through this nonprofit agency. Special pricing is available for university professors, including license to distribute SEG material through electronic course packs. Licenses also are available for distribution of journal articles and expanded abstracts via e-mail or posting on Intranets and Extranets for limited time periods.

Authors' right to redistribute
Authors of articles in GEOPHYSICS, THE LEADING EDGE, and the Technical Program *Expanded Abstracts* may post their own articles on their personal Web sites or the Web sites of their institutions without obtaining further permission from SEG. Authors of journal articles and *Expanded Abstracts* retain similar rights for print redistribution. If an author or an author's institution redistributes an author's article online or in print, the original publication venue encompassed in a complete citation and including SEG's status as publisher must be identified. Authors of SEG books, or portions of SEG books, must seek permission from the SEG publications director to redistribute these works in any form. Such permission will not be withheld if SEG's investment in the original publication of the works is not threatened. Questions should be directed to the publications director.

Publications

Copyright

PUBLICATIONS

Bulletin
Digital Products
DEG Journal
Explorer
Special Publications
Advertising

SUBMIT A PAPER:

Bulletin
DEG Journal
Special Publications

General Copyright Information and Permissions FAQs

AAPG Owns Copyright on Most of its Publications

AAPG obtains copyright of both print and digital/electronic ownership from most authors of articles and books published by AAPG. If any material requested was reprinted by AAPG with the permission of another publisher, it is the responsibility of those requesting permission to obtain permission from that original publisher.

AAPG Authors

Authors wishing to use AAPG copyrighted material within work being published by AAPG are not subject to fees nor do they need to seek permission from AAPG; however, it is the responsibility of authors to provide proper citation. Permission without a fee is granted to AAPG authors who wish to republish portions of their own work as long as AAPG copyright credit is given. For both instances please refer below to "Condition of Grant of Permission".

Special Fair Use Permission

If you want to use a single figure, a brief paragraph, or a single table from an AAPG publication in a paper in another publication, AAPG considers this to be fair usage, and you need no formal permission. In that case, you should print a copy of this document and present it to your publisher. You are, however, required to provide proper citation.

How to Apply for Permission

Authorization for additional copies of items copyrighted by AAPG in any form, hardcopy, digital/electronic scanning or other digital transformation into computer-readable and/or transmittable form, for personal or corporate use is granted provided the appropriate fee is paid directly to the Copyright Clearance Center, 222 Rosewood Drive, Danvers, Massachusetts 01923. For circumstances occurring outside authorization of